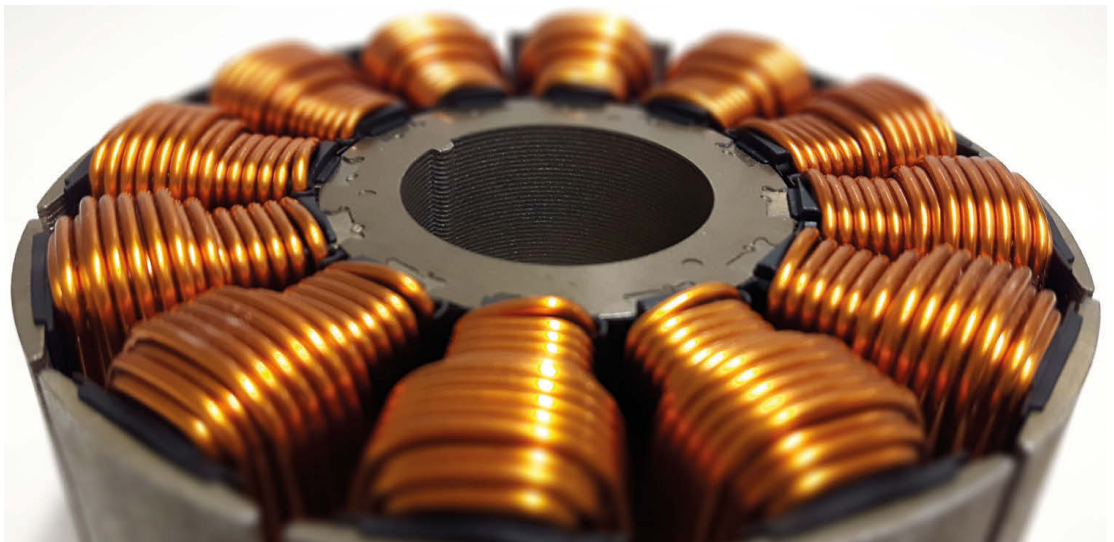


Christian Dinca

Motor Design for maximum Material Exploitation and Magnetization Procedure with in-line Quality Check for Mass Production



Christian Dinca
**Motor Design for maximum Material Exploitation and
Magnetization Procedure with in-line Quality Check
for Mass Production**

Die Schriftenreihe *Elektrische Energietechnik an der TU Berlin*
wird herausgegeben von:

Prof. Dr. Sibylle Dieckerhoff,

Prof. Dr. Julia Kowal,

Prof. Dr. Ronald Plath,

Prof. Dr. Uwe Schäfer

Christian Dinca

**Motor Design for maximum Material Exploitation and
Magnetization Procedure with in-line Quality Check
for Mass Production**

Bibliografische Information der Deutschen Nationalbibliothek

Die Deutsche Nationalbibliothek verzeichnet diese Publikation in der Deutschen Nationalbibliografie; detaillierte bibliografische Daten sind im Internet über <http://dnb.dnb.de> abrufbar.

Universitätsverlag der TU Berlin, 2017

<http://verlag.tu-berlin.de>

Fasanenstr. 88, 10623 Berlin

Tel.: +49 (0)30 314 76131 / Fax: -76133

E-Mail: publikationen@ub.tu-berlin.de

Zugl.: Berlin, Techn. Univ., Diss., 2016

Gutachter: Prof. Dr.-Ing. Uwe Schäfer

Gutachter: Prof. Dr.-Ing. Arnulf Kost

Gutachter: Prof. Dr.-Ing. habil. Dr. h.c. Kay Hameyer

Die Arbeit wurde am 29. August 2016 an der Fakultät IV unter Vorsitz von Prof. Dr.-Ing. Ronald Plath erfolgreich verteidigt.

Diese Veröffentlichung – ausgenommen Zitate und Abbildungen – ist unter der CC-Lizenz CC BY 4.0 lizenziert.

Lizenzvertrag: Creative Commons Namensnennung 4.0

<http://creativecommons.org/licenses/by/4.0>

Umschlagfoto: Christian Dinca | CC BY SA

<https://creativecommons.org/licenses/by-sa/2.0/>

Druck: Meta Systems Publishing & Printservices GmbH, Wustermark

Satz/Layout: Christian Dinca

ISBN 978-3-7983-2883-9 (print)

ISBN 978-3-7983-2884-6 (online)

ISSN 2367-3761 (print)

ISSN 2367-377X (online)

Zugleich online veröffentlicht auf dem institutionellen Repository der Technischen Universität Berlin:

DOI 10.14279/depositonce-5630

<http://dx.doi.org/10.14279/depositonce-5630>

Preamble

The following dissertation was done during my employment as an scientific coworker at the Technische Universität Berlin at the chair of electric drives of Prof. Dr.-Ing. Uwe Schäfer, to whom I extend my utmost gratitude.

Special thanks goes to all the students who wrote their final theses under my supervision and contributed a lot to this dissertation. The discussions led to fruitful publications and patents. Additionally, I would like to thank Dr.-Ing. Manfred Filtz with whom I was able to solve some of the magnetic field problems.

I would like to thank Jürgen Federspiel from our workshop who built most of the mechanical setups I designed, and gave several hints on how to achieve powerful solutions.

I am very delighted to have successfully allured Prof. Dr.-Ing. habil. Dr. h.c. Kay Hameyer, Prof. Dr.-Ing. Arnulf Kost and Prof. Dr.-Ing. Uwe Schäfer into being my reviewers for this dissertation.

Last but not least, I would like to thank my family for the patience, motivation and grasp.

Contents

Nomenclature	XI
1 Introduction	1
2 Motor Design for an Electric Suspension System	7
2.1 Specifications	8
2.2 Fundamental Production techniques for electric Motors	9
2.2.1 Packetization	10
2.2.2 Segmentation	11
2.2.3 Winding	12
2.3 Motor type Selection	13
2.3.1 Inner vs. outer Rotors	17
2.3.2 Winding type Selection	17
2.4 Design of the Electric Suspension System	19
2.4.1 Design of the pressure Can	20
2.4.2 Design of Stator and Rotor	22
2.4.3 Sensor Concept	35
2.5 Production and Assembly of the Motor Parts	35
2.5.1 Winding	36
2.5.2 Magnet Fixation	38
2.5.3 Can Production	40
2.5.4 Connection Ring	41
2.5.5 Stator and Rotor Assembly	41
2.6 Simulations	42
2.6.1 Efficiency and Loss Simulations	43
2.6.2 Cogging Torque Simulations	44
2.6.3 Equivalent Circuit	45
2.6.4 Current curve Shape and Control	47
2.6.5 Circulating Currents	47
3 Materials and Manufacturing Methods for thermal Optimization	49
3.1 Thermal impact of Insulating Material	49
3.1.1 Enamelled Winding Wire	50
3.1.2 Slot insulation Liner	51
3.1.3 Potting	52
3.1.4 Electrical Steel	52
3.2 Thermal impact of Manufacturing Methods	53
3.3 Thermal Model	56
3.3.1 Combined Wire Insulation Material	56

3.4	Testing matrix and Equipment	58
3.4.1	Thermal Testing Setup	59
3.4.2	Testing Matrix	59
3.5	Thermal Tests and Simulation Results	61
3.6	Motor thermal Simulations	61
4	Rotor design for Magnetization	65
4.1	Magnetizing and demagnetizing Mechanisms	65
4.1.1	Pinning Mechanism	65
4.1.2	Nucleation Mechanism	66
4.1.3	Magnetization Fields	67
4.2	NdFeB Magnet Ingredients and their Impact	67
4.3	Demagnetizing Curves	69
4.4	High Field generation for the magnetizing Process	70
4.4.1	Specifications of the magnetizing Circuit	72
4.4.2	Brief Design Description	74
4.5	Rotor Design for Magnetization	75
4.5.1	Magnetic Saturation during Magnetization	76
4.5.2	Penetration Angle and Strength of the Field	77
4.5.3	Skewing of the Rotor	77
4.5.4	Thermal Path for the Heat generated during Magnetization	77
4.5.5	Fixation Technique	78
4.5.6	Rotor design for the Quality Control Magnetizer	78
5	The Quality Control Magnetizer	79
5.1	Pulsed Field Magnetometer	79
5.1.1	Pulsed Field Magnetometer Field Analysis	80
5.1.2	Pulsed Field Magnetometer Setup	81
5.1.3	Eddy current Effects	83
5.1.4	Magnetic Viscosity	86
5.1.5	Non-homogeneous fields and their Consequences on the demagnetizing Tensor	87
5.1.6	Demagnetization Tensor depending on Susceptibility	87
5.1.7	Temperature dependence of the demagnetizing Curves	88
5.2	Designing the Quality Control Magnetizer	89
5.2.1	Specifications for a Quality Control Magnetizer	89
5.2.2	Limitations of the developed Quality Control Magnetizer	89
5.2.3	Testing Oscillations	90
5.2.4	Arrangement of the Coils	91
5.2.5	Field and Force Calculations for the Coils	93
5.2.6	The demagnetizing Factor/Function	95
5.2.7	The reference demagnetizing Function for different Magnets	97
5.2.8	Detection of Demagnetization	97
5.2.9	Eddy Effects	99
5.2.10	Magnetic Viscosity	102
5.2.11	Temperature Dependence of the demagnetizing Curves	103
5.2.12	Influence of neighboring Magnets	104

5.2.13	Mechanical Tolerances	105
5.2.14	Variations in Rotor Steel	106
5.2.15	Hysteresis of the Compensator Steel	106
5.2.16	Steel for the magnetizing Fixture	108
6	Testing and Analysis	109
6.1	Motor Testing	109
6.1.1	Resistance, Inductance and EMF	110
6.1.2	Motor Efficiency Measurements	111
6.1.3	Cogging Torque Measurements	111
6.2	Can Test Setup and Analysis	112
6.2.1	Can Test Setup without an equivalent Stator	113
6.2.2	Can Test Setup with an equivalent Stator	115
6.2.3	Analysis of the pressure Testing	116
6.3	Magnetizer Test Setup and Analysis	116
6.3.1	Calibration of the Pulse Field Magnetometer	118
6.4	Calibration of the Quality Control Magnetizer	123
6.4.1	Hysteresis Measurements of a Rotor in a Quality Control Magnetizer	124
6.4.2	Eddy Current Calibration in a Quality Control Magnetizer	125
6.5	Quality Control Magnetization of Ferrites	125
6.5.1	Magnetization with a non-conductive Rotor	125
6.5.2	Magnetization with a laminated Steel Rotor	129
6.5.3	Magnetization with a different Rotor	129
6.5.4	Missing Magnet	130
6.6	Quality Control Magnetization of NdFeB Magnets	130
7	Conclusion and Discussion	133
7.1	Electric Suspension System	133
7.2	Maximum flux Utilization and metallic Cans	135
7.3	Sensitivity Analysis for different Insulation Material Combinations	136
7.4	Magnetization and Quality Control	139
8	Summary and Outlook	145
8.1	Design for maximum Magnet material Exploitation	145
8.2	Design for Magnetization and Quality Control	146
A	Appendix	163
A.1	Motor type Choice Decision Matrix	163
A.2	Inner vs. Outer Choice Decision Matrix	166
A.3	Winding Technology Decision Matrix	167

Nomenclature

Greek

ρ_{fiber}	Fiber content of the filament
σ_{can}	Tension of the can
σ_{t}	Tensile yield strength of the fiber in tangential direction
ϑ_{r}	Electric rotor angle
Ψ_{d}	Linked flux in direct direction
Ψ_{q}	Linked flux in quadrature direction
$\Psi_{\text{u,v,w}}$	Linked flux of each phase

Latin

A_1	Creep rupture properties
A_2	Influence of the ambient conditions
A_3	Temperature influence
A_4	Influence of variation and inhomogeneity
A_{gap}	Current loading
Ang_{notch}	Notch angle
A_{slot}	Slot area
A_{tot}	Total safety factor
A_{wire}	Cross section of one copper wire conductor
B_{gap}	Average flux density over the rotor surface
BH_{max}	Maximum energy density
$Bridge$	Bridge thickness
$B_{\text{r,min}}$	Minimum remanent flux density
D_{a}	Outer diameter of the can

d_{can}	Depth of equivalent can beam
D_r	Rotor diameter
E_{can}	Young modulus of can
$f_{\text{max,can}}$	Maximum warpage
f_{wfirst}	Winding factor of the first effective harmonic
f_{wx}	Winding factor
Gap	Air Gap
$H_{\text{cB,min}}$	Minimum coercive field strength
$H_{\text{cJ,min}}$	Minimum intrinsic coercive force
I_d	Current in direct direction
$I_{\text{phase,rms}}$	Phase RMS current
I_q	Current in quadrature direction
$I_{\text{u,v,w}}$	Current in each phase
$I_{y,\text{can}}$	Moment of inertia
J_{slot}	RMS current density inside each slot
K	Output coefficient
l_{can}	Length of can
L_d	Synchronous direct inductance
LM	Magnet thickness
L_q	Synchronous quadrature inductance
L_{stk}	Effective stator length
m	Number of phases
N	Number of turns
n_{layers}	Number of layers in each slot; 1 for single layer winding; 2 for two layer winding
N_{parallel}	Parallel coils of each phase
N_{ph}	number of turns per series per phase
p	Inner pressure
q_{can}	Area load
R_1	Rotor radius
R_3	Stator outer radius

R_{ph}	Phase resistance at 20 °C
R_{SH}	Shaft Radius
r_{slot}	Slot chamfer radius
SO_{ang}	Slot opening angle
SD	Slot depth
s_{f}	Minimum thickness of the can
S_{fg}	Gross copper fill factor
SB_{fill}	Chamfer radius
SO	Slot opening
S_{safe}	Overall can safety factor
TGD	Slot opening depth
$T_{\text{c},20-150}(B_{\text{r}})$	Remanent flux density temperature coefficient
$T_{\text{c},20-150}(H_{\text{ci}})$	Intrinsic coercive field temperature coefficient
t_{can}	Thickness of can
T_{inner}	Inner torque
TO	Tooth opening width
TWS	Tooth width
W_{mag}	Magnet width
W_{slot}	Magnet slot width

Acronyms

BLDC	Brushless Direct Current.
CTE	Coefficient of thermal expansion.
ESS	Electric Suspension System.
FEA	Finite Element Analysis.
FMEA	Failure Mode and Effect Analysis.
GMR	Giant Magneto Resistance.
HREE	Heavy Rare Earth Element.
IPM	Internal Permanent Magnet.
LREE	Light Rare Earth Element.
MTPA	Maximum Torque Per Ampere.
MTPW	Maximum Torque Per Watt.
PA	Polyamide.
PAM	Post Assembly Magnetization.
PCB	Polychlorinated biphenyl.
PEEK	PolyEther Ether Ketone.
PFM	Pulsed Field Magnetometer.
PPS	PolyPhenylene Sulfide.
QCM	Quality Control Magnetizer.
REE	Rare-earth Element.
RTM	Resin Transfer Moulding.
SPM	Surface Permanent Magnet.

1 Introduction

Electric motors designed for prototypes are usually different from their mass produced counterparts. Since time and cost factors are not as critical for prototypes as they are for mass produced motors, different production methods are used. This thesis presents guidelines for the design of electric motors for mass production. Due to the complexity of this issue, the focus of this thesis will be on the design of electric motors for maximum magnet exploitation, and a newly introduced magnetization procedure with in-line quality check.

Electric drives are highly manifold, hence the mentioned topics are applied exemplarily on a drive of an Electric Suspension System (ESS). Special interest lies in the cost effective construction of the magnetic active components. Therefore, cost drivers are exposed and cost effective designs are proposed.

When a drive is designed for the first time, the cost of the drive can be best estimated from previous models. For the drive currently under investigation, information was limited since there was no electric suspension system built yet, and only limited information was available about the new 48 V DC link board net standard [151] for which the drive should be designed. As a solution to this problem, production line companies were already involved in the first designs which led to the prototype presented in detail in the following chapters. Additionally, the design minimizes the cost of raw materials, especially for copper and magnet material which consume a big portion of the overall motor costs.

In the automotive industry, the size and power density of an electric drive is of major importance since weight and space is limited. To decrease the size of an electric drive, high energy density magnets are inevitably used. Rare-earth Element (REE) magnets like SmCo_5 , $\text{Sm}_2\text{Co}_{17}$ or NdFeB feature such high energy densities as shown in Tab. 1.1. NdFeB magnets show the largest energy density and are a good choice for high power density drives. NdFeB magnets were developed in 1982 by General Motors and

Tab. 1.1: Energy density $(\text{BH})_{\text{max}}$ of different kind of magnets [202]

Magnet	Ferrite	SmCo_5	$\text{Sm}_2\text{Co}_{17}$	NdFeB
$(\text{BH})_{\text{max}} / \text{kJ/m}^3$	10-40	120-190	190-280	290-415

Sumitomo Special Metals [93]. Until the 1990s, the USA was the biggest producer of REE at its Mountain Pass Mine in the Mojave desert, which at the time was used for special military equipment. The exploitation of such minerals comes along with severe environmental problems. To understand the history of REE and today's dependency on the Chinese market, one has to take a look at how they are mined and commercialized [149].

At first, rocks containing REE are crushed and ground into a powder. Mixed in special tanks, the REE containing minerals float on top, while the rest sinks to the ground. This hazardous waste material, i.e. tailings, has to be stored in holding basins. In the meantime, the desired minerals are heated in kilns and dissolved in acid. Only a small part of the resulting slush contains REE, and is subsequently extracted for refinement [64]. The residual dissolvent includes radioactive elements such as Thorium and Uranium and is very difficult to recycle, resulting in it being shored in ponds. In [149], it is said that the Mountain Pass Mine produced 850 gallons of waste water every minute in the mid 1990. Because of the hazardous waste, the government refused to issue new permits for additional holding basins, so that the mine had to be closed by 2002. In [64] it is claimed that the production of each ton of REE material results in the generation of 1-1.4 tons of radioactive waste. This is different from the radioactive waste generated in nuclear power plants because it is not enriched.

In 2003 Wen Jiabao, a geologist from Gansu province, became prime minister of China and saw the geo-political potential of REE for his country, which holds the largest deposits of Light Rare Earth Element (LREE) and Heavy Rare Earth Element (HREE) [37]. Due to lower environmental protection standards, as well as lower labor cost, China was able to flood REE onto the market, sometimes at dumping prices, resulting in a wave of bankruptcies of a lot mining companies all over the world. Since 2003 the price of LREE, mostly mined in the Bayan Obo Mining District in Inner Mongolia (China), has soared continuously due to export quotas introduced in 2006 [113]. Export taxes from 15% to 25%, depending on the type of REE raw material, were introduced in 2007 to keep the production chain of the raw REE material to the final magnets inside China. Export taxes on finalized magnets have not been introduced so far. In 2010, Chinese firms accounted for 97 % of REE oxide production, together with a high production volume for REE alloys [37]. In the same year China embargoed Japan after a maritime incident [37]. The events catalyzed the tremendous rise of REE prices. Many Chinese mining companies did not accept central government export restrictions on Japan, and started to smuggle REE, especially HREE [113], out of China. It is said in [113] that in 2010, the real output for REE was 45 % larger than the 89,200 metric tons the central government had set as a production quota. Despite the fear of the market being embargoed by the Chinese central government, the price for REE minerals did not rise as much as predicted. To valorize REE, the Chinese government increased export taxes for raw material up to 25 % in 2011, resulting in the transition of many European magnet manufacturers from magnet manufacturing to trading and reselling.

Due to severe environmental problems caused by illegal mining and the ongoing problem of the tailings ponds, the central government closed down several mines and processing companies. Due to the increased price of REE material, companies in several other countries opened or reopened their mines - usually for LREE [205]. On January 5th 2015, China announced that it will end export regulations for rare earth minerals [206], after losing a trial, in World Trade Organization court in 2013.

HREE deserve the name "rare" since there are only a few known occurrences of the elements in the world so far; namely in Northern Australia [121], Mountain Pass [205] and southern China [150]. Other sites of HREE found in Canada, South Africa, Russia and Kazakhstan are yet to be exploited [64]. The economic and political situation

around REE changes monthly, so the author stopped investigating the political status of REE on the 28th of February 2015 for this dissertation.

There are several elements which belong to the group of LREE and HREE (see Tab.



Fig. 1.1: Molycorp[®] Mountain Pass Mine (June 2015)

1.2). Some of them like Nd, Pr, Sm and Tb and Dy are of great importance for NdFeB and SmCo magnets. The weight percent (wt. %) of the elements of NdFeB and SmCo

Tab. 1.2: Light(LREE) and Heavy (HREE) rare-earth Elements

LREE	Sc	La	Ce	Pr	Nd	Pm	Sm	Eu	Gd
HREE	Tb	Dy	Ho	Er	Tm	Yb	Lu	Y	

magnets are shown in Tab. 1.3 and Tab. 1.4, respectively. NdFeB magnets contain

Tab. 1.3: Weight percent of NdFeB Magnets [101]

Element	Nd	B	Dy	Co	Al	Ga	Tb	Fe
wt. %	13-35	0.8-1.3	0-15	0-15	0.5-2	0-1	0-0.5	rest

0%-15% of the HREE Dysprosium which enables durability at higher temperatures (see section 4). Looking at the recent price development of REE shown in Fig. 1.2, it can be stated that higher temperatures inside a NdFeB magnet increase its raw material cost due to the need of Dy. In June 2011 when the topic of this thesis was formulated, magnet prices were subject to large fluctuations. Therefore, two questions arose:

- How can we reduce the REE content in electric motors for mass production?

Tab. 1.4: Weight percent of SmCo Magnets [101]

Element	Sm	Fe	Cu	Zr/Hf/Ti	Co
wt. %	24.5-28	13.5-22	3-12	1.3-3.2	rest

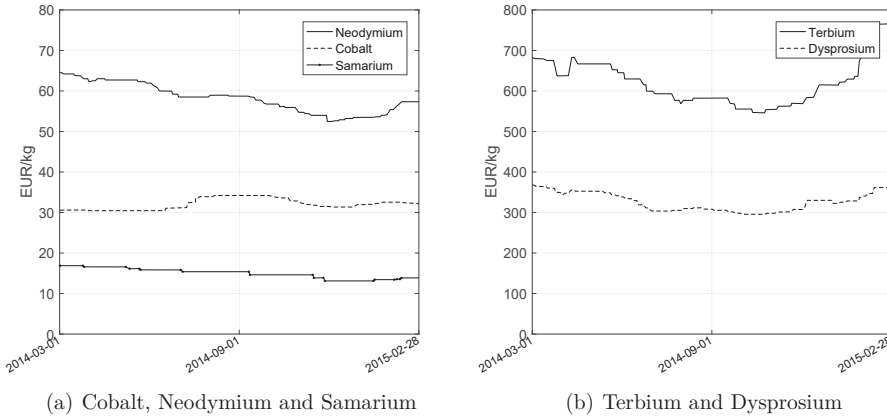


Fig. 1.2: Selected REE raw material prices in EUR/kg (China mainland) [146, 169]

- How can we prepare for quick changes of suppliers as prices vary?

To investigate the first question in more detail, one has to differentiate between the maximum exploitation of the used REE material and the temperature reduction inside the magnet resulting in a HREE reduction. Reducing the amount of REE goes along with the reduction of magnetic stray flux, which can be achieved by reducing big air gaps, or avoiding metallic cans between stator and rotor. These cans are usually used for hermetically sealing the rotor from the stator in applications where a wet rotor configuration is used. Because of the low electric resistance, metallic cans are subject to eddy current losses which are caused by the rotating field of the rotor. Using non-conductive cans, which are not subject to eddy currents, leads to a lower possible pressure inside the rotor because of the lower strength of the material. Additionally, the losses cause heating of the fluid, and eventually also that of the magnets. The magnet temperature can also be reduced by lowering the overall temperature of the motor, which is increased by other motor losses. In this thesis, a wound glass fiber can will be used for hermetically sealing the rotor from the stator. It will be shown how this non-conductive can will perform in a pressurized environment with regard to mechanical tolerances. Additionally, the overall motor temperature will be reduced by electric insulation improvements.

The second question deals with the situation of rising magnet prices and what to do about it. Changing the vendor might be a possible solution, but comes along with tedious preparations. Is a new vendor going assure the quality standard over a whole batch? How much fluctuation occurs in a production batch? Testing of a whole pro-

duction batch is tedious, time consuming and expensive. Therefore, it might be useful to have in-line production test equipment which checks for various magnetic properties, without increasing production time. To check magnets for their quality, they have to be magnetized. Handling magnetized permanent magnets in a production line is very difficult. First, all tools used to pick and place magnetized magnets need to be of non-ferrous material. Second, the closer the magnets are to the magnetic rotor the bigger the force needed to hold them back. Since sintered REE magnets are brittle, there is a big risk of broken edges. Inserting the pre-magnetized magnets into an Internal Permanent Magnet (IPM) rotor is also challenging because the magnets tend to stick to the rotor pockets, which might destroy the corrosion resistant coating. While Post Assembly Magnetization (PAM) rotors do not have these disadvantages, they only allow limited possibilities of quality control, as checking the magnet quality requires the magnets to be magnetized.

In this thesis, a new method is introduced which allows to check for certain magnetic parameters of a PAM rotor during magnetization. To prove the concept of maximized exploitation of magnet material, as well as the magnet quality check, an ESS was chosen as an automotive application with high torque density as well as high temperatures. The motor, as well as the power electronics, are built up and tested with respect to mass production. To decrease temperatures inside the motor, several electric insulation materials were tested. The inverter needed to drive the motor is not further discussed in this thesis, because of its low impact on the magnetic design. Further information about the inverter design can be found in [39].

2 Motor Design for an Electric Suspension System

In modern cars more than 120 electric drives mostly used for auxiliary functions are increasing complexity and power consumption. Hence, even small electric actuators are required to work at high efficiency. In the mid 90s of the last century, the 42 V board net was introduced [41], enabling lower DC currents at the same power outputs. Unfortunately, this system did not manage to succeed due to the lack of automotive qualified components. A new approach was made in 2011, introducing the 48 V system [151] that should coexist with the 12 V standard board net. Since more and more high energy consumers are disconnected from the crank shaft, the 48 V system offers the advantage of having lower copper cross sections in the DC lines, thereby reducing the weight and the cost of the car. At the time when the standard was defined, automotive power semiconductors as well as drivers were still missing and standard industrial products had to be used.

An Electric Suspension System is a 48 V system. It adjusts the dampers of each wheel with respect to road terrain, allowing an almost vibration free driving experience [110]. The system today consists of a central oil pump connected to the crank shaft of the combustion engine. Four pressure storages combined with two vents for each wheel are supplied by the central oil pump. Due to the direct connection, the pump is always rotating and causing losses, even if no additional refill of the pressure storages is needed. For this reason, the central oil pump should be replaced by 4 individually operating servo oil-pumps.

The presented motor was chosen for this thesis in cooperation with an automotive manufacturer, resulting in several advantages:

- Direct specification from a automotive manufacturer
- Application specified space requirements
- Variable usage for CO₂ climate compressors for automotive applications
- Challenging thermal specifications
- Mass produced item with a minimum of 200.000 pieces/year
- 48V DC Link

This thesis only deals with the electric drive and the involved boundaries, but not with the whole electric suspension system which was developed by the automotive company.

2.1 Specifications

The specifications for the motor and power electronics have been derived from a more general specification sheet for the whole suspension system:

- General:
 - Wet rotor configuration
 - No magnetic losses due to the can
 - Degree of protection of enclosure according to DIN 40 050 IP6K9K
 - high efficiency for the drive with more than 75 % at all working points
 - nominal Torque 10.4 Nm
 - nominal Speed 4,200 RPM
- Electrical:
 - fully functional from 36 V to 52 V DC [151]
 - maximum occurring voltage 60 V DC [151]
- Geometric:
 - max. motor length 200 mm
 - max. motor diameter 125 mm
- Max. weight 7 kg
- Thermal specifications for speeds above 15 km/h:
 - air coolable
 - minimum air temperature $-40\text{ }^{\circ}\text{C}$
 - maximum air temperature $+80\text{ }^{\circ}\text{C}$
- Working fluid: Pentosin CHF 11 S
 - minimum oil temperature $-40\text{ }^{\circ}\text{C}$
 - maximum oil temperature $+80\text{ }^{\circ}\text{C}$
 - short maximum oil temperature $+125\text{ }^{\circ}\text{C}$
 - oil temperature:
 - $-40\text{ }^{\circ}\text{C}$ for 200 h
 - $+60\text{ }^{\circ}\text{C}$ for 4,700 h
 - $+80\text{ }^{\circ}\text{C}$ for 1,000 h
 - $+110\text{ }^{\circ}\text{C}$ for 400 x 15 min
 - $+125\text{ }^{\circ}\text{C}$ for 50 x 5 min

static pressure 15 bar - 60 bar

dynamic pressure max. 160 bar

- Corrosion resistant:

anodic aluminum or

seawater resistant aluminum

steel parts coated in black ZnFe

- Recycling:

the drive has to be able to be separated into its parts

parts have to be labeled with raw material names

following hazardous contaminants are not allowed:

CFC, Polychlorinated biphenyl (PCB), Asbestos, Pb, Hg, Cd

- Accuracy of the system:

the system has to be able to hold pressure when quasi-stationary

- Parametrization:

the motor has to have variable length and torque outputs

all other components also have to be adaptable

Electronics, programming, the pumping wheel and communication interfaces are also mentioned in the complete specification sheet but will not be further discussed in this thesis.

2.2 Fundamental Production techniques for electric Motors

In this section, a short overview of fundamental production techniques of electric motors is given. Winding as well as lamination packetization techniques are presented. An overview of electric insulation systems is presented in chapter 3, while magnetization technologies are presented in chapter 4 and 5. Motor types and their fundamentals can be found in [53, 88] and will not be presented in this thesis.

2.2.1 Packetization

For eddy current reduction electric machines consist of non-oriented silicon alloyed laminated electrical steel [114]. These lamination steel sheets can be produced in several ways:

- Stamping
- Laser cutting
- Eroding

Stamping of the lamination is the most profitable way for the mass production, while lasering and eroding are usually used for small batches because of the high energy and time consumption [73]. After cutting, the steel is packetized which can be processed in several ways:

- Interlock packetization
- Baking lacquer
- Welding
- Gluing
- Clinching
- Clamping

Interlock packetization (see Fig. 2.1(a), 2.1(b)) is one of the easiest and cheapest ways to form the stator/rotor [69]. Besides cutting, the stamping tool will also punch the bead into the lamination sheet, which enables good positioning of the packet. As interlock packetization is a weak bonding, the mechanical strength needs to be achieved by winding. When wound, the winding wire is wound with an almost constant tension. The more turns wound around the lamination, the bigger the compressive force on the laminations.

Baking lacquer (see Fig. 2.1(c), 2.1(d)) is usually combined with lasered lamination sheets and is commonly used for prototypes. The lacquer is applied onto the sheet insulation and has a thickness of $5\ \mu\text{m}$ to $8\ \mu\text{m}$ [69]. It is colorless, non-reactive at room temperature. Packetization is usually carried out at about $210\ ^\circ\text{C}$ over a period of about 2 min [69]. Heating of the packet can either be done by induction or hot air circulation. The heat of the cutting laser could lead to an evaporation of the baking lacquer near the cutting edges, which reduces the bonding of the packet. Lasered baking lacquer laminations cannot be annealed, because activation temperature of the lacquer is lower than the annealing temperature, $730\ ^\circ\text{C}$ to $790\ ^\circ\text{C}$ [114]. Hence, losses could be higher than for stamped annealed laminations [50].

Welding (see Fig. 2.1(e), 2.1(f)) is one of the classic packetization procedures. The seam is usually placed in a magnetically inactive region, so that the electric short caused by the weld seam does not increase eddy current losses [114]. The bonding is weak, so that the package becomes stable when wound.

Gluing (see Fig. 2.1(g), 2.1(h)) is a good alternative for mass production. During stamping, a glue spot is placed on the lamination, then the next sheet is pressed

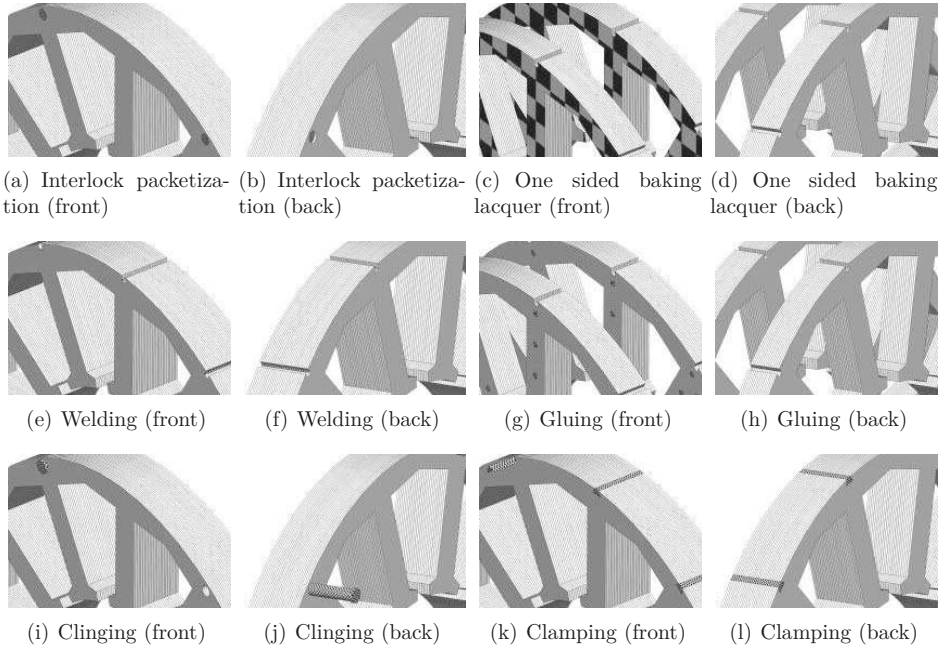


Fig. 2.1: Paketization options [69]

against it, forming a good hold. The position of the sheet is controlled by a servo motor which gives better tolerances when skewing is favored. The cyanoacrylate glue cannot withstand temperatures higher than 80 °C [81], the strength at higher temperatures is only provided by the winding. Higher temperatures methods are market ready [163]. Clinging (see Fig. 2.1(i), 2.1(j)) is also a classical way to form the package. The bolts are pressed into pre-formed holes and are bent at the end. The selective hold of the bolts forms wavy packets with low quality [69]. Clamping (see Fig. 2.1(k), 2.1(l)) is done with preformed brackets which are pressed into the groove of the packet. This is usually used for industrial standard motors [69].

2.2.2 Segmentation

To get better access to the winding machine, the stator can be segmented. This has many advantages for mass production. Besides the bigger fill factor, the production throughput can also be bigger. Common segmentation techniques are:

- I-segments
- T-segments
- Pole star

- Pole shell
- Pole chain

I- and T-segments (see Fig. 2.2(b), 2.2(c)) are accessible for a winding machine. I-segments can also be equipped with preformed coils [69]. The teeth are usually connected to the yoke by a dove tail. I-segments could suffer from vibrations caused by tolerances of the connection point [62]. The exploitation of the laminations sheets is better for the T-segments because of the lack of a yoke ring. The run-out of the inner stator diameter is determined by the connection surfaces of the T-segments.

The pole star segmentation (see Fig. 2.1(d)) consists of I-segments which are connected at the slot openings by thin bridges [69]. Preformed coils are clipped onto the teeth. The thin bridges cause flux leakage which results in a lower exploitation of the given magnetic material.

The pole shell (see Fig. 2.1(e)) is a cross between a full stator (see Fig. 2.1(a)) and a pole star configuration (see Fig. 2.1(d)) [69]. Due to the lack of pole shoes, it is easier to wind compared to a full stator. For lower torque ripple, the shell is added.

The pole chain (see Fig. 2.1(f)) is an enhancement of the T-segments and overcomes the problem of the difficult assembly of single T-segments. For better assembly after winding, the segments are connected by pins [92] or by small steel bridges [77].

2.2.3 Winding

In this section, the different basic winding techniques are presented. Although there are several variations of each winding techniques, only needle, flyer, linear and insertion winding is explained. Others can be found in [69, 70, 71].

Before starting the linear winding procedure (see Fig. 2.3), the wire is fastened at the tooth. Next, the tooth is rotated while the wire nozzle (in diamonds) is moved to assure that the wires are wound orthocyclically. After winding, the nozzle is rotated around a pin (not shown in Fig. 2.3) to fasten the wire which is cut afterwards [69].

Needle winding (see Fig. 2.4) consists of a movable needle which is inserted into the slot openings of a full stator. The needle is then moved around the tooth to place the wire at its designated position. To wind a full stator which does not have to be separated into the single tooth is very advantageous, but also comes along with compromises. Since the needle needs space inside the full stator, this space has to be left empty, resulting in a lower copper fill factor [69].

Flyer winding is usually applied with outer slotted stators but can also be used for single teeth as shown in Fig. 2.5. Other than linear winding where the tooth is rotated, with flyer winding, the needle rotates around the tooth. Baffle plates guide the wire to its designated place. Insertion winding is usually used for distributed windings. A comb, shown in Fig. 2.6, is flyer wound with windings and inserted into the stator bore. A rounded shaft takes the windings which extend into the stator bore, and moves them along the stator into the winding windows [118]. The wires have to be flexible so that they can be bent easily, which limits the wire diameter. This results in random windings inside the stator bore and limits the copper fill factor.

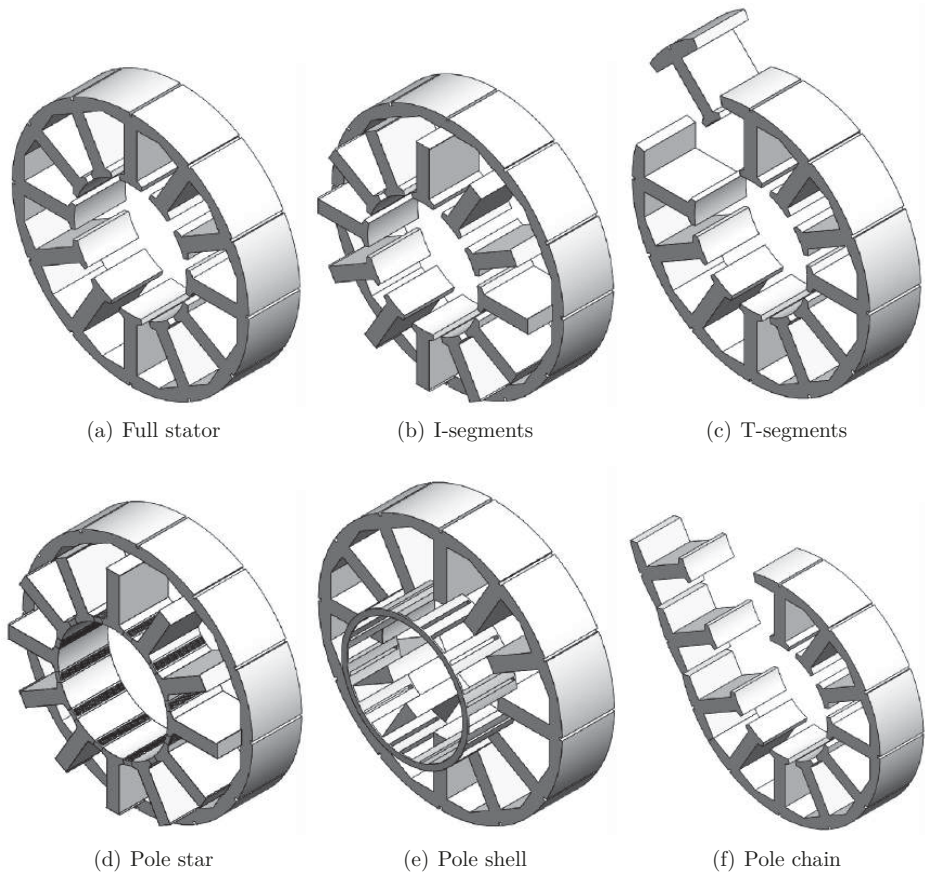


Fig. 2.2: Stator segmentation variations [69]

2.3 Motor type Selection

Before designing the ESS, several basic decisions have to be made. For the motor type, identification experts were gathered to fill out a decision making matrix with several categories. Every main category contains subcategories which can be seen in appendix A.1. The main categories were:

- Designated space
- Weight
- Efficiency
- Ability to modularize
- Research intensity

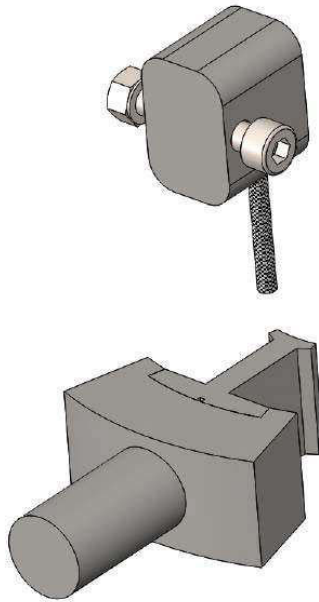


Fig. 2.3: Linear winding scheme [69]

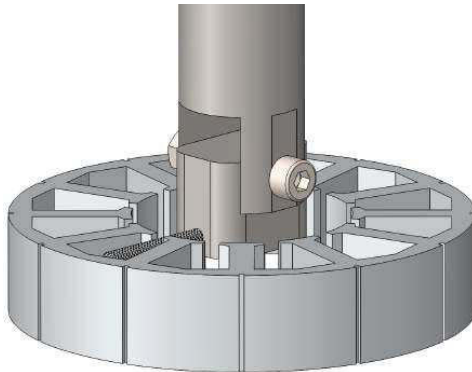


Fig. 2.4: Needle winding scheme [69]

- Manufacturability
- Manufacturing costs
- Consequences of material price development
- Acoustics
- Sensors
- Robustness

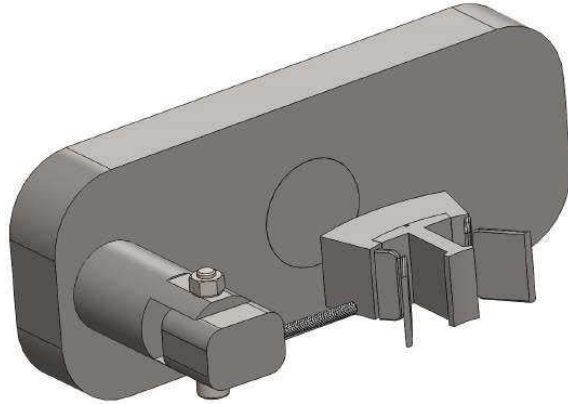


Fig. 2.5: Flyer winding scheme [69]

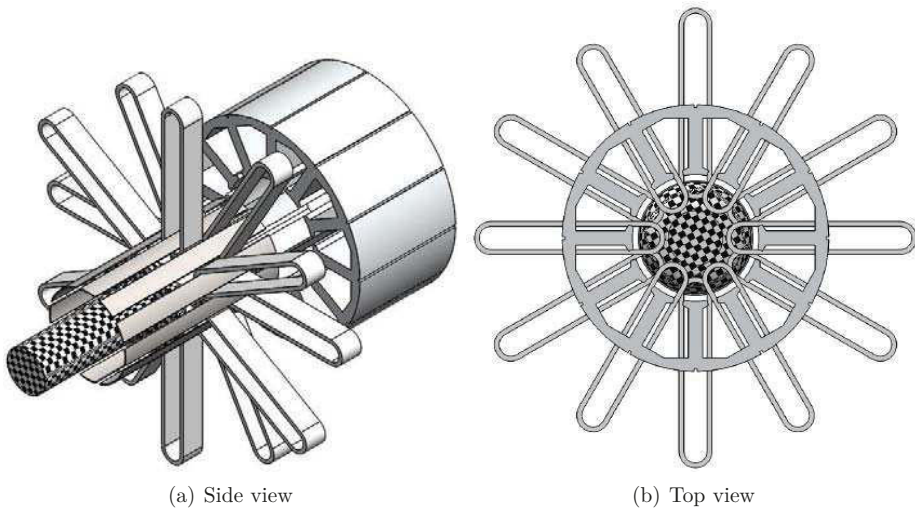


Fig. 2.6: Insertion winding [118]

- Modular manufacturability
- Dynamics

To weight the different categories the well known Analytic Hierarchy Process is used [99]. This process is slightly modified to ease the decision making process. According to [99] when comparing two categories against each other, the scheme shown in Tab. 2.1 is used to find out the weightings. This scheme is rather complex and time consuming, so only three relevances were used for this process as shown in Tab. 2.2 [89]. Experts from the Technische Universität Berlin and a big automotive company evaluated the following motor types based on the specifications mentioned before. Scores were given as seen in Tab. 2.3. The investigated motors are:

Tab. 2.1: Values and relevances for the Analytic Hierarchy Process [99]

value	relevance
1	equal relevance
3	slightly/marginally greater relevance
5	greater relevance
7	significantly large relevance
9	dominating

Tab. 2.2: Compact values and relevances for the Analytic Hierarchy Process [89]

value	relevance
0	marginal relevance
1	equal relevance
2	large relevance

- Induction machine with squirrel cage rotor
- Synchronous machine
 - Sine commutated
 - Surface Permanent Magnet
 - Internal Permanent Magnet
 - Block commutated
 - Surface Permanent Magnet
 - Internal Permanent Magnet
- Reluctance machine
 - Synchronous Reluctance Machine

It was decided that the switched reluctance motor is unsuitable because of the noise generation. More exotic machines were not investigated because of the lack of experience in mass production. The subcategories can be found in the appendix A.1. Based on the results, a synchronous motor, block commutated internal permanent magnet

Tab. 2.3: Scores for decision matrices

Score	Suitability
0	bad/unsuitable
1	
2	
3	
4	
5	very good

motor IPM Brushless Direct Current (BLDC) was chosen since it got the most points, fulfilling the requirements best. The predominant factors for this decision are the possible configuration only with a single current sensor in the DC-link. This also enables the usage of that motor for other configurations like water or oil pumps where dynamics of the drive are of less importance. For these applications, the motor's length can be shrunk in its length while still being manufacturable on the same production line. For the ESS, a positioning sensor with a better accuracy is needed.

2.3.1 Inner vs. outer Rotors

To decide whether an inner or outer rotor should be used, a similar investigation was conducted regarding the following categories. The subcategories can be found again in the appendix:

- Power and Torque
- Manufacturability of rotor
- Manufacturability of stator
- Cooling
- Costs
- Mechanical

The following three types of IPM BLDC motors were investigated:

- Inner rotor with two sided bearing
- Outer rotor with one sided bearing
- Outer rotor with two sided bearing

The basis of that evaluation was, the same size, closed housing i.e. IP6K9K and no rotor shaft cooling. The same 0-5 scoring system was used, naming the inner rotor with two sided bearing as the most suitable candidate. The subcategories can be found in appendix A.2.

2.3.2 Winding type Selection

For the selection of a suitable winding type, a similar decision making matrix was filled out with winding experts from the company Aumann. This company was chosen because of its extensive experience with winding machines and fully automated production lines.

Because of the general smaller copper fill factor [88], insertion winding was excluded from the decision by request of the automotive company. The following winding strategies were investigated:

- Needle winding of pole chain
- Needle winding of inside slotted stator
- Needle winding of outside slotted stator
- Flyer winding of single tooth
- Flyer winding of outside slotted stator
- Flyer winding of pole chain
- Linear winding of outside slotted stator
- Linear winding of single pole
- Linear winding of pole chain
- Hook or guide winding

The parameters are:

- Quality of the wire after winding
- Electric copper fill factor
- Heat removal of the winding
- Automation
- Stator pre- and post-processing
- Phase insulation
- Electric symmetry of the phases/windings
- Mechanical symmetry of the stator
- Turnout of the winding machine
- Investment for stator production
- Number of contacts
- Electric circuitry of the poles
- Flexibility of the circuitry
- Vibration stability
- Usability for diversification of types and set-up costs
- Number of stator parts
- Ability to wind thick copper wire
- Good wire return with orthocyclic winding

This time a decision matrix scheme according to VDI 2225 [119] was used. This was done because of the standard procedure and comparability with other projects of the company Aumann. The most suitable winding technology is single tooth windings in T-Shape. For the prototype, several guidelines were determined:

- The laminations are laser cut and baking lacquer packetized because of time and costs - for mass production they will be interlock packetized or glued
- The magnets will be glued in magnetized state into the rotor - for mass production PAM will be used (see section 4)
- The winding pattern will be tried on a modified standard linear winding machine before a specialized piece of equipment is manufactured

2.4 Design of the Electric Suspension System

The development of the ESS was done completely from scratch because at that time, such a system was not available. The oil pressure of 160 bar was especially challenging. Compared to other pumps, like electric oil or water pumps, where the dissipated heat from the motor is removed via the pumping fluid, the ESS does not allow this due to the double flow direction of the pumped medium. If a car is undergoing a slalom turn, hot oil that is pumped in one direction comes back after only a few seconds and heats up the pump and motor even more. This can be clearly seen in Fig. 2.7, where the speed vs. time and torque vs. time graphs of the motor are shown. Therefore, the drive has to be cooled externally. The automotive car maker insisted on having air cooling with no extra fan. Another challenging issue was the target production price of each

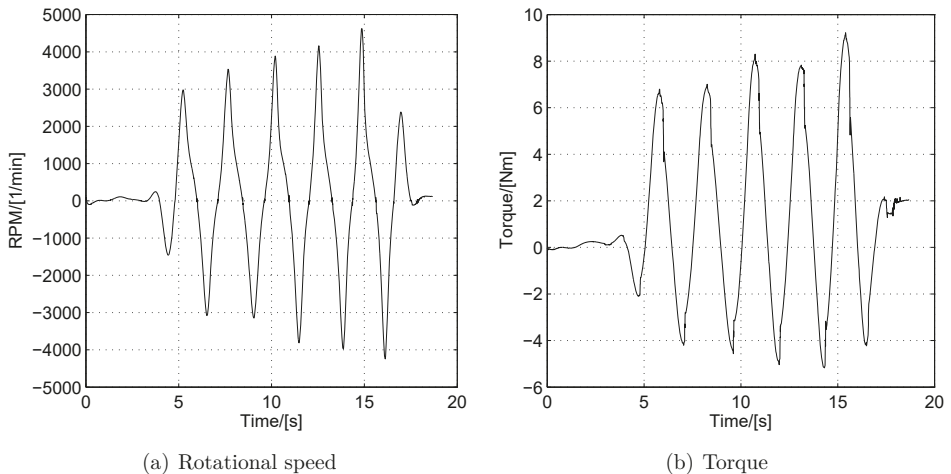


Fig. 2.7: Rotational speed and torque measurements of the ESS vs. time measured on a typical slalom test

unit, including power electronics, pumping wheel and housing. Due to the political issues mentioned in the introduction, the magnets alone made up for about 17% of the cost of the total product, at a volume of 200,000 pieces a year in mid 2011.

In Fig. 2.8 the schematic set-up of the motor is shown. In the following sections, the magnetic, electrical, mechanical and thermal design of various components are explained. The specifications have the following impact on the design:

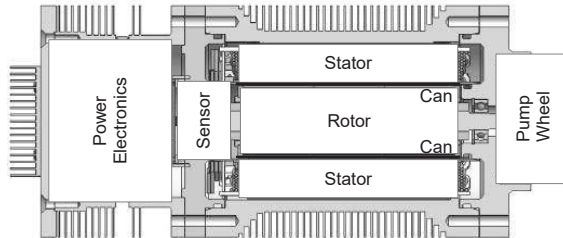


Fig. 2.8: Components of the drive shown in a cross sectional view [24]

- The thickness of the can determines the size of the magnetic air gap
- Very high power density has to be achieved
- Very high efficiency of the whole drive - higher than 75% in all working points
- Very high copper fill factor at moderate costs
- Magnet volume is one of the critical issues because of the high costs
- Power electronics must be included in the whole design from the beginning onwards
- Cheap and precise positioning sensor has to be used for controlling the pressure/torque at stand still
- The inertia of all rotating parts should be kept small to decrease dynamic torque

2.4.1 Design of the pressure Can

The non-segmented pressure can cannot be made of a ferrous material because it would cause high eddy current losses. To fulfill the power density demands, the maximum thickness of the can was found to be 0.6 mm, when not being conductive. Manufacturing of thin cans made of thermoplastics is difficult. First attempts to glue a thicker can into the stator bore hole and mill it down to 0.6 mm failed already in operation at 25 bar. Glass fiber wound cans could be a better solution here.

Many authors have dealt with the problem of low to medium pressure cans [12, 91, 94, 98]. Metallic cans, usually made of stainless steel contribute up to 30% of the total losses for industrial standard 4 pole 50 Hz motors [14]. Nickel alloys like austenite 2.4610 [165] reduce the can losses because of their higher electric resistance and mechanical strength, which makes it possible to decrease the thickness [15, 24]. [15]

investigates a nickel alloy can for industrial pump applications, stating that the losses rise in proportion to the third power of the rotor diameter and the second power of the rotational speed. At maximum speed, the can losses are bigger than the copper losses. The metallic can in [15] is also used since the motor is cooled by the pumping fluid, so that a low thermal resistance of the can is beneficial to the transportation of the heat from the windings.

Wound cans, when made of non-conductive glass fiber, can also be manufactured very thin (see Fig. 2.9) and might be a good choice.



Fig. 2.9: Winding of the can in circumferential direction [24]

In [68, 79, 97, 111, 122], filament wound tubes are investigated regarding winding angle, thermal expansion and weepage, claiming that circumferentially wound cans at almost a 90 degree angle to the rotor axis could withstand the pressure specified in section 2.1. Since wound cans are not a mechanically continuous material, they have to be treated according to pressure vessel design guides [35]. The pressure vessel formula has to be extended for fiber reduction factors [24]:

- A_1 := Creep rupture properties
- A_2 := Influence of ambient conditions
- A_3 := Temperature influence
- A_4 := Influence of variation and inhomogeneity

These factors are multiplied with the overall safety factor S_{safe} , to calculate the total safety factor $A_{\text{tot}} := A_1 \cdot A_2 \cdot A_3 \cdot A_4 \cdot S_{\text{safe}}$. The minimum thickness s_f of the can can be calculated to:

$$s_f = \frac{D_a \cdot p \cdot A_{\text{tot}}}{2 \cdot \sigma_t \cdot \rho_{\text{fiber}}} \quad (2.1)$$

- s_f := Minimum thickness of the can
- D_a := Outer diameter of the can
- p := Inner pressure
- A_{tot} := Total safety factor
- σ_t := Tensile yield strength of the fiber in tangential direction
- ρ_{fiber} := Fiber content of the filament

Wound fiber tubes in industry are also common for armored sleeves for surface permanent permanent magnet motors [193]. For highly pressurized cans, they are still a niche in mass production. For the ESS, a glass fiber (Vetrotex[®] EC2400-P185) [203] as well as a carbon fiber (TOHO[®] Tenax HTS40F13) [199] are chosen. [35] proposes factors for fiber tubes which are shown in Tab. 2.4.

Tab. 2.4: Fiber reduction factors

A_1	A_2	A_3	A_4	S_{safe}
2	1.2	1.4	1.2	2

The outer diameter of 44.2 mm is chosen based on several facts which will be explained later on. The dynamic pressure of 160 bar defined in section 2.1 is taken as the maximum exposed pressure. As can be seen in Tab. 2.5 the minimum thickness is bigger

Tab. 2.5: Thickness of cans considering the safety factor A_{tot}

Fiber	σ_t	ρ_{fiber}	S_f
Vetrotex [®] EC2400-P185	2,400 MPa	63%	2.95 mm
TOHO [®] Tenax HTS40F13	4,620 MPa	63%	1.53 mm

than the required 0.6 mm, which is necessary for meeting the requirements for the power density. However, to decrease safety margins, testing is necessary. When decreasing all safety factors to $A_{\text{tot}} = 1$, the maximum pressure with a 0.6 mm can will be $p_{\text{carbon}} = 801$ bar and $p_{\text{glass}} = 416$ bar. Additionally, the stator has to be constructed in such a way as to mechanically support the tube. Therefore, the slot openings are a trade-off between support of the can and the magnetic flux leakage (see Fig. 2.10).

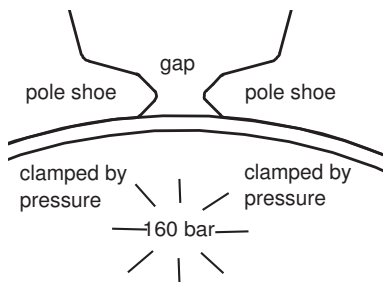


Fig. 2.10: Pressure indicated clamping of the can [24]

2.4.2 Design of Stator and Rotor

The stator is designed in three steps. First a basic manually optimized version is calculated, secondly, it is optimized in SPEED and thirdly, it is verified by Finite Element Analysis (FEA).

Single tooth winding usually implements a fractional slot winding pattern. A combination of 12 slots as well as 10 poles or 8 poles is suitable. 12 slots are chosen because of the good experience in prior industrial projects. Looking at Tab. 2.6 one can see the winding factors f_{wx} of the two combinations.

Tab. 2.6: Winding factors for 12 slot 10 pole and 8 pole combinations seen mechanical wise [24]

Winding factors	12 Slots 10 poles	12 Slots 8 poles
f_{w1}	0.066	0
f_{w2}	0	0
f_{w3}	0.5	0
f_{w4}	0	0.866
f_{w5}	0.933	0
f_{w6}	0	0
f_{w7}	0.933	0
f_{w8}	0	0.866
f_{w9}	0.5	0

The smooth surface of the rotor is necessary because of the wet rotor configuration and the friction losses involved. The combination of the IPM rotor with a smooth surface with slot openings limited by the pressure inside the magnetic air gap will produce a quasi trapezoidal EMF. Dry rotor configurations, which would also allow sinusoidal back EMFs, i.e. with surface bread loaf magnets or bent pole shoes in the rotor, are also possible [51].

When it comes to mass production of single tooth windings, delta connection has several advantages over wye connection. Delta connected windings can be wound in one work process without the need of cutting and connecting one end to the star connection ring. Parallel stranded wires can be avoided. This is due to the fact that the line to line EMF e_{LL} is smaller with delta connected phases compared to wye connection. While parallel windings increase the complexity of the winding process and limit the flexibility of the product, delta connected windings also have disadvantages. Looking at Tab. 2.6 one can see that the 12 slot 10 pole combination will produce a high third harmonic content. This leads to circulating currents [23].

The basic analytic magnetic circuit is calculated with the methods described in [53]:

$$T_{\text{inner}} = K D_r^2 L_{\text{stk}} \quad (2.2)$$

$$K = \frac{f_{w,\text{first}}}{\sqrt{2}} \frac{\pi^2}{4} B_{\text{gap}} A_{\text{gap}} \quad (2.3)$$

$$A_{\text{gap}} = \frac{2m N_{\text{ph}} I_{\text{phase,rms}}}{\pi D_r} \quad (2.4)$$

T_{inner}	:=	Inner torque
K	:=	Output coefficient
D_r	:=	Rotor diameter
L_{stk}	:=	Effective stator length
$f_{\text{w,first}}$:=	Winding factor of the first effective harmonic
B_{gap}	:=	Average flux density over the rotor surface
A_{gap}	:=	Current loading
m	:=	Number of phases
N_{ph}	:=	Number of turns per series per phase
$I_{\text{phase,rms}}$:=	Phase RMS current

[53] recommends a value of about 10 kNm/m^3 to 32 kNm/m^3 for totally enclosed motors and 11 kNm/m^3 to 39 kNm/m^3 for high performance servo motors. Another first guess factor is the current density inside the slots $J_{\text{slot,rms}}$. It is defined as:

$$J_{\text{slot,rms}} = \frac{n_{\text{layers}} \cdot N \cdot I_{\text{phase,rms}}}{N \cdot A_{\text{wire}} \cdot N_{\text{parallel}}} \quad (2.5)$$

In literature [53, 88], the denominator in formula 2.5 is sometimes defined as the copper fill factor S_{fg} times slot area A_{slot} .

$J_{\text{slot,rms}}$:=	RMS current density inside each slot
N	:=	Number of turns
n_{layers}	:=	Number of layers in each slot; 1 for single layer winding; 2 for two layer winding
A_{wire}	:=	Cross section of one copper wire conductor
N_{parallel}	:=	Parallel coils of each phase
S_{fg}	:=	Gross copper fill factor
A_{slot}	:=	Slot area

Recommended values are 5 A/mm^2 to 10 A/mm^2 for fan cooled motors [53]. The values chosen for the design are higher because of better cooling:

$$K = 39 \text{ kNm/m}^3 \quad (2.6)$$

$$J_{\text{slot,rms}} = 14.12 \text{ A/mm}^2 \quad (2.7)$$

For windability, a special tooth geometry is chosen as seen in Fig. 2.14. In contrast to normal teeth, where the back iron has a constant thickness, these teeth are designed such that the linear winding machine has good accessibility for all wires. The tongue and groove connection is subject to mechanical tolerances (see Fig. 2.15) which might lead to higher magnetic resistances. Therefore special care has to be taken, not only at laser cutting or stamping of the teeth, but also at stacking. The dimensions are shown in Fig. 2.11. Requirements for the rotor design are:

- IPM rotor for additional reluctance torque and easy fixation of the magnets

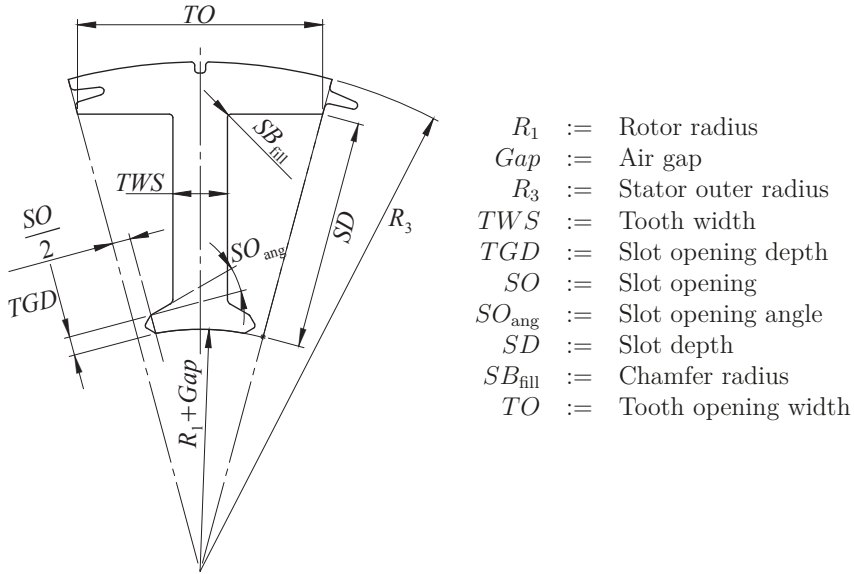


Fig. 2.11: Tooth and dimensioning variables

- Low inertia
- Low weight
- Easy magnetization by PAM
- Smooth surface for low oil friction

Several authors have dealt with the rotor magnet topologies [51, 53, 78]. For this particular motor, the set of possible variants was limited, since low weight, a smooth surface and easy PAM set strict limitations on the rotor choice. Because of the low weight specification, smooth surface and the reluctance torque at higher speeds, the configurations shown in Fig. 2.12(b) and 2.12(c) are not ideal. The topology shown in Fig. 2.12(a) is a good trade-off. It combines the largest amount of permanent magnet material per rotor volume, a smooth surface and a positive value for $L_q - L_d$. For outer PAM magnetization, the topology in Fig. 2.12(c) provides the best field saturation of the magnets if the magnetizing coils are not inserted into the hollow rotor bore. This will be discussed in chapter 4, where the design for magnetization is also explained.

The dimensions are shown in Fig. 2.13. The first guess solution using the formulas presented in [53, 88] leads to the values shown in Tab. 2.7.

Tab. 2.7: First guess solution

R_1	R_3	TWS	SD	Gap	L_{stk}
20 mm	40 mm	4.5 mm	18 mm	1.1 mm	100 mm

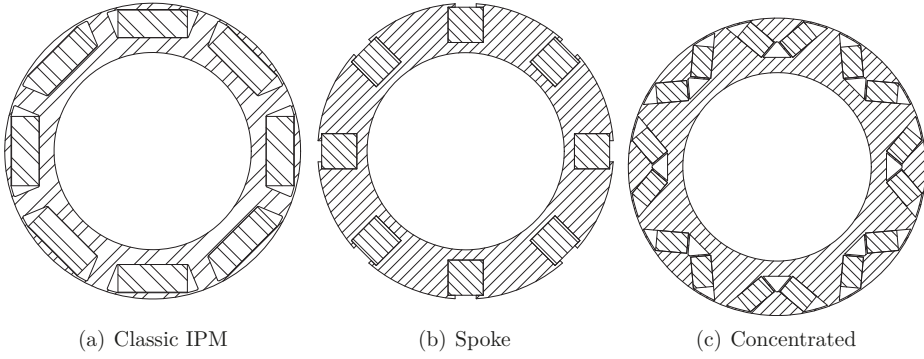


Fig. 2.12: Rotor topologies, [53]

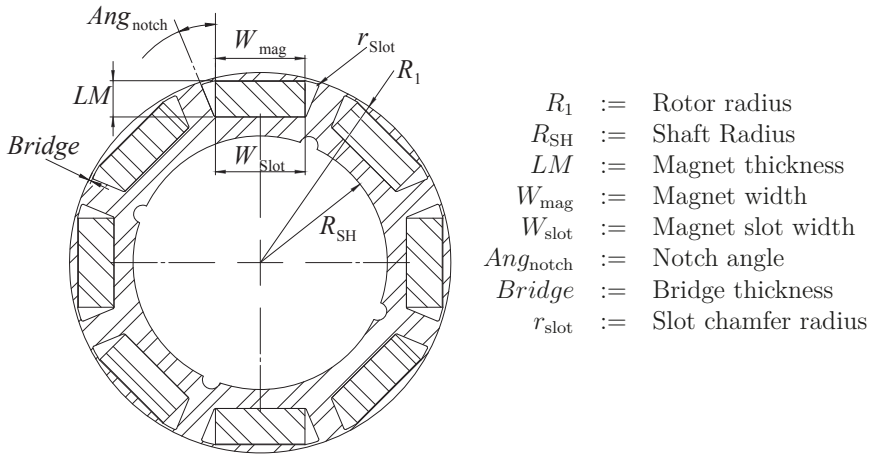


Fig. 2.13: Rotor and dimensioning variables

The air gap (*Gap*) was chosen to be 0.5 mm, plus 0.6 mm can. The motor is long compared to its diameter (see Tab. 2.7), because of the available space mentioned in section 2.1 and the force by the oil pressure which rises linear with the diameter. In [7] it is said that if a high pole number is chosen, concentrated winding is convenient only if the rotor diameter is larger than the effective length of the laminations (L_{stk}). This stands in clear contrast to the first guess parameters and the chosen single tooth winding. But from a production point of view, it is still the right choice since the torque can be adjusted by varying the length of the stator, without fundamentally changing the tooling of the winding machine. Linear winding machines provide some flexibility.

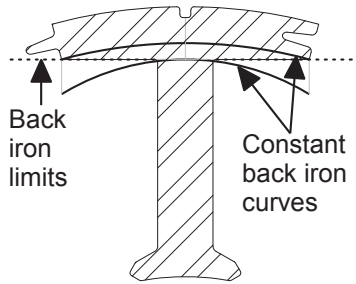


Fig. 2.14: Constant backiron curves and backiron limits

In Fig. 2.15 the tongue and groove of a single sheet are shown. The tongue is large and extends into the groove. Besides the better mechanical stability, it enables a bigger contact area of two teeth, therefore minimizing the increased magnetic gap resistance due to possible tolerances. The maximum allowed flux density in an FEA was set to max. 1.8 T, and to 1.5 T at no load [88]. The thinnest part of the back iron was increased by 0.5 mm to account for possible tolerances at the tongue and groove which might increase the magnetic resistance.

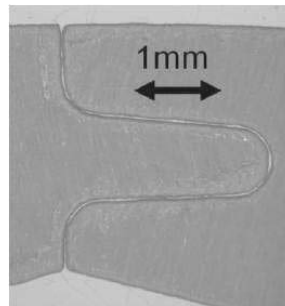


Fig. 2.15: Microscopic view on tongue and groove for single sheet [24]

The thickness of the magnet was determined to be 4 mm. The magnetic material is 255/200 according to IEC 60404-8-1 [154] with the specifications mentioned in Tab. 2.8. It was chosen because of its high energy product and its relatively high intrinsic coercive

field strength H_{cJ} at high temperatures (see Fig. 4.6). This enables a maximum phase current of about 980 A before starting to pass the knee point of the magnet material at 150 °C. The max. short transient circuit current is about 255 A at 5,000 RPM, when all phase cables are connected to each other.

Tab. 2.8: 255/200 magnet material specifications at 20 °C according to [154]

$B_{r,\min}$	$H_{cB,\min}$	$H_{cJ,\min}$	$(BH)_{\max}$	$T_{c,20-150}(B_r)$	$T_{c,20-150}(H_{cJ})$
1.17 T	875 kA/m	2,000 kA/m	255 kJ/m ³	-0.095 %/K	-0.510 %/K

$B_{r,\min}$:=	Minimum remanent flux density
$H_{cB,\min}$:=	Minimum coercive field strength
$H_{cJ,\min}$:=	Minimum intrinsic coercive force
BH_{\max}	:=	Maximum energy density
$T_{c,20-150}(B_r)$:=	Remanent flux density temperature coefficient
$T_{c,20-150}(H_{ci})$:=	Intrinsic coercive force temperature coefficient

Analytical simulation resulted in 31 turns of 1.6 mm copper wires which are wound around the tooth resulting in a gross copper fill factor $S_{fg} = 53\%$. The definition of the gross copper fill factor can be found in [24]. A very detailed description of the winding and winding optimization process is given in section 3. The windings are connected in parallel delta (see Fig. 2.16).

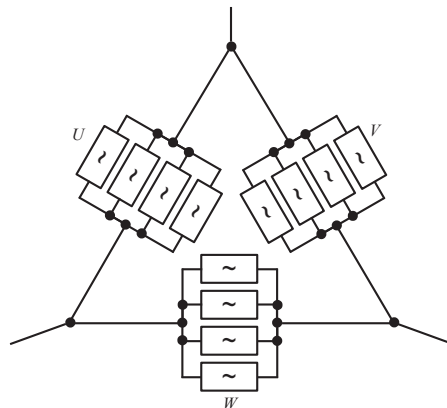


Fig. 2.16: Connection of windings

The power electronics which were developed [39] have a maximum output current of 120 A. The minimum voltage at which the drive still had to be functioning without restriction is 36 V at the specified temperatures. These values mark the boundaries for the electric design.

The motor design software SPEED 9.1 used for quasi analytical calculations is not able to predict flux densities in tooth and yoke accurately with respect to saturation. Therefore, the basic design has to be verified by FEA. For transient simulations, the inverter was modeled in ANSYS® Simpler® including a current controller and then connected to the FEA by double transient simulation. This has many advantages:

- Current curve shape will be included for
 - torque calculation
 - iron losses
 - magnet losses
- Controllability at very low speed can be simulated
- Maximum torque per current or voltage for non-sinusoidal current can be simulated
- Dynamics and transient load interaction can be simulated

Pure transient simulations without the inverter will also be beneficial when it comes to the investigation of circulating currents, with respect to mechanical and electrical tolerances (see section 2.6.5). Using the symmetry axis of a 12 slot 8 pole machine, the computation time can be reduced.

The differences in torque and especially in EMF calculations vary strongly from the quasi analytical SPEED solution to the FEA performed in ANSYS® Maxwell® for large slot openings (see Fig. 2.17). This is due to the defective fringing prediction of the magnetic flux inside the air gap. Additionally, SPEED uses a magnetic flux distribution inside the air gap which is shaped by so called X-factors. These factors work well for Surface Permanent Magnet (SPM) but become inaccurate with IPM rotors because of the influence of the rotor steel and slotting. Both modeling inaccuracies become especially prominent when the slot openings for fractional slot machines are changed. Other modeling approaches, where an expert mesh is created inside the air gap, promise higher accuracies, especially for the problem of fringing [3, 123].

The lamination material was chosen to be M330-35A coated with baking lacquer [196]. This non-oriented steel is cheap, usually available at all laser cutting manufacturers and has relatively moderate losses. Since non-grain oriented steel retains preferred directions because of the rolling direction (0 degree), both the angles of 0 degree and 90 degree directions have different magnetic specifications as shown in Fig. 2.18. It is advisable to have all teeth in rolling direction, while the back iron should be in the perpendicular direction if the back iron length is shorter than the tooth length for each pole. The rotor should be stacked with alternating orientations of the steel sheets.

The dimensions found with SPEED were loaded into Maxwell® by an automatic script which calculates the air gap flux density distribution or tooth flux vs. rotor position which can be used as input data for SPEED. The changes made afterwards in

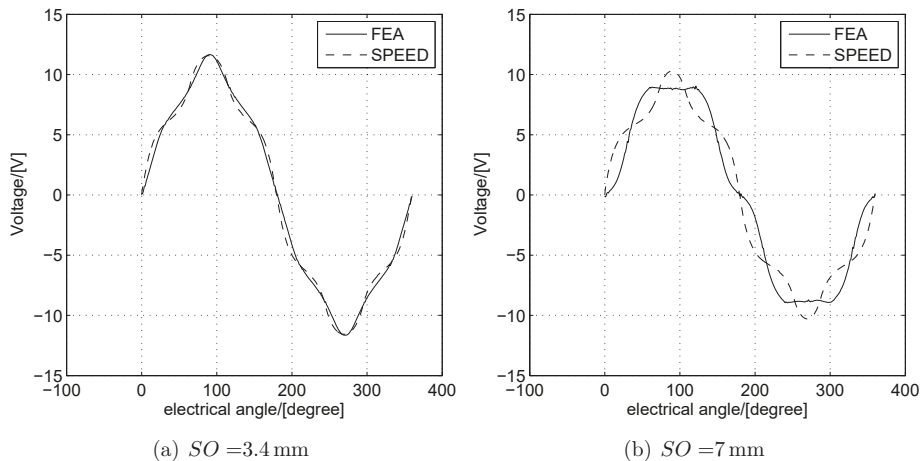


Fig. 2.17: Induced voltage at 1000RPM for different slot openings SO , FEA and SPEED results

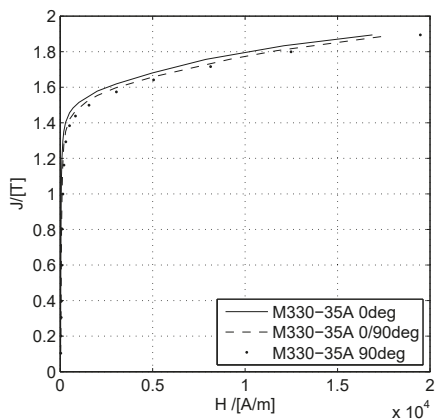


Fig. 2.18: Polarization vs. magnetic field of non grain oriented M330-35A in different angles to the rolled direction at 50 Hz [197]

SPEED should not be too big, so that the accuracy of the FEA air gap solution is still acceptable. The final dimensions are shown in Tab. 2.9.

Tab. 2.9: Final dimensions for the ESS motor design

R_1	R_3	TWS	SD	Gap	L_{stk}	SO	TGD	SO_{ang}
21 mm	46 mm	5 mm	21.1 mm	1.1 mm	120 mm	3.4 mm	1.5 mm	15 mm
$Bridge$	LM	W_{mag}	W_{Slot}	Ang_{notch}	r_{Slot}	R_{SH}	SB_{fill}	
0.3 mm	4 mm	9.8 mm	9.9 mm	22.5 degree	0.3 mm	14 mm	0.3 mm	

A rotor length of 120 mm is difficult to achieve, so it is separated into three 40 mm parts which are then press fitted onto a steel tube. The steel tube is also used as an additional back iron. This can be done because simulations showed that non-synchronous field harmonics inside the air gap, causing high eddy current losses, fade away at this depth. Additionally this technique can be used to skew the motor to decrease the cogging torque. For these applications skewing is not applied because of the non-necessary smoothness of the torque output. Additionally, the 12 slot 8 pole combination already provides low cogging torque compared to other combinations [100].

Most of the mechanical dimensioning e.g. for the stator housing are explained in [135] and would go beyond the scope of this thesis if discussed in detail. Some parts also affect the magnetic and thermal calculations and are presented in detail.

When forming a stator out of single teeth, the tolerances at the tongue and groove (see Fig. 2.15) lead to an error in concentric run out of the stator's inner diameter, which will increase tension on the can. Assuming a maximum tolerance of 0.01 degree, provided by the laminations manufacturer, at the plane regions of tongue and groove shown in Fig. 2.19, the maximum run out at the stator inner diameter is 3.9 mm (see Fig. 2.20). Therefore, wedges are placed in between the pole shoes, so that

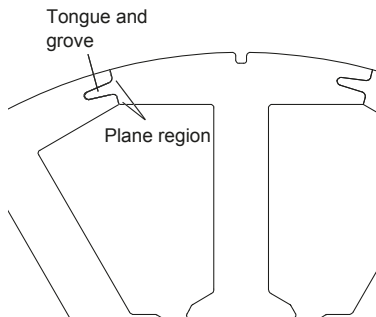


Fig. 2.19: Joint of teeth [24]

concentricity is assured. Sandglass wedges (see Fig. 2.21) enable a concentric run out of 0.2 mm when assuming manufacturing tolerances of 0.05 mm (see Fig. 2.22). When analyzing the can without wedges, the elastic beam theory might give a rough

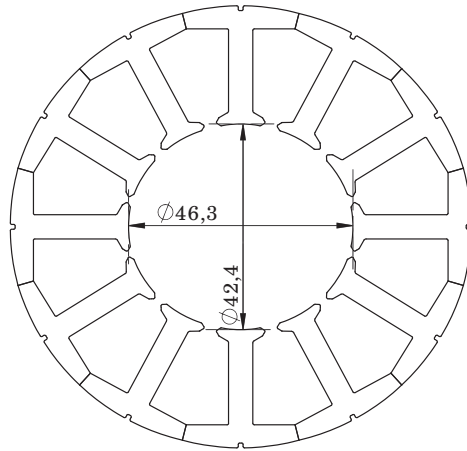


Fig. 2.20: Worst-case error of concentric run out due to tolerances of tongue and groove of 0.01 mm [24]

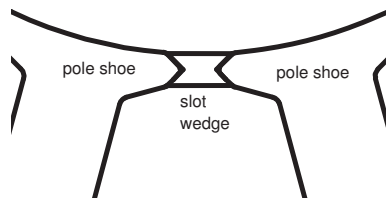


Fig. 2.21: Shape of the slot wedges [24]

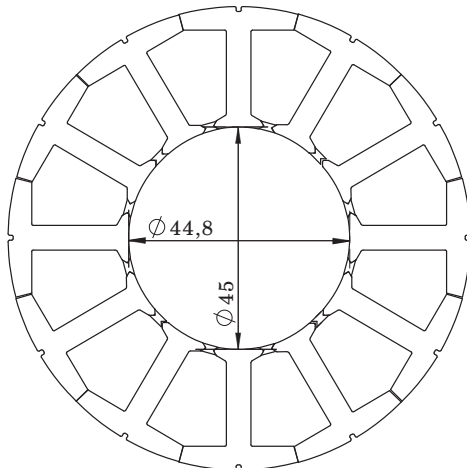


Fig. 2.22: Worst-case error of concentric run out when adding slot wedges with tolerance of 0.05 mm [24]

d_{can}	:=	Depth of equivalent can beam
t_{can}	:=	Thickness of can
l_{can}	:=	Length of can
$I_{y,\text{can}}$:=	Moment of inertia
$f_{\text{max,can}}$:=	Maximum warpage
q_{can}	:=	Area load
E_{can}	:=	Young modulus of can
σ_{can}	:=	Tension of the can

estimation of the inflection and strain between the pole shoes. Therefore, the region of the can between two teeth is considered as a beam with the following properties:

Tab. 2.10: Values for beam calculation

d_{can}	t_{can}	l_{can}	ρ_{fiber}	q_{can}	E_{can}
1 m	0.6 mm	3.28 mm	63 %	16 MPa	230 GPa [203]

By using the formulas from [26] the moment of inertia can be calculated to:

$$I_{y,\text{can}} = \frac{d_{\text{can}} \cdot t_{\text{can}}^3}{12} \quad (2.8)$$

The maximum warpage occurs at minimum Young's modulus and can be calculated by:

$$f_{\text{max,can}} = \frac{5 \cdot q_{\text{can}} \cdot l_{\text{can}}^4}{384 \cdot E_{\text{can}} \cdot \rho_{\text{fiber}} \cdot I_{y,\text{can}}} \quad (2.9)$$

Inserting the values from Tab. 2.10 results in a maximum can warpage of $f_{\text{max,can}} = 49 \mu\text{m}$. The maximum mechanical stress σ_{can} can be calculated by

$$\sigma_{\text{can}} = \frac{q_{\text{can}} \cdot l_{\text{can}}^2 \cdot t_{\text{can}}}{24 \cdot I_{y,\text{can}}} \quad (2.10)$$

which results in 239 N/mm^2 . Maximum allowable stress of the glass fiber can is $\sigma_{\text{can,max}} = 1,449 \text{ N/mm}^2$. With the fiber reduction factors presented in section 2.4.1, the maximum allowable stress reduces to $\sigma_{\text{can,red.,max}} = 179 \text{ N/mm}^2$, so it might be advisable to also use the wedges to support the can, especially when cycling the max. pressure. Cycling the pressure puts an enormous stress on the fiber/epoxy matrix. The more movement, the higher the chances that weepage might occur after a number of cycles. These very tiny holes, sometimes not even detectable, caused by fiber/epoxy matrix inhomogeneities [68], lead to pressure losses. Once weepage starts, it increases the micro cracks leading to visible failure. Hence the can was not designed with its lowest possible thickness.

The slot wedges were made of PolyPhenylene Sulfide (PPS) with 40 % glass fiber content. This material is machinable with appropriate tolerances (0.05 mm) and has sufficient strength [198], while high stiffness is achieved through the shape. The slot wedges

hold up at keys at the end of the pole shoes. In mass production the slot wedges can be manufactured by pultrusion or by injection molding. Both are high volume mass production processes.

The mechanical design, of the rotor is only explained briefly. Detailed information, e.g. shaft dimensioning can be found in [135]. Since the rotor laminations are divided into three parts, they have to be pressed onto a common tube.

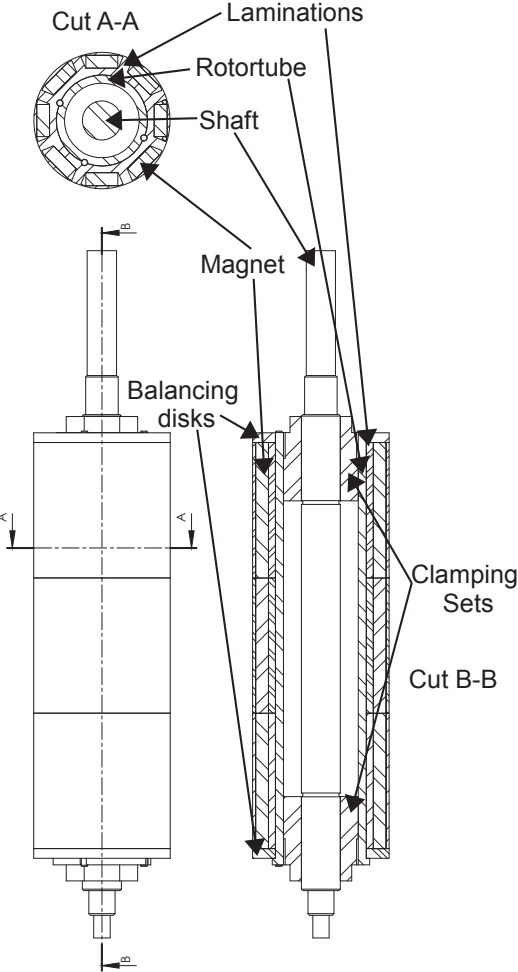


Fig. 2.23: Technical drawing of the rotor

For the final production design the shaft can be divided into output and drive shaft, so that the weight and costs can be further decreased. Currently, two clamping sets are

connecting the shaft to the rotor tube. The rotor tube is made of 1.0503/C45 standard steel and contributes to the magnetic flux conduction of the rotor yoke. Additionally, it increases the stiffness of the rotor. The positioning sensor is placed on the short end of the shaft.

2.4.3 Sensor Concept

Since the pump should be controllable at around 0 RPM, a simple hall sensor concept was found to have an insufficient resolution for the demands of the ESS. Additionally, the rotor is completely encapsulated, so the sensor electronics should be placed outside the pressurized vessel. Therefore, a Giant Magneto Resistance (GMR) positioning sensor [168] combined with a diametral magnetized magnet mounted on the shaft is used. The magnet is generating a rotating magnetic field which is strong enough to be detected through an aluminum wall (see Fig. 2.24).

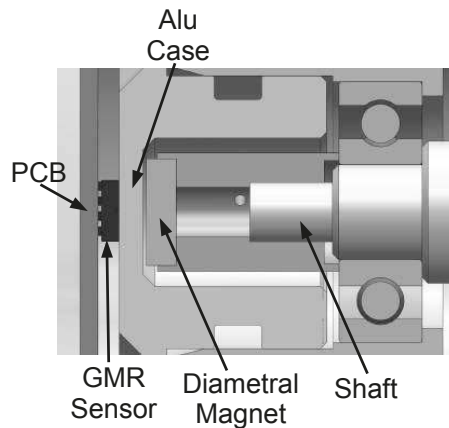


Fig. 2.24: GMR sensor concept

The wall has to be thin enough to ensure that the magnetic field remains detectable, but thick enough to withstand the maximum pressure of 160 bar. For this reason, EN-AW 7075-T6 aluminum, which provides high strength, was used for the case structure. The sensor TLE 5012 allows field variations only in certain tolerances [167]. Therefore the field dependence on temperature, as well as eddy currents induced at higher speeds, were investigated in detail and found to be acceptable. For even higher pressures, the magnet as well as the aluminum thickness may be increased.

2.5 Production and Assembly of the Motor Parts

The mechanical layout of the motor can be separated into the design of several parts like stator, rotor, housing and can. In the following sections, it is shown how the parts

are built up for the prototype, and how this might be done in mass production. The housing is not investigated because of the lack of experience in aluminum casting. One focus of this thesis is the optimization of the stator in terms of winding. Therefore in chapter 3, the mechanical and thermal improvements by different aspects of winding technology are shown. The following section details the winding setup and the production technique of the electric and magnetic active parts.

2.5.1 Winding

As decided earlier, the stator is separated into single T-segments and wound with a linear winding machine. Winding is one of the more complex aspects in motor production and design, and has a big impact in the thermal behavior of the final product. In this section, the winding setup as well as the winding scheme is presented.

For automated winding scheme design a MATLAB[®] toolbox is written, which fills a single tooth with variable geometry with orthocyclic windings, and calculates the electric resistance of the windings. The following winding rules, also mentioned in [24], are programmed into the toolbox, which are derived from practical experience with linear winding machines:

- Winding is usually started from the outside of the stator
- For delta connection of the phases, the beginning and end position, should be the same
- For wye connection of the phases, it can be useful to start and stop at different sides, to connect one side to the phase connection ring and the other side to the neutral connection ring
- The wire offset is usually limited to 2 wires to prevent slinging of its designated position, (see Fig. 2.26)
- Enough space has to be foreseen for the phase insulation paper
- To get a better foothold when doing large wire offsets, the wires should have additional space, about 25 μm on each side
- Multi filar winding should only be done if the number of wires in the layer is a common multiple of the number of filar wires

The winding geometry designed by the toolbox is shown in Fig. 2.25. Common adjacent wire colors signal filar winding. The two vertical lines in the middle (in red) show the needle space that would be necessary if the tooth is not separated and wound by needle winding. All other straight lines describe the winding window boundaries. Overlap of the wires, which enables the modeling of deformation described in section 3.2 can be also specified inside the toolbox.

The toolbox is able to write a script which assembles an ANSYS[®] Workbench geometry that can be simulated afterwards within a thermal FEA.

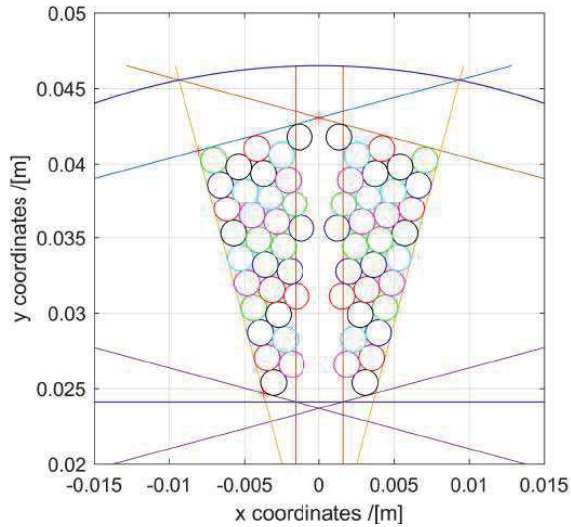


Fig. 2.25: Example winding geometry generated by MATLAB® Toolbox

In this particular case, the first proposed winding scheme is shown in Fig. 2.26. The winding order of wire 25 and 26 is switched. This change is called wire gap winding. It is necessary to limit the wire offset. The first proposed winding scheme from Fig.

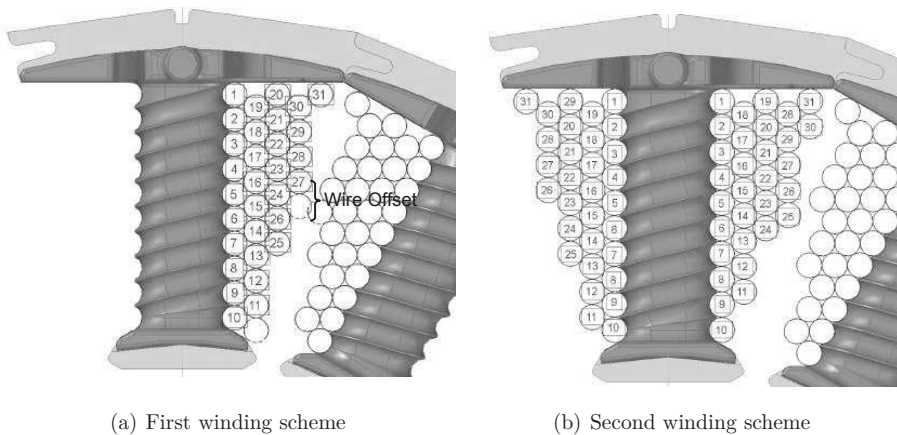


Fig. 2.26: First and second winding scheme

2.26(a) did not work out, because the wire slipped off from position 27 to the sketched wire below. So a second winding scheme was applied as shown in Fig. 2.26(b), where the two sides are wound differently.

Winding of the teeth is done with the help of the company Aumann. The linear winding machine setup can be seen in Fig. 2.28. The tooth is mounted on the spindle.

A counter support prevents the tooth from being deformed by the wire tension. Both tools are shown in Fig. 2.27. The 1.6 mm copper wire is tightened by an active wire tensioner with a force of 100 N. The big advantage of linear winding is, that the wire

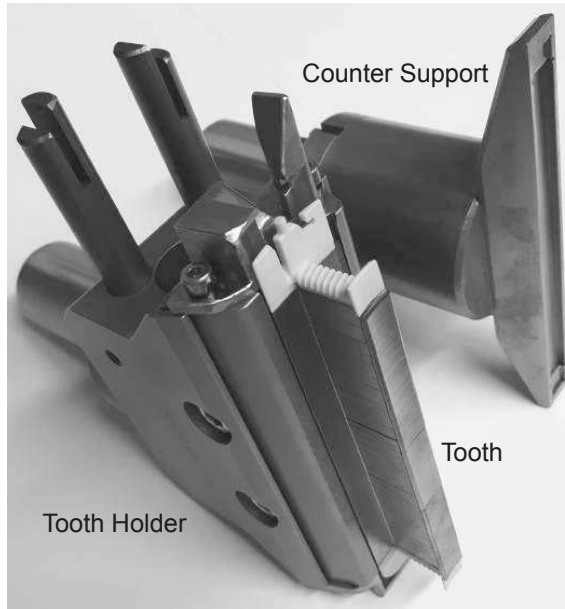


Fig. 2.27: Tooth holder and Counter Support

leaves the needle with a wider angle compared to needle winding. This decreases the mechanical stress on the wire, preventing insulation faults. In Fig. 2.29 the wound tooth is shown. On the left side of the tooth shown in Fig. 2.29(b) the impact on wire gap winding on the end windings can be seen. On that side, the wires are not orthocyclic anymore because of the switched positions of wire 24 and 25.

2.5.2 Magnet Fixation

While for SPM rotors the magnets can be picked and placed magnetized [72], IPM machines are usually inserted non magnetized because of the attraction of permanent magnets to ferromagnetic objects. The magnets are falling into the pockets and have to be fixed afterwards.

There are several ways to fix the magnets inside the rotor steel. [129] proposes a method by which the magnets are held in their pockets by punching the very thin steel above, supporting the magnets. This is a very cheap solution if the magnets are not buried too deep inside the rotor steel. While [1] proposed several caulking methods for fixing the magnets, it was found that this method damages the magnets too much because of mechanical tolerances. A sacrificial layer has to be applied to provide good strength, even at low caulking forces, which results in an additional air gap.

For a prototype, it is easier to glue the magnets. Hot-setting epoxies [152] provide

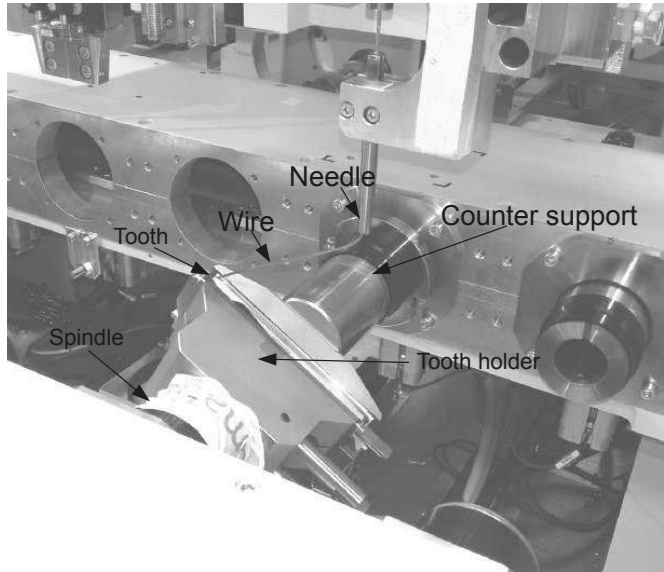
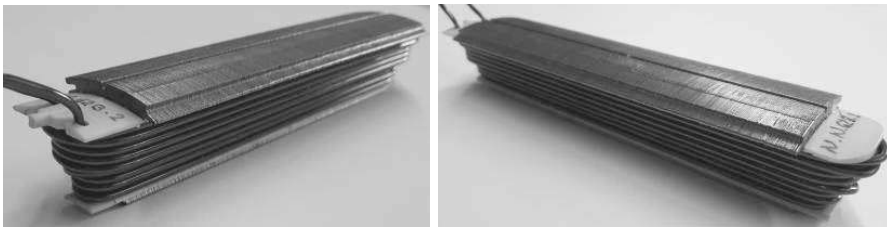


Fig. 2.28: Winding machine setup



(a) Front

(b) Back

Fig. 2.29: Wound single tooth

good strength over a wide range of temperatures, but are too expensive for mass production and have long curing times. Therefore, the magnets are usually fixed by an injection molding process using a thermoplastic [1]. To fix the magnets at the designated position, small fillets can be introduced into the lamination design (see Fig. 2.30(b)). These will position the magnets inside the rotor with low tolerances and cause small flux losses.

The magnets for the investigated prototype rotor are glued with DELO-Monopox AD066 [152] (see Fig. 2.30(a))

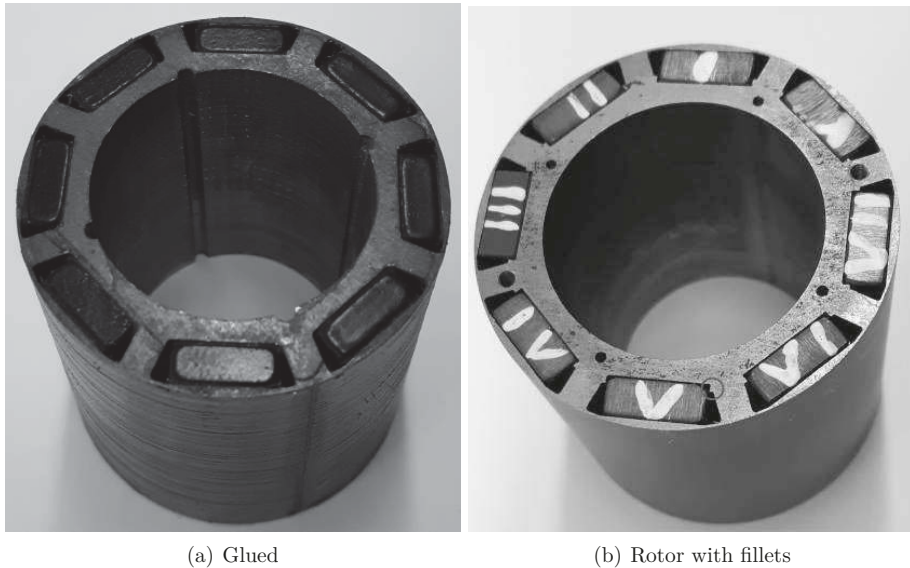


Fig. 2.30: Glued magnets and rotor with fillets

The rotor laminations are also manufactured using baking lacquer laminations. These are stacked with alternating rolling orientations, so that every magnet is subject to the same magnetic resistive path.

2.5.3 Can Production

The prototype cans of carbon and glass fiber are wound circumferentially with an angle of almost 90 degree (see Fig. 2.9) around a hollow stainless steel mandrel. The cans are cured afterwards in an oven at around 90 °C and removed from the mandrel by cold water flushing through the hollow mandrel. Afterwards the cans are polished from the outside with a tolerance of ± 0.03 mm. In mass production, grinding with such tolerances is too expensive, so another production method like Resin Transfer Moulding (RTM) should be applied here. A detailed explanation would go beyond the focus of this thesis, further information can be found in [80, 95].

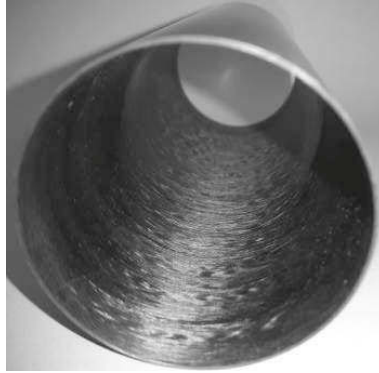


Fig. 2.31: Carbon can from inside

2.5.4 Connection Ring

The connection ring is usually the last part that is designed and sometimes results in a complex connection solution. The ESS Motor is designed such that a very thin connection ring consisting of 3 phase rings is used to carry the current to high current copper plugs (see Fig. 2.32). For testing purposes, the copper wires are screwed to the connection ring, enabling easier removal of the teeth. In production, the copper wires would be brazed [201] onto the connection ring.

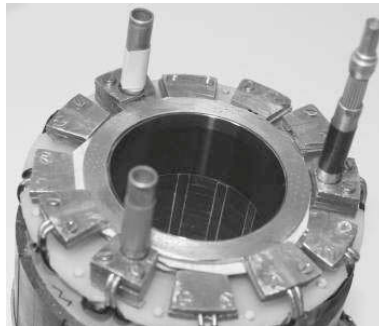


Fig. 2.32: Prototype screwed connection ring with connection plugs

During the making of this thesis, two studies were conducted on how to integrate the connection ring into foldable power electronics [134, 142]. This enables a compact combined power electronics motor package and the omission of the high current connection plugs.

2.5.5 Stator and Rotor Assembly

First, the stator is assembled out of twelve teeth, and the wedges are inserted. These wedges control the circularity and make sure that the can is not subject to additional

mechanical stress coming from dimensional variations of the teeth. Afterwards the can is inserted and glued with flexible silicon glue [174] (see Fig. 2.33). This silicon glue can be dispensed very thinly and is able to fill gaps which might occur due to dimensional variation of stacking of the laminations. Since the glue is flexible, the can itself is taking over some stress while expanding. Because the Young modulus of the glass fiber can is smaller compared to steel, the can will be expanded due to the pressure of the fluid. Due to the expansion, the can will touch the stator which starts to take over the force at this point. Adjusting this is difficult, since it depends on the maximum or minimum tolerances of the can and stator teeth. Therefore, the stator and the housing are designed to be able to take over the whole stress caused by the pressure. When the can is lubricated with the glue, it is positioned inside the stator. Then spring clamps around the outer stator are used to press the teeth's tongue and groove into the final position.

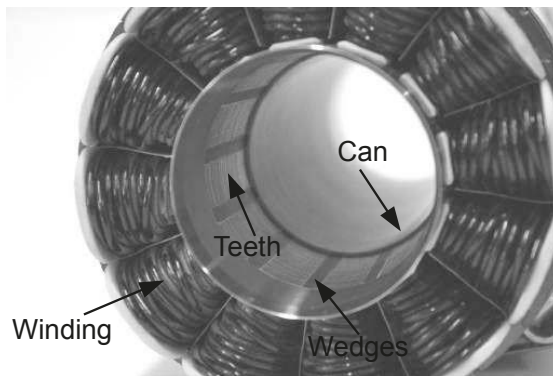


Fig. 2.33: Teeth and wedges assembly with half inserted can

The connection ring is positioned on the end caps and the wires are connected. Due to delta winding, two adjacent winding wires can be connected to each other. Afterwards the stator is shrunk into the stator housing.

After the rotor laminations are equipped with magnets they are pressed on the rotor tube together with the balancing disks and rotationally fixed with pins. The shaft is connected with clamping sets [161] for the prototype. In mass production this fixture is done by shrinking.

On the front side of the shaft shown in Fig. 2.34 a sensor magnet is glued into a brazen holder which is screwed onto the shaft.

2.6 Simulations

In this section, most of the simulations which will be verified later by measurements are presented. All of them were conducted at 20 °C because the measurements will be

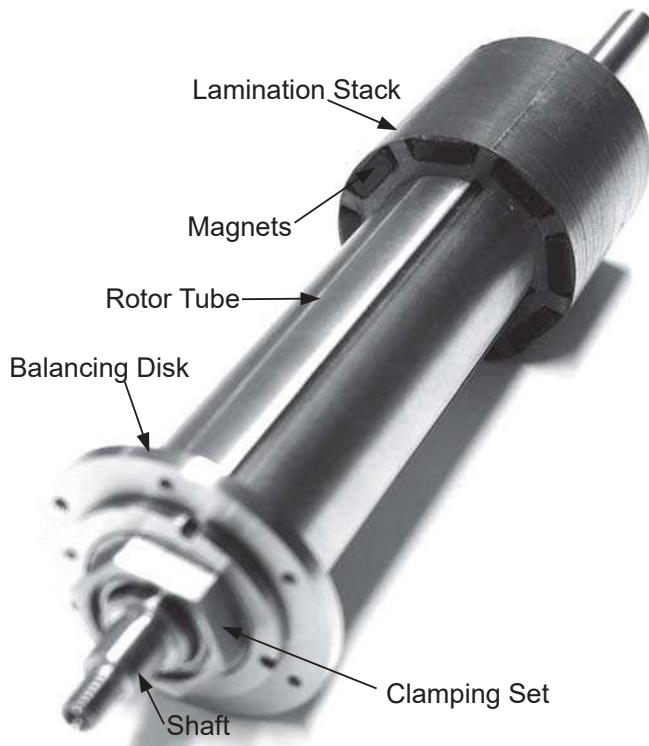


Fig. 2.34: Rotor Assembly with one Lamination Package

done at the same temperature. Because of the focus on thermal improvements in this thesis, thermal simulations are presented in a separate chapter 3.

2.6.1 Efficiency and Loss Simulations

Efficiency simulations considering Maximum Torque Per Ampere (MTPA) and Maximum Torque Per Watt (MTPW) strategies are conducted co-transient with Maxwell[®] and Simplorer[®]. In Fig. 2.35 the simulated efficiencies vs. motor torque and speed are shown. In Fig. 2.36 and 2.37 the total, copper, iron and magnet losses are shown, respectively. As can be seen, the copper losses increase when looking at higher speeds but constant torques. This is due to the current needed for field weakening. The iron losses increase according to theory, with frequency and saturation up to a maximum of 39 W. The magnet losses increase with speed and saturation of the iron. At low speeds, they are very small compared to the copper losses. The magnet losses are also small thanks to the small slot openings, which enables good fringing of the magnet flux and therefore lower frequencies inside the air gap. Higher speeds were not recorded due to the limitations of the test bench.

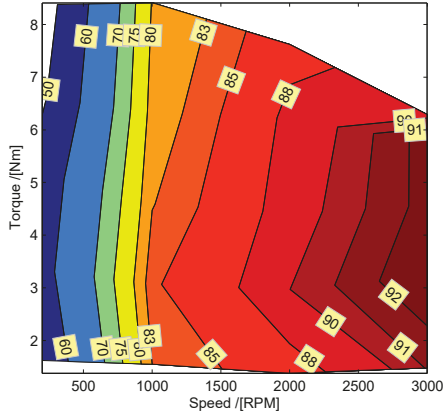


Fig. 2.35: Theoretical efficiency map $\eta_{\text{theoretical}}$ in [%] of motor vs. torque and speed at 38 V DC Link voltage

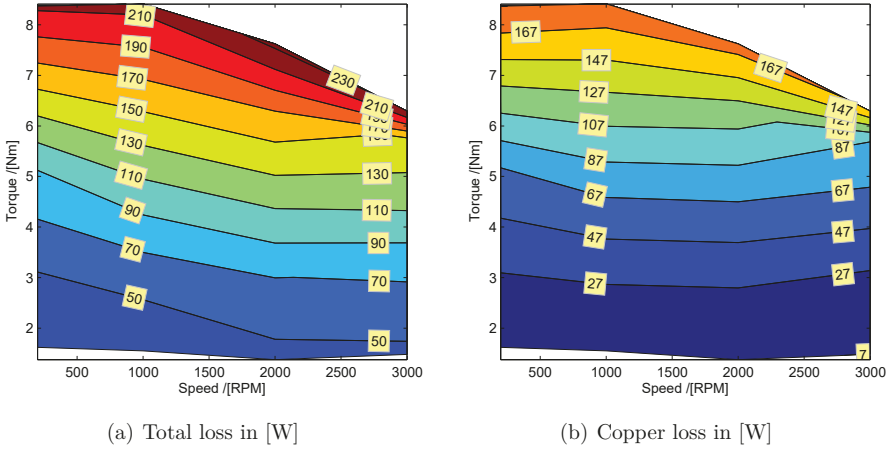
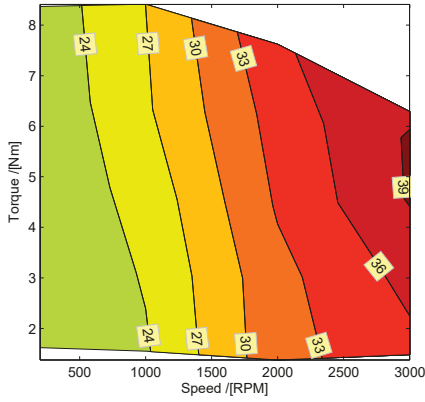


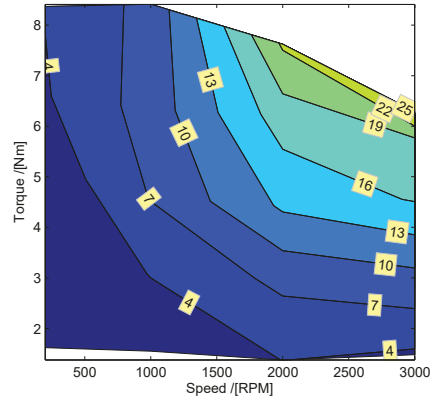
Fig. 2.36: Total and copper losses in [W] of motor vs. torque and speed at 38 V DC Link voltage

2.6.2 Cogging Torque Simulations

The cogging torque effect is well known and studied [21, 58, 124, 126, 127]. As calculating cogging torque analytically is difficult due to fringing of the magnetic flux, an FEA is conducted. In Fig. 2.38 the cogging torque is shown with maximum torque of about 570 mNm, which is acceptable for this pump according to the specifications.



(a) Iron loss in [W]



(b) Magnet loss in [W]

Fig. 2.37: Iron and magnet losses in [W] of motor vs. torque and speed at 38 V DC Link voltage

Skewing of the three rotor parts is an option to reduce the cogging as explained in [21], and could be introduced in the next iteration of the pump.

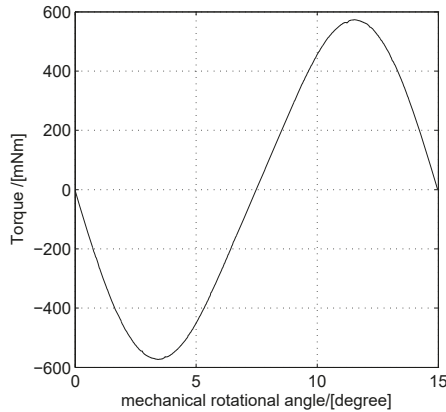


Fig. 2.38: Simulated cogging torque vs. mechanical rotational angle of the rotor

2.6.3 Equivalent Circuit

The resistance is determined to be $R_{ph} = 12.8 \text{ m}\Omega$ at $20 \text{ }^\circ\text{C}$. The direct and quadrature inductances L_d, L_q , are obtained within an FEA with the formulas from [6]. Absolute

values of L_d and L_q with respect to any current can be calculated by:

$$\Psi_d = \frac{2}{3} \left[\Psi_u \cos \vartheta_r + \Psi_v \cos \left(\vartheta_r - \frac{2}{3}\pi \right) + \Psi_w \cos \left(\vartheta_r - \frac{4}{3}\pi \right) \right] \quad (2.11)$$

$$\Psi_q = \frac{2}{3} \left[\Psi_u \sin \vartheta_r + \Psi_v \sin \left(\vartheta_r - \frac{2}{3}\pi \right) + \Psi_w \sin \left(\vartheta_r - \frac{4}{3}\pi \right) \right] \quad (2.12)$$

$$I_d = \frac{2}{3} \left[I_u \cos \vartheta_r + I_v \cos \left(\vartheta_r - \frac{2}{3}\pi \right) + I_w \cos \left(\vartheta_r - \frac{4}{3}\pi \right) \right] \quad (2.13)$$

$$I_q = \frac{2}{3} \left[I_u \sin \vartheta_r + I_v \sin \left(\vartheta_r - \frac{2}{3}\pi \right) + I_w \sin \left(\vartheta_r - \frac{4}{3}\pi \right) \right] \quad (2.14)$$

$$L_d = \frac{\Psi_d}{I_d} \quad (2.15)$$

$$L_q = \frac{\Psi_q}{I_q} \quad (2.16)$$

- Ψ_d := Linked flux in direct direction
- Ψ_q := Linked flux in quadrature direction
- $\Psi_{u,v,w}$:= Linked flux of each phase
- ϑ_r := Electric rotor angle
- I_d := Current in direct direction
- I_q := Current in quadrature direction
- $I_{u,v,w}$:= Current in each phase
- L_d := Synchronus direct inductance
- L_q := Synchronus quadrature inductance

In Fig. 2.39 the inductance with respect to peak current is shown. As can be seen the saturation starts at 40 A and is continuous until L_d and L_q approach each other.

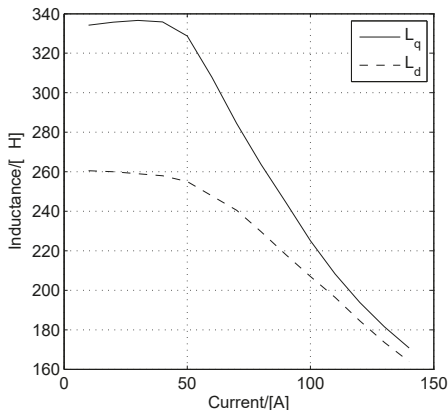


Fig. 2.39: Simulated inductances L_q and L_d vs. peak current

The EMF shown in Fig. 2.40 is not trapezoidal due to the small slot openings which cause a high amplitude of the fifth harmonic, resulting in the buckled trapezoidal curve shape.

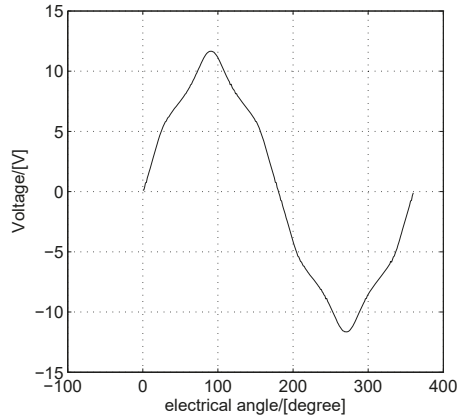


Fig. 2.40: Simulated EMF at 1000RPM, derived for rotor position

2.6.4 Current curve Shape and Control

The current shape for this motor will only be discussed very briefly, because it is a control scheme related topic and therefore not in the main focus of this thesis. More detailed information can be found in [138].

For the motor, the control scheme C60Q6 was chosen. This scheme is known very well and described in [53]. It provides equal switching power loss distribution among all power semiconductors. The PWM frequency is set to 25 kHz to decrease the current ripple. MTPA and MTPW were used to increase the efficiency and are described in detail in [137]. To detect the parameters for MTPA and MTPW, several working points in a close grid were remnant and measured.

2.6.5 Circulating Currents

Circulating currents are very important when investigating delta connected stators. A complete survey about the investigated stator including all mechanical and electric tolerances can be found in [23]. It was found that a 12 slot and 8 pole combination is not influenced much by mechanical tolerances. A 12 slot 10 pole combination will suffer from circulating currents.

3 Materials and Manufacturing

Methods for thermal Optimization

A motor with low winding temperatures, which are usually the hot spots, can be reduced in size. On the other hand, low temperatures inside the windings come together with lower magnet temperatures which results in lower necessity of HREE. Using less HREE magnet material results in a significant price reduction of the whole motor. Hence, motor temperature has to be reduced. One of the goals of this thesis is to find inexpensive and easy to use solutions to decrease the temperature inside the motor. In low speed permanent magnet synchronous motors copper losses are predominant as shown in section 2.6.1. The heat has to be conducted through the wire insulation material, pass possible air gaps between the wires, pass the slot insulation liner and has to be conducted through the stator tooth, yoke and housing (see Fig. 3.1). Reducing the temperature can be done by either improving the insulation system, or by manufacturing of the windings.

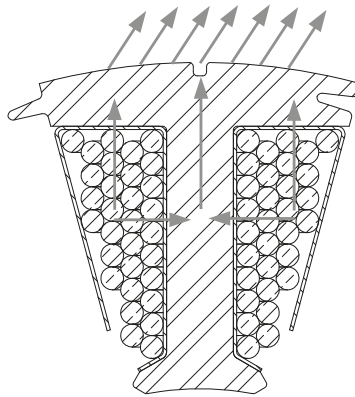


Fig. 3.1: Thermal path of the heat for a single tooth from windings to yoke and air (fins and housing not included)

3.1 Thermal impact of Insulating Material

For many years the insulation systems of electric machines has not changed much [109]. Common insulation systems have been developed by Dupont[®] or 3M[®]. As mentioned

in chapter 2 the insulation system along with the outer cooling are the key factors of the machine size. Common industrial insulation systems are limited by 200 °C [188] usually because of the maximum temperature of the insulation of enameled winding wires. According to DIN EN 60172 [155], the temperature class of enameled winding wires is defined as "the temperature in [°C] that is hit by the regression line at the 20,000 h straight". In the automotive industry, a lifetime of just 5,000 h-6,000 h has to be achieved. According to the Arrhenius law, the lifetime of an insulation material is halved if the temperature is increased by 10 K. This means that the continuous temperature of the winding for automotive lifetimes might be increased.

3.1.1 Enamelled Winding Wire

The most common enameled winding wires in automotive industry are class 155 to class 200 wires. Some very common enameled winding wire insulations are:

- Class 155 wire

insulation: polyurethane [170]

breakdown voltage: >7 kV for a 0.8 mm wire [170]

thermal conductivity of insulation: 0.27 W/mK [2]

thermal conductivity of copper wire: 381 W/mK [60]

- Class 200 wire

insulation: polyester/polyamide THEIC [188]

breakdown voltage: >8.5 kV for a 1 mm wire [188]

thermal conductivity of insulation: 0.28 W/mK [2]

thermal conductivity of copper wire: 381 W/mK [60]

- Class 200 backing wire

insulation: polyester/polyamide THEIC [187]

backing lacquer: acyclic polyamid [166]

breakdown voltage: >8.0 kV for a 1 mm wire [187]

thermal conductivity of insulation: 0.28 W/mK [2]

thermal conductivity of backing lacquer: 0.31 W/mK [52]

thermal conductivity of copper wire: 381 W/mK [60]

In several cases it makes sense to use backing wire, which is normal, enameled winding wire with a lacquer, usually made of polyvinylbutyral for class 155 wire, phenoxy resin for class 180 wire and acyclic polyamide for class 200 wire [166].

3.1.2 Slot insulation Liner

The slot insulation liner is the second electrical insulation of the wires against the tooth. It is very important because the laminations can sometimes be quite rough due to mechanical tolerances. When considering mechanical vibrations, it is obvious that a burr of a lamination sheet might damage the very thin insulation lacquer ($11\ \mu\text{m}$ - $54\ \mu\text{m}$) [156] of the enameled winding wire. Typical insulation liner for automotive purposes can be categorized in several groups:

- Polyester papers

breakdown voltage: $>43\ \text{kV/mm}$ [157]

thermal conductivity: $0.155\ \text{W/mK}$ at $75\ ^\circ\text{C}$

very good mechanical stability

max. continuous temperature $155\ ^\circ\text{C}$ (class 155)

- Aramid papers

breakdown voltage: $>18\ \text{kV/mm}$ [158]

thermal conductivity: $0.139\ \text{W/mK}$ at $150\ ^\circ\text{C}$ for a $0.25\ \text{mm}$ paper

very good mechanical stability

max. continuous temperature $180\ ^\circ\text{C}$ (class 180)

Die cast insulations are also very common. In this case, thermoplastics can be used:

- Polyamide (PA)

breakdown voltage: $>24\ \text{kV/mm}$ [185]

thermal conductivity: $0.26\ \text{W/mK}$

max. continuous temperature $155\ ^\circ\text{C}$ (class 155)

- PPS

breakdown voltage: $>24\ \text{kV/mm}$ [184]

thermal conductivity: $0.3\ \text{W/mK}$

max. continuous temperature $180\ ^\circ\text{C}$ (class 180)

PolyEther Ether Ketone (PEEK) is sometimes used when higher mechanical forces at low temperatures are required. PEEK loses most of its mechanical strength when the temperature rises above the glass transition temperature of $150\ ^\circ\text{C}$ [204]. Better results give PPS with glass fiber enforcement. Also PPS has a low glass transition temperature but loses less mechanical strength compared to PEEK.

Silicone insulation papers with ceramic flakes like Al_2O_3 have become quite popular in power electronics in recent years. Adding a glass fiber layer for mechanical stability makes it an interesting alternative for common insulation systems. Additionally these

papers are flexible and adapt to the form of the first layer of the windings. Consequently, the thermal contact can be improved.

- Flexible silicone paper with ceramic flakes (Keratherm®)[172]

breakdown voltage: >26 kV/mm

thermal conductivity: 1.8 W/mK, with glass fiber layer 1.06 W/mK

very good mechanical stability

flexible

max. continuous temperature >200 °C

3.1.3 Potting

A way to enhance thermal performance is potting. Potting allows to fill air gaps between liner and windings as well as between the conductors. In small electric motors, this is usually done with quasi vacuum impregnation [114]. Depending on the viscosity of the used resin, it can be difficult to fill all gaps in limited time. In many talks with automotive companies and suppliers, it turned out that a lot of companies would like to waive the use of any potting material. Therefore, this study does not focus on potting material. Nevertheless, for comparability, several tests with epoxy were conducted, too. The epoxy used is Elantron® MC 5470 FR/W 5710 [159]. It provides high strength and good thermal conductivity:

- Elantron® MC 5470 FR/W5710 [114, 159]

breakdown voltage: >19 kV/mm

thermal conductivity: 0.9 W/mK

Coefficient of thermal expansion (CTE): 35 ppm/K

viscosity at 25 °C: 6 Pa s - 10 Pa s

high crack and shock resistance

3.1.4 Electrical Steel

Thermal properties of electrical steel depend on the Si or Al content. In [145] it is mentioned that the thermal conductivity of M400-50A drops from 48 W/mK at 0.49% Al & Si content to about 25 W/mK- 30 W/mK at 3.5% . This can be explained by the disturbed grain structure, which usually leads to a higher electric resistivity. [53] proposes a conductivity of 20 W/mK- 30 W/mK. [147] measured a thermal conductivity by Xenon flash of 25 W/mK for an AISI M19-26GA which corresponds to an EN 10106 M270-60 steel. In the upcoming calculations, a thermal conductivity of 30 W/mK is assumed. Compared to other conductivities, e.g. the liner, steel has a low thermal resistance.

3.2 Thermal impact of Manufacturing Methods

Looking at the typical linear winding process, there are several things that have to be considered for the thermal path:

- How far are the windings away from the slot liner?
- Are there any air gaps from one wire layer to the next?

Air is one of the poorest thermal conductors $k_{\text{air}}=0.026 \text{ W/mK}$ [60]. Therefore any air gaps have to be avoided. However pure linear winding of single tooth leads to the so called wire belly (see Fig. 3.2).

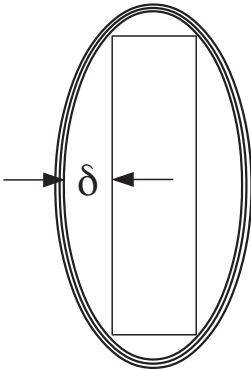


Fig. 3.2: Schematic wire form wound with linear winding technology



Fig. 3.3: Schematic wire form wound with the technique introduced in [132]

This can be partially avoided when using a technique introduced in [132], where an extra pin preforms the wire, so that it becomes contour conform. Unfortunately, the wire still does not completely touch the insulation liner over the whole length of the tooth (see Fig. 3.3).

Another technique introduced in [61] solves the mentioned problem, by pressing the windings and simultaneously heating them up by a current. The heat is used as a partial mechanical stress relief. After heating, the pressed wires stay at their designated position and do not spring back as much as without heating. Therefore, also higher fill factors are possible. The wound teeth would not fit next to each other without pressing. Therefore, a pressing device is developed. Pressing for the prototype windings is done with a common parallel vice, which has a load cell between the pressing brackets and the jaw. The maximum pressure was found by trial and error. Therefore the wound tooth was pressed and the insulation material checked for possible damages after unwinding. The maximum force before insulation failures occur was found to be 16 kN. The brackets which are adapted to the winding outer layers can be seen in Fig. 3.5. The pressing setup is shown in Fig. 3.6.

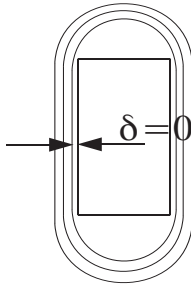


Fig. 3.4: No wire belly after pressing

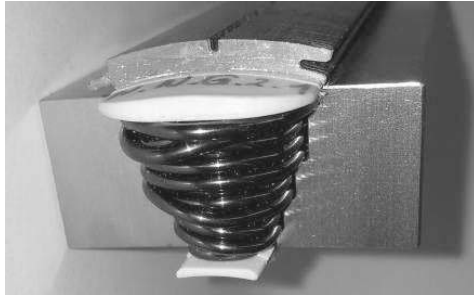


Fig. 3.5: Pressing brackets with tooth

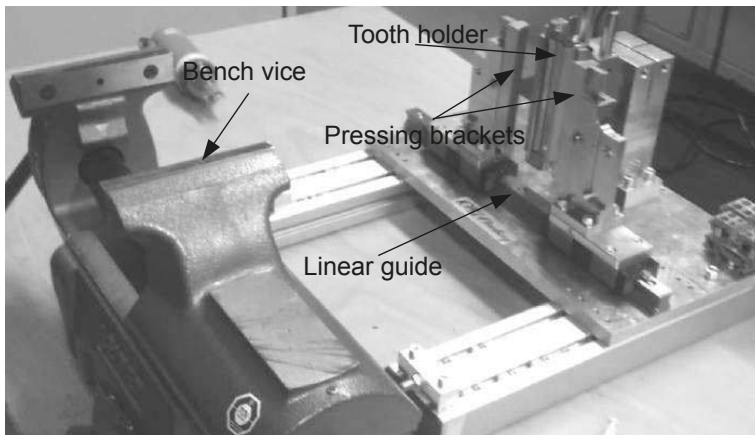


Fig. 3.6: Pressing Setup

The current was provided by a current controlled IGBT half bridge. The voltage drop over the coils was measured before and during heating. By doing this, it is possible to estimate the temperature inside the coils automatically without the need of a temperature sensor. To be independent of the capacitance of the tooth and hence avoiding local hot-spots inside the winding it is important to heat up the coil very quickly. This can also be advantageous for maximizing the throughput in mass production. When

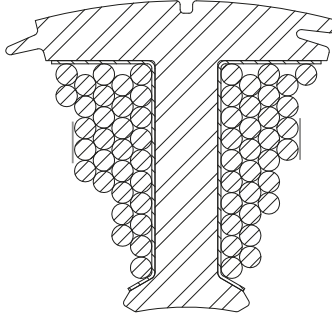


Fig. 3.7: Cross section of winding on single tooth; distance measurement points left and right markings

looking at the gap between the first winding, layer and insulation paper it can be stated from experience that the relaxation of the copper wire is not dependent on the heating speed, it is just dependent on the end temperature and the applied pressure. This was proven by various experiments. Pressed and non-pressed dimensions between the red bars shown in Fig. 3.7 can be found in Tab. 3.1. The difference is shown for conventional class 200 wire without backing lacquer. For relaxation it was found that a temperature of 150 °C is sufficient. Higher temperatures of 200 °C were applied just for the backing wire.

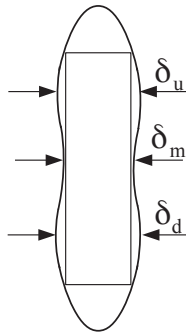


Fig. 3.8: Wire Pressing Dimensions

Tab. 3.1: Average dimension of pressed and non pressed teeth between the red bars seen in Fig. 3.7; class 200 wire without backing lacquer used

Tooth	δ_u	δ_m	δ_d
Pressed	17.6 mm	17.54 mm	17.56 mm
Non-pressed	19.84 mm	19.19 mm	19.28 mm

Using backing wire, the gaps between the first layer and the insulation paper reduce to

non-measurable thicknesses. When analyzing the other two wire insulation materials, a small belly similar to the one shown in Fig. 3.3 can be seen from the outside. This can be explained by the spring-back of the wire after pressing and relaxing.

3.3 Thermal Model

A thermal model for the different insulation materials and the impact of the improved winding technology has to fulfill the following criteria:

- Different insulation material
- Backing wire and epoxy
- Flexibility of the liner insulation paper
- Contact area of the wires among themselves
- Non circular wires because of wire pressing
- Distance between first layer and winding

Several thermal models are available [10, 105]. One of the most popular thermal motor models is the layer model [11, 107], which gives very good results for common industrial standard motors. The winding window is divided into layers of the different materials. The thickness is chosen based on the volume of each material. Unfortunately, this model does not include any contact resistance or wire deformation parameters. Hence, for this investigation, it is not suitable.

A better solution is the modeling of each wire and the insulation material. This can become very difficult when it comes to non circular wires, which emerge by pressing and heating. Modeling each deformed wire and its insulation material is difficult. A better solution is the assumption of a common copper+insulation material for simulation.

3.3.1 Combined Wire Insulation Material

Combining the wire insulation material together with the copper into a mathematical expression has many advantages when doing a thermal FEA. First, the minimum tetrahedron size can be bigger compared to a small insulation around the copper wire, which saves time. Second, the deformation of the wire can be modeled as an overlap of the wires, without having to model the real shape. Third, increased contact area between the slot liner insulation material and wire can be modeled as well. A combined thermal conductivity k_3 for the wire and wire insulation has to fulfill the following requirements:

- When assuming a loss density inside the copper, the outer wire insulation temperature of the simplified model has to match the physical one when the inner temperature is given as a boundary
- The same is true when assuming an outer temperature boundary

In Fig. 3.9 the boundaries for the copper and insulation material as well as the combined version is shown. The combined insulation and copper material will have an orthotropic thermal conductivity, k_3 in x- and y-direction and k_1 in z-direction. To

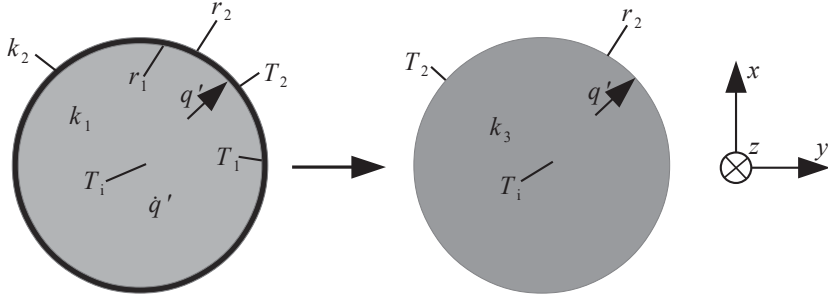


Fig. 3.9: Combined insulation material boundaries

- T_i := Maximum inner wire temperature
- T_1 := Copper temperature at r_1
- T_2 := Copper temperature at r_2
- \dot{q}' := Heat generation density per meter
- k_1 := Thermal conductivity of copper
- k_2 := Thermal conductivity of wire insulation material
- k_3 := Thermal conductivity of equivalent copper and insulation material in x- and y-direction

find out the correct $k_3=f(k_1, k_2, r_1, r_2)$ one has to start with the diffusion differential equation in cylindrical coordinates [60]:

$$\frac{1}{r} \frac{d}{dr} \left(r \frac{dT}{dr} \right) + \frac{\dot{q}'}{k_1} = 0 \quad (3.1)$$

$$\frac{dT}{dr} = -\frac{\dot{q}'}{k_1} \frac{r^2}{2} + c_1 \quad (3.2)$$

$$T(r) = \frac{\dot{q}'}{k_1} \frac{r^2}{4} + \ln c_1 + c_2 \quad (3.3)$$

In [60] the definition of thermal resistance per meter in cylindrical coordinates is defined as:

$$R'_{th} = \frac{T(r_1) - T(r_2)}{\dot{q}'} = \frac{\ln \left(\frac{r_2}{r_1} \right)}{2\pi k_2} \quad (3.4)$$

$$\dot{q}' = \int_0^{2\pi} \int_0^r \dot{q}' r dr d\varphi \quad (3.5)$$

Assuming that $\frac{dT}{dr}|_{r=0} = 0$, c_1 becomes 0 (3.3). Setting T_i as the maximum temperature at $r = 0$:

$$T(r = 0) = T_i = \frac{\dot{q}'}{4k_1}r^2 + c_2 \quad (3.6)$$

$$\Rightarrow c_2 = T_i \quad (3.7)$$

$$T(r = r_1) = -\frac{\dot{q}'r_1^2}{4k_1} + T_i \quad (3.8)$$

Inserting formula 3.8 into 3.4:

$$\frac{(\frac{\dot{q}'r_1^2}{4k_1} + T_i) - T_2}{\dot{q}'r^2\pi} = \frac{\ln(\frac{r_2}{r_1})}{2\pi k_2} \quad (3.9)$$

$$T_2 = \frac{\ln(\frac{r_2}{r_1})}{2\pi k_2}\dot{q}'r_1^2\pi - \frac{\dot{q}'r_1^2}{4k_1} + T_i \quad (3.10)$$

Now assuming a conductor with a single thermal conductivity as shown on the right side of Fig. 3.9.

$$T_2 = -\frac{\dot{q}'r_2^2}{4k_3} + T_i \quad (3.11)$$

In that case formulas 3.10 and 3.11 can be equalized:

$$\frac{\ln(\frac{r_2}{r_1})}{2\pi k_2}\dot{q}'r_1^2\pi - \frac{\dot{q}'r_1^2}{4k_1} + T_i = -\frac{\dot{q}'r_2^2}{4k_3} + T_i \quad (3.12)$$

Solving for k_3 :

$$k_3 = \left[\left(\frac{\ln(\frac{r_2}{r_1})}{2k_2}r_1^2 - \frac{r_1^2}{4k_1} \right) \frac{4}{r_2^2} \right]^{-1} \quad (3.13)$$

As can be seen in formula 3.13 k_3 does only depend on material data.

3.4 Testing matrix and Equipment

This model has to be tested for accuracy by measurements and simulations. Producing several motors with different insulation material combinations is expensive, so it was decided that only single teeth windings should be investigated. When doing thermal testing of motor components, in this case one tooth, it is useful to insulate all parts that would not conduct in the final assembled motor. Since it is difficult to achieve full adiabatic boundaries, it is useful to dissipate a lot of heat through the main thermal path. That way, the error made by non perfect adiabatic conditions, e.g. at the sides can be decreased.

3.4.1 Thermal Testing Setup

The thermal testing setup is shown in Fig. 3.10. As can be seen, the surface of one tooth is cooled by air powered by a strong fan. The sides are made of Polyamide 12 which is selective laser sintered to match the tooth and winding geometry. T-Type thermocouples are mounted as shown in Fig. 3.11. The thermocouples are mounted on the tooth and windings with aluminum tape. This enables high accuracy and repeatable results compared to polyimide foil [104]. The dissipative heat inside the

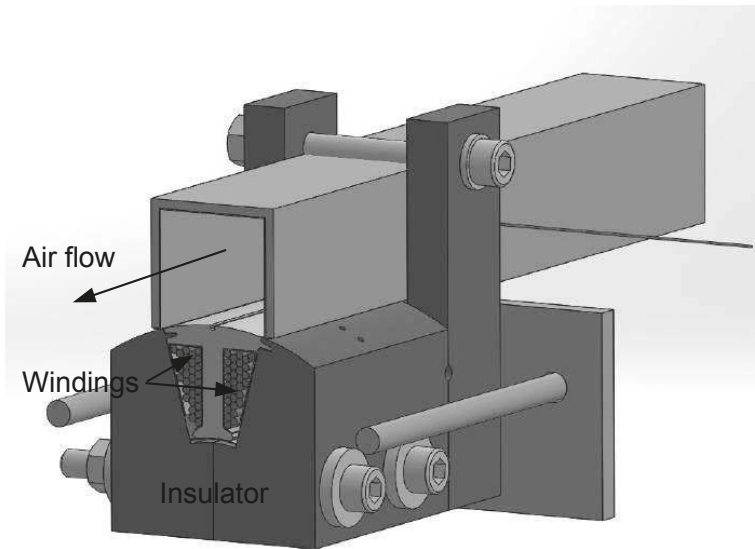


Fig. 3.10: Cut trough temperature testing setup for single tooth winding

windings was generated by an electric current. The current and the voltage at the wire terminals was measured, so that the dissipative power can be estimated. The used equipment is listed below:

- Current measurement: LEM Current Sensor and measurement resistor $100\ \Omega \pm 0.1\%$ [173]
- Voltage measurement: Fluke 8840A [162]
- T-Type thermocouple: Omega Engineering [181]
- Temperature logging: Omega Engineering HH147U [182]

3.4.2 Testing Matrix

To test the impact of each enameled winding wire insulation, liner and potting, all possible combinations were tested in the test setup mentioned. The combinations can be seen in Tab. 3.2. 1.6 mm copper wire with polyurethane (155) insulation and

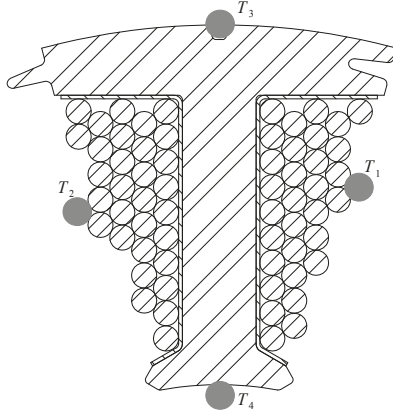


Fig. 3.11: Thermocouple placing for single tooth

Tab. 3.2: Thermal testing matrix

Code	Wire insulation	Liner	Potting	Pressing
N.N.G1.Y	polyurethane (155)	Nomex [®]	NO	Yes
N.E.G1.Y	polyurethane (155)	Nomex [®]	Epoxy	Yes
K.N.G1.Y	polyurethane (155)	Keratherm [®]	NO	Yes
K.E.G1.Y	polyurethane (155)	Keratherm [®]	Epoxy	Yes
N.N.G2.Y	polyester/polyamide (200)	Nomex [®]	NO	Yes
N.E.G2.Y	polyester/polyamide (200)	Nomex [®]	Epoxy	Yes
K.N.G2.Y	polyester/polyamide (200)	Keratherm [®]	NO	Yes
K.E.G2.Y	polyester/polyamide (200)	Keratherm [®]	Epoxy	Yes
N.N.G2B.Y	polyester/polyamide (200)	Nomex [®]	Backing Lacquer	Yes
K.N.G2B.Y	polyester/polyamide (200)	Keratherm [®]	Backing Lacquer	Yes
K.N.G2B.N	polyester/polyamide (200)	Keratherm [®]	NO	NO

backing lacquer is only available in very large quantities and therefore not tested in this thesis. From a heat removal stand point, it can be stated that if the backing lacquer for class 155 wire has the same conductivity as for class 200, both the polyurethane (155) and polyester/polyamide (200) insulation should show the same results.

3.5 Thermal Tests and Simulation Results

The tests were conducted with a controlled load current resulting in losses of about 19 W per tooth. The fan was kept at constant speed at all time, and the final ambient temperature after reaching steady state was taken as the input for the cooling air flow. Thermal steady state was reached when the temperature change was less than 0.3 °C in 10 min. The measured temperatures were compensated for increased ambient temperatures. As can be seen in Fig. 3.12, the temperatures agree very well with the simulation. It is not clear why the simulated T_4 is usually slightly bigger than the measured values, since the steel was pre-measured alone for thermal conductivity estimation. It is interesting to see, that the difference between a potted K.E.G2.Y and a non-potted N.E.G2.Y is only about 4 K at the hottest point, whereas K.N.G2.Y and N.N.G2.Y show a 8.2 K difference. This is because at higher conductivities of the material between the wires, the liner becomes the limiting factor and vice versa. As can be seen in Fig. 3.12, non pressed teeth were also thermally tested (K.N.G2.N). Normally all teeth have to be pressed because they would not fit next to each other inside the stator. As can be seen, the temperature is about 4 K-6 K higher compared to a pressed tooth. Several polished cut images at different lengths were produced to investigate the gap between the first winding layer and the liner (see Fig. 3.14). As can be seen, the wires are not as close to each other as for a pressed configuration (compare Fig. 3.13). As already described in Tab. 3.1, the maximum distance occurs near the end winding caps because of the elastic nature of copper wire (compare Fig. 3.14). It was found that with larger wire tension the belly shape of the wire can be slightly reduced - resulting in a higher electrical resistance of the wire because of the stretching. Therefore, this method should not be used. The average distance from the liner to the first winding layer is 0.2 mm. This results in a temperature difference of T_1 of 6 K and T_2 of 3.4 K. The difference of T_3 and T_4 is in the range of the measurement error. Because of the good accuracy of the model, several investigations can be done by simulation (see section 7.3).

3.6 Motor thermal Simulations

Reducing the temperature inside the windings has several effects for a wet rotor configuration. First, the heating of the working fluid surrounding the rotor can be reduced. This also leads to reduction of the magnet temperature, which in this design is set equal to the oil temperature. Because of the large surface of the stator inner bore, the motor can even be used to cool the oil. Tab. 3.3 shows the resulting temperatures at a nominal torque of 10.4 Nm and 1,000 RPM as well as 15 km/h driving speed and 80 °C

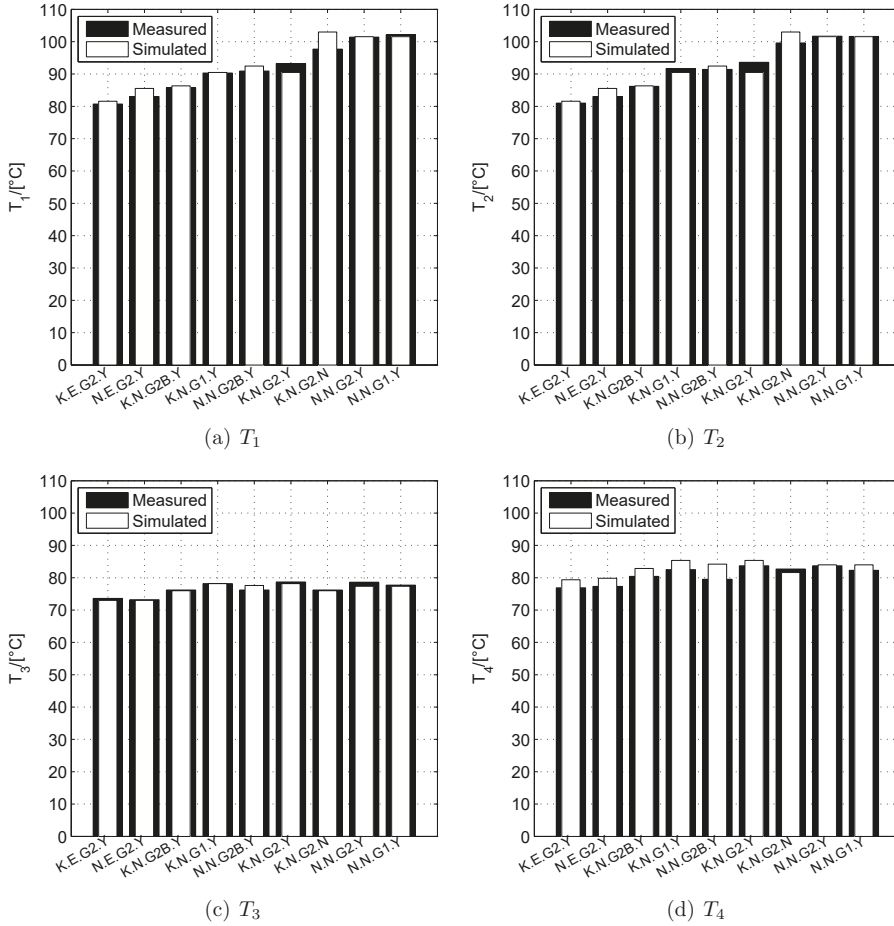
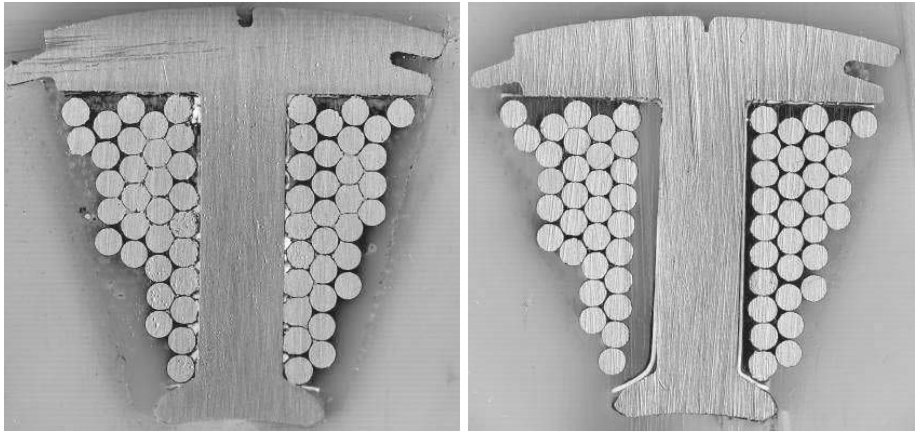


Fig. 3.12: Thermal results of simulation and measurements for T_1 , T_2 , T_3 and T_4

air cooling temperature for the different insulation material combinations. The values were obtained by simulation, since building a stator for every insulation combination was considered to be too expensive.

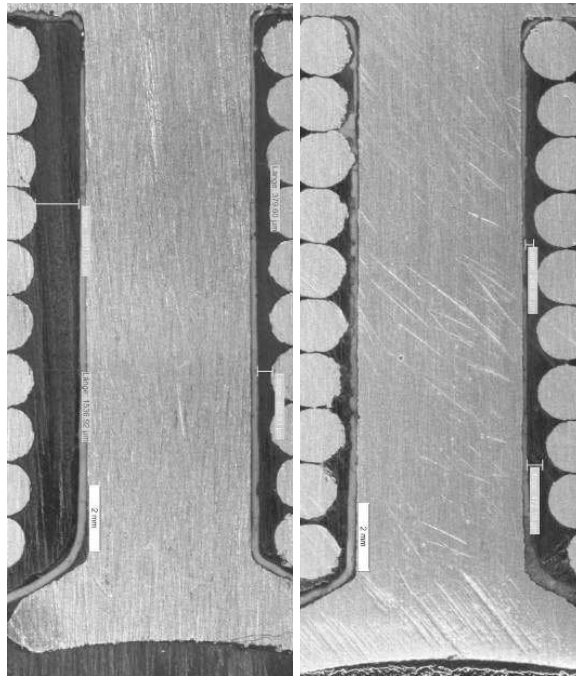
As shown in Tab. 3.3, by using simple insulation improvements the temperature can be decreased by 20 K. Potting, i.e. by the proposed epoxy, decreases the temperature by only 3 K (compare K.N.G2B.Y and K.E.G2.Y). The ceramic filled liner material showed very good mechanical strength during production, and can be recommended also for higher voltage classes. Using the liner without glass fiber basis, which has a 50 % higher thermal conductivity, led to insulation faults and should not be used especially when pressing the wires after winding. Improving the thermal path from the wire to the heat sink without using a potting material decreases production time thereby also reducing costs. Assuring that all gaps are filled with a thermal conductive epoxy is usually not easy to achieve in mass production often resulting in quality problems.



(a) K.E.G2.Y

(b) K.N.G2.N

Fig. 3.13: Polished cut images for pressed and non-pressed windings



(a) K.N.G2.N, 10 mm away

(b) K.N.G2.N, in the middle

Fig. 3.14: Measured polished cut image, at 10 mm away from the winding caps and in the middle

Tab. 3.3: Thermal results of simulation at nominal torque 10.4Nm (temperature measurement points shown in Fig. 3.11)

Code	T_1, T_2 Sim.	T_3 Sim.	T_4 Sim.
K.E.G2.Y	111 °C	99 °C	109 °C
K.N.G2B.Y	113 °C	99 °C	109 °C
N.E.G2.Y	116 °C	99 °C	109 °C
K.N.G2.Y	117 °C	99 °C	110 °C
N.N.G2B.Y	120 °C	99 °C	110 °C
N.N.G2.Y	133 °C	99 °C	111 °C

This can be explained by varying wire tolerances from batch to batch, and also winding window tolerances which decrease/increase the gaps between the wires for the epoxy to completely penetrate the winding up to the first layer.

As a result of the insulation improvements, the peak torque can be increased or machine size/length can be decreased. Tab. 3.4 shows the resulting temperatures for a peak torque of 13.1 Nm. The peak temperatures reach 166 °C for a standard Nomex[®], class 200 wire and no potting compared to 132 °C for the ceramic liner, and class 200 backing wire combination. In Tab. 3.3 and 3.4, it can be seen that the temperatures are well below the critical temperatures for the insulation material.

During development, it was not clear if the drive would also be used in harsh environments. The position of the ESS drives will be very close to the steering rod, which means that it will be very close to the ground. Mud and other dirt will choke the fins of the motor and power electronics and lead to a decreased heat transfer rate from the fins. Small dust particles are usually blown away during highway cruise, clay or other wet foulings might settle on the fins during heavy off road usage and dry out. Therefore, the drive was designed to be bigger than necessary. Right now the drive is designed so that even with 1 mm clay coated fins with a thermal conductivity of 0.25 W/mK [48] are still fully operational. Additionally, it was not clear if the air to cool the drive might even be hotter than 80 °C due to the proximity to the combustion engine.

Tab. 3.4: Thermal results of simulation at peak torque 13.1Nm (temperature measurement points shown in Fig. 3.11)

Code	T_1, T_2 Sim.	T_3 Sim.	T_4 Sim.
K.E.G2.Y	129 °C	109 °C	125 °C
K.N.G2B.Y	132 °C	109 °C	126 °C
N.E.G2.Y	137 °C	109 °C	126 °C
K.N.G2.Y	137 °C	109 °C	127 °C
N.N.G2B.Y	143 °C	109 °C	126 °C
N.N.G2.Y	166 °C	111 °C	130 °C

4 Rotor design for Magnetization

The following sections give an overview of where the magnetizing and demagnetizing curves originate and how they can be measured. Additionally, a detailed description is given on how to design a rotor for Post Assembly Magnetization in general, and how the magnets inside the rotor can be magnetized. A detailed overview on how the magnets are produced and how production will change the magnetic properties can be found in [101].

As introduced in the very beginning of this thesis, a method on how to measure the quality of permanent magnets during magnetization is presented in chapter 5.

4.1 Magnetizing and demagnetizing Mechanisms

Common modern REE permanent magnets are $\text{Nd}_x\text{Fe}_y\text{B}_z$, SmCo_5 and $\text{Sm}_2\text{Co}_{17}$ which show a nucleation or pinning magnetizing behavior. The process of magnetization can be seen in Fig. 4.1. If electrons are moving in free space they generate a magnetic field. In a magnet, electrons are moving around the atomic nucleus and generate strong dipole moments. The electrons rotate about themselves thereby generating spin-up or -down momentum. In absence of an applied field, these momentums are randomly distributed. Applying an external magnetic field leads to partially reversible movement of the so called Weiss domains. Increasing the field leads to a sudden irreversible movement of the walls described best by the Barkhausen effect. If the field rises even further, the whole magnet changes its magnetization direction and the magnet becomes fully magnetized. In this state a certain negative field, the coercive field strength H_{cJ} , has to be applied to repeal the magnetization [117].

4.1.1 Pinning Mechanism

Magnets which show pinning magnetization mechanism consist of very rigid domain walls which can only be changed when applying a very strong field. Therefore, the coercive field strength rises faster than the remnant flux density B_r [34]. Applying this very high field results in rotation of the walls at ones. An example of a material in which the magnetization occurs according to the pinning mechanism is $\text{Sm}_2\text{Co}_{17}$.

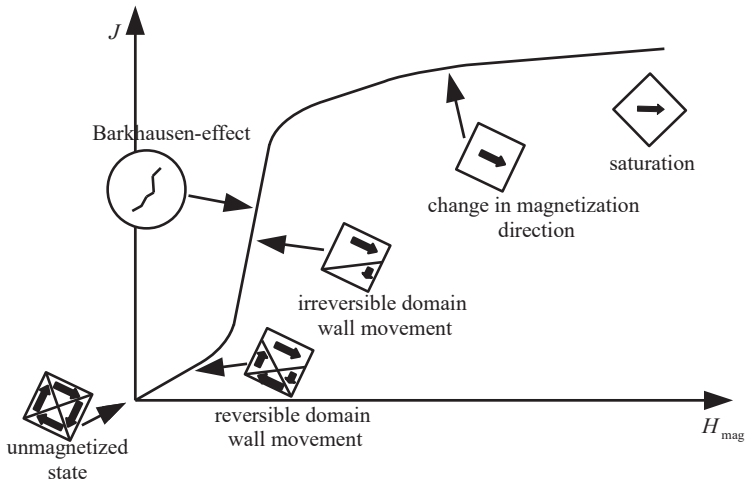


Fig. 4.1: Magnetization process [117]

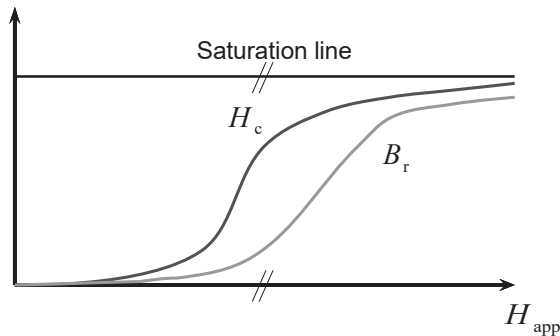


Fig. 4.2: Pinning mechanism at magnetization [34]

4.1.2 Nucleation Mechanism

In an unmagnetized magnet, the domains have magnetic moments which are randomly oriented [34]. In NdFeB and Sm_1Co_5 , which show a nucleation mechanism, these domains contain walls which are easy to move compared to the pinning mechanism. Heating the magnets over the Curie point and cooling them down field free leads to the generation of smaller domain regions, which are easier to remagnetize. The starting point of the magnetization is the so called nucleation point, which is a favorable discontinuity. Around this point, the domain walls of the adjacent wall move into the favorable direction and allow a single directed remnant flux density. Compared to the pinning mechanism, the remnant flux density rises faster than the coercive field strength (compare Fig. 4.3 and 4.2), but to fully magnetize the magnet, a high magnetic field is needed to eliminate any unfavorable discontinuities which might be the starting point of demagnetization [141].

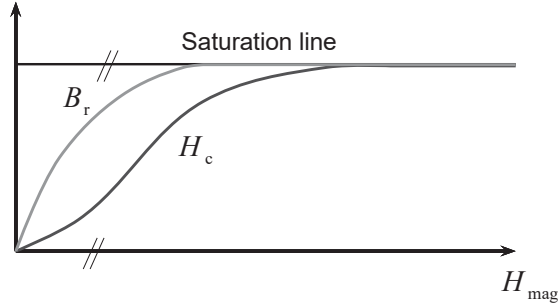


Fig. 4.3: Nucleation mechanism at magnetization [34]

4.1.3 Magnetization Fields

To fully magnetize the magnets, a field strength big enough to fully redirect the domain walls has to be applied. Depending on the material, the field strength varies quite a bit. [202] gives the following minimum intrinsic field strength $H_{\text{mag,min}}$ for REE magnets during magnetization:

Tab. 4.1: Minimum magnetizing field strength $H_{\text{mag,min}}$ for different magnet materials [202]

Material	$H_{\text{mag,min}}$
NdFeB	2,500 kA/m
Sm ₁ Co ₅	2,000 kA/m
Sm ₂ Co ₁₇	3,650 kA/m

Unfortunately, there are no more detailed values given for different compositions of NdFeB, Sm₁Co₅ or Sm₂Co₁₇, which vary due to their different B_r and H_{cJ} as seen in Fig. 4.2 and 4.3.

4.2 NdFeB Magnet Ingredients and their Impact

As mentioned in section 2 the motor was built using a 255/200 NdFeB magnet material. NdFeB magnets are made of a Nd₂Fe₁₄B matrix which is usually encapsulated in a Neodymium grain boundary phase. This boundary phase can contain smaller amounts of Praseodymium, Gadolinium, Terbium and Dysprosium [8]. Other elements like Cobalt, Titanium, Vanadium and others are sometimes added to increase corrosion resistance. Tab. 4.2 shows the most important weight percentage of ingredients of different materials, as well as their B_r , H_{cJ} and the maximum operational temperature. As can be seen, the Dysprosium content is responsible for a larger H_{cJ} as well as a larger operational temperature but reduces B_r because of its ferrimagnetic characteristic. In the 335/127 material, Dysprosium is replaced by Terbium which gives a decent amount of H_{cJ} compared to its weight percentage of 0.2%, and hence does not influence B_r

that much. Unfortunately, the maximum operational temperature of 120 °C is too low for use in automotive systems (see section 2.1). Since Tb is even rarer than Dy, it is not a good replacement [29].

Tab. 4.2: Weight percent of important ingredients, remnant flux density B_r , the intrinsic coercive field strength $H_{c,J}$ and the max. reasonable operable temperature of selected materials [143, 202]

Material	Sm	Dy	Tb	Nd	Co	$B_{r,min}$	$H_{c,J,min}$	max. Temp
335/127	0.0%	0.0%	0.2%	31.1%	2.0%	1.33 T	1,273 kA/m	120 °C
335/127.5	0.0%	2.8%	0.3%	28.6%	1.0%	1.33 T	1,275 kA/m	110 °C
255/200	0.0%	7.5%	0.0%	25.0%	2.9%	1.17 T	2,000 kA/m	170 °C
225/262.5	0.0%	10.7%	0.0%	22.2%	2.9%	1.09 T	2,625 kA/m	220 °C
250/263	0.0%	9.8%	0.0%	22.5%	1.0%	1.15 T	2,625 kA/m	220 °C
190/159	25.0%	0.0%	0.0%	0.0%	52.0%	1.10 T	1,590 kA/m	350 °C

255/200 material which was used for the designed motor gives a reasonable amount of coercive field strength and a good energy product of 255 kJ/m³ compared to its maximum reasonable operational temperature of 170 °C. Still, the Dy content of 7.5 % is very high. The following Tab. 4.3 lists the proportional as well as the total raw material costs per kg of these magnet materials. The table only includes the major price components. Fe is considered to be inexpensive.

Tab. 4.3: Proportional and total cost in Euro for one kg of selected raw material, domestic China prices on 28th of February 2015 (see Fig. 1.2)

Material	Sm	Dy	Tb	Nd	Co	Total
335/127	0€	0€	1.2€	17.8€	0.6€	19.7€
335/127.5	0€	10.2€	2.3€	16.4€	0.3€	29.2€
255/200	0€	27.2€	0€	14.3€	0.9€	42.4 €
225/262.5	0€	38.7€	0€	12.7€	0.9€	52.4€
250/263	0€	35.5€	0€	12.9€	0.3€	48.7€
190/159	3.5€	0€	0€	0€	16.7€	20.1€

Looking at the used 255/200 material, Dy makes up for 63 % of the raw material costs. In Fig. 4.4 and 4.5, the relative costs of a 255/200 magnet are shown for July 2011 and February 2015 when ordering 3.6 mio. magnets a year for the ESS. It is interesting to notice that at more or less constant manufacturing costs, the relative costs for Dy have been cut in half in the last 3.5 years.

To cushion production against sudden price shocks it is very useful to reduce the amount of HREE. In order to get a very high temperature resistant rotor it might be good to increase the magnet thickness and use a Sm₂Co₁₇ magnet material, e.g. a 190/159 magnet, instead of a high temperature NdFeB magnet with high Dy content. Since the price for Sm and Co have been rather low recently, it is expected that this material might become again more popular in the future. New materials like TOSREX[®] [200] are looking promising.

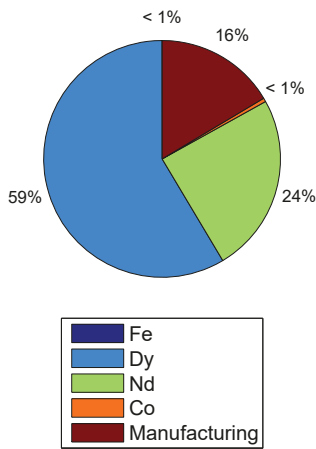


Fig. 4.4: 255/200 magnet, relative cost in July 2011

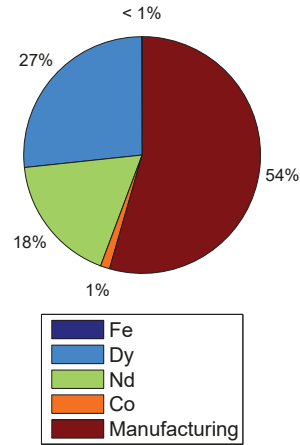


Fig. 4.5: 255/200 magnet, relative cost in February 2015

4.3 Demagnetizing Curves

After being fully magnetized, the magnets operate along the so called demagnetizing curve, which depends on temperature, the magnetization field strength and the demagnetizing field. In Fig. 4.6, the dependence of the temperature on the flux density as well as the polarization curve are shown for the 255/200 magnet. The slope of the polarization curve, the susceptibility χ_{mag} , varies with respect to temperature and field intensity.

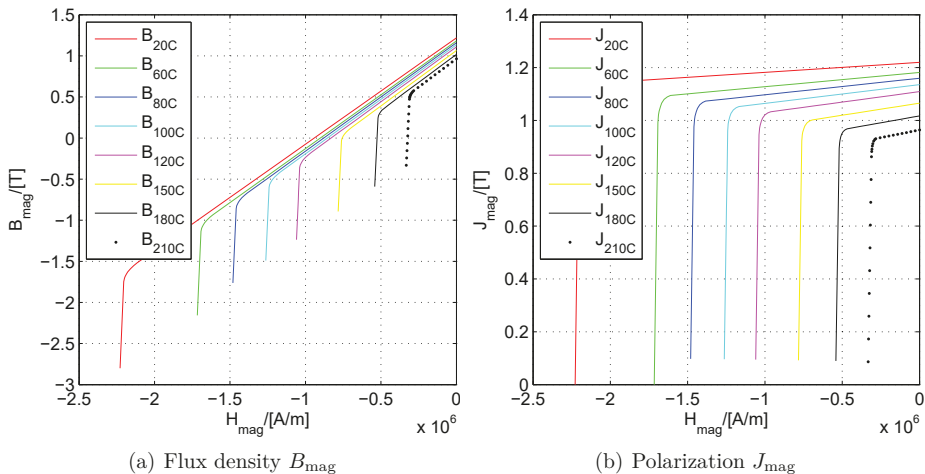


Fig. 4.6: Demagnetizing curves of 255/200 material, flux density B_{mag} and polarization J_{mag} at different temperatures [202]

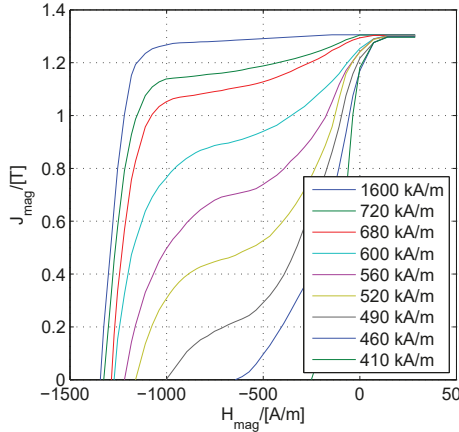


Fig. 4.7: Polrization curve J_{mag} of a 362/140 magnet vs. max. magnetization field strength [202]

In Fig. 4.7 the demagnetization curves for a 362/140 magnet material are shown with respect to its magnetizing field strength. The difference between a fully saturated and a 90% saturated magnet in terms of maximum magnetizing field strength is big. Therefore, it is very important to fully saturate all regions of the magnet in order to avoid any non-magnetized nucleation points, which might be the starting point of irreversible demagnetization.

4.4 High Field generation for the magnetizing Process

There is a variety of magnetizing procedures depending on the magnet material. Low coercive ferrites can be magnetized via stronger REE magnets [34], or by the stator coils in a fully assembled motor [57]. REE magnets are more difficult to magnetize without special fixtures. The authors of [56] try to magnetize NdFeB magnets by the stator coils with several subsequent pulses. Due to the enormous current needed for magnetization, the stator coils heat up, so that some time has to elapse before applying the second pulse. Magnetizing the rotor inside the assembled motor has the advantage that the magnetized rotor does not have to be inserted into the stator, which is difficult since the rotor sticks to the inner stator.

Paper [34] analyzed a magnetizing fixture composed by a RLC resonant circuit with a free-wheeling path. A capacitor which is charged to a high voltage and discharged quickly over the magnetizing coils generates a high current, resulting in a high field which will trigger the domain wall movement of the magnets. The circuit is shown in Fig. 4.8. Diodes parallel to the load insure, that the emerging RLC resonant circuit will not produce reversed currents which will generate a demagnetizing field. Such a pulse current can be differentiated into the first half oscillation and the tailing neglecting the parasitic capacitances $C_{\sigma, \text{OnOff}}$, $C_{\sigma, \text{free}}$, $C_{\sigma, \text{sw}}$, $C_{\sigma, \text{free, sw}}$, $C_{\sigma, \text{load}}$ as well as the switch parasitics [25]:

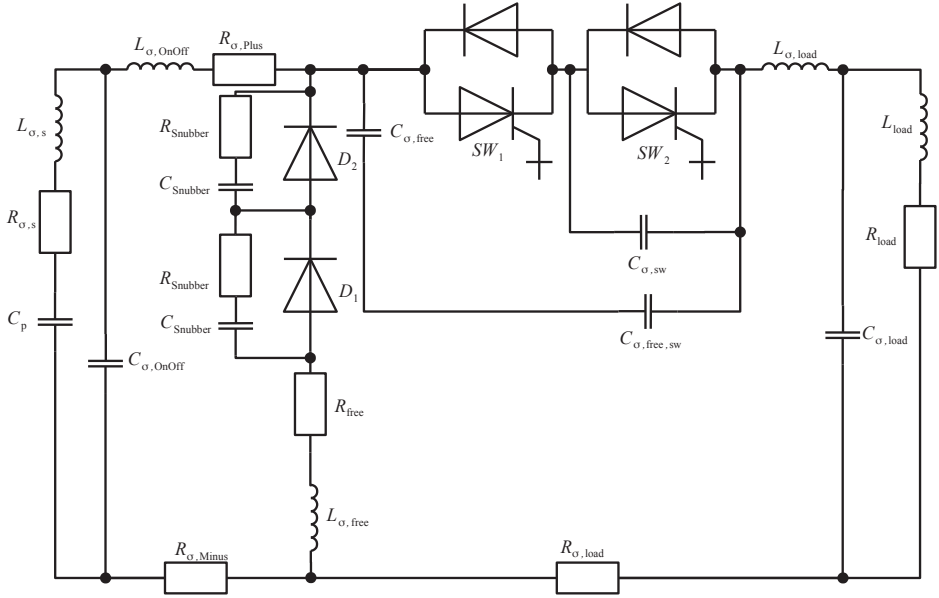


Fig. 4.8: Equivalent circuit of the magnetizer including parasitic influences

$$C = C_p \quad (4.1)$$

$$L = L_{\sigma,s} + L_{\sigma,OnOff} + L_{\sigma,load} + L_{load} \quad (4.2)$$

$$R = R_{\sigma,s} + R_{\sigma,Plus} + R_{load} + R_{\sigma,Load} + R_{\sigma,Minus} \quad (4.3)$$

$$\omega = \sqrt{\frac{1}{LC} - \frac{R^2}{4L^2}} \quad (4.4)$$

$$i_{\text{rising,oscillation}}(t) = \frac{U_0}{L\omega} \cdot e^{-\frac{R}{2L}t} \cdot \sin(\omega t) \quad (4.5)$$

As can be seen in formula 4.5, to achieve high currents quickly, the inductance and the capacitance should be as low as possible. Hence, it is very useful to achieve the needed energy inside the capacitor $E_c = \frac{1}{2}C_p U_0^2$ by increasing the voltage rather than by increasing the capacity.

In terms of magnetization, the tailing is not necessary and produces losses inside the magnetizing coils. For this reason, it should be kept as short as possible (see Fig. 4.9). To decrease the joule heating caused by the tailing, a resistance R_{free} can be inserted into the free wheeling path (see Fig. 4.8). This resistance will cause the current to flow back into the capacitor after the first half oscillation, and unload over the free wheeling resistance. Dissipating less power into the magnetizing coils improves the cycle time, which is important in terms of mass production.

The resistance R_{free} can also be used to generate a negative half oscillation. Being able to continuously change the resistance R_{free} enables the control of the amplitude of the negative half oscillation independent of the first positive one (see Fig. 4.9).

U_0	:=	Charging voltage of the capacitor
C_p	:=	Capacitance of magnetizer capacitor
$L_{\sigma,s}$:=	Capacitor leakage inductance
$L_{\sigma,OnOff}$:=	On/off leakage inductance
$L_{\sigma,load}$:=	Load leakage inductance
L_{load}	:=	Load inductance
$L_{\sigma,free}$:=	Free wheeling inductance
$R_{\sigma,s}$:=	Capacitor inner resistance
$R_{\sigma,Plus}$:=	Positive connector resistance
R_{load}	:=	Load resistance
$R_{\sigma,load}$:=	Load connector resistance
$R_{\sigma,Minus}$:=	Minus connector resistance
R_{free}	:=	Free wheeling resistance
$C_{\sigma,OnOff}$:=	On Off leakage capacitance
$C_{\sigma,free}$:=	Leakage capacitance of free wheeling branch
$C_{\sigma,sw}$:=	Switch leakage inductance
$C_{\sigma,free,sw}$:=	Leakage capacitance between free wheeling branch and switches
$C_{\sigma,load}$:=	Load leakage inductance

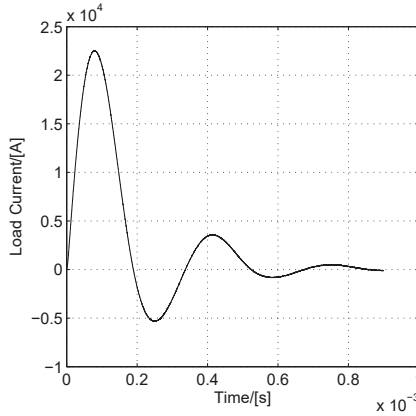


Fig. 4.9: Testing example current for magnet quality measurement measured on the lab test bench

4.4.1 Specifications of the magnetizing Circuit

The development of the magnetizing circuit consumed a big portion of the whole time and monetary budget of this research. From the scope of this work, it has to be ranked as a tool with some specialties. Therefore, only a brief overview of the development is given.

The magnetizer and Quality Control Magnetizer (Quality Control Magnetizer (QCM)) has to fulfill the following specifications:

- A maximum of 2,500 kA/m has to be achieved inside the entire magnet to fully saturate the 255/200 magnets (see Tab. 4.1)
- The maximum heating of the magnetizing coils is limited to 40 K per cycle, to limit the cycled thermal expansion
- The maximum voltage is limited by the insulation of the enameled winding wire (5,000 V) [188] (including double safety factor)
- The time between each magnetization is limited to 15 min
- Life expectancy of the magnetizing coil is 1,000 magnetizations
- The magnetizing coils should be placed right next to the main circuit, reducing the stray inductances resulting from long connecting cables
- The analysis electronics should be placed into an additional box next to the fixture
- The control FPGA board should be placed into an extra box inside the main cabinet because of EMI reasons
- All metallic parts will be grounded
- Safety reasons:

a double safety concept should be installed - having the magnetizing coils in an extra cabinet inside the main cabinet

an interlock system including all doors, charging supply unit, control electronics should be installed

the capacitor is discharged over an extra resistor in case the interlock is opened

control of the whole circuit should be done from a computer

all connections to the computer should be galvanically isolated

a Failure Mode and Effect Analysis (FMEA) should be conducted

Resulting specifications:

- Max. 31 kA
- Max. 7 kJ
- High $\frac{di}{dt}$
- Controllable negative amplitude independent of the positive one

4.4.2 Brief Design Description

The design is only mentioned briefly in this section. A very detailed description can be found in [25, 136]. The circuit shown in Fig. 4.8 is composed of the following hardware components:

- Capacitor (C_p) Electronicon E.59.A18-694010 [160]

capacity: $689 \mu\text{F}$

rated DC Voltage: $6,500 \text{ V}$

I^2t : $4.4 \times 10^5 \text{ A}^2\text{s}$

- AZ-Switches ($SW_{1,2}$) [25] with inverse diode

repetitive DC blocking voltage per switch: $2,800 \text{ V}$

I^2t : $5 \times 10^5 \text{ A}^2\text{s}$

max. $\frac{di}{dt}$: $20 \text{ kA}/\mu\text{s}$

required stack pressing force: 50 kN

- Diodes ($D_{1,2}$) ABB 5SDD 38H5000 [144]

repetitive DC blocking voltage per diode: $2,800 \text{ V}$

I^2t : $10.1 \times 10^6 \text{ A}^2\text{s}$

required stack pressing force: $45 \text{ kN}-55 \text{ kN}$

- Variable power resistor (R_{free}) (in house made) [139]

resistance: $0.1 \Omega-0.35 \Omega$

I^2t : $20 \times 10^6 \text{ A}^2\text{s}$

max. allowable pressing force: 60 kN

The design also consists of the usual high voltage, high current design protection systems, like snubbers, discharge resistance etc. The FMEA can be found in [136]. The magnetizing setup can be seen in Fig. 4.10.

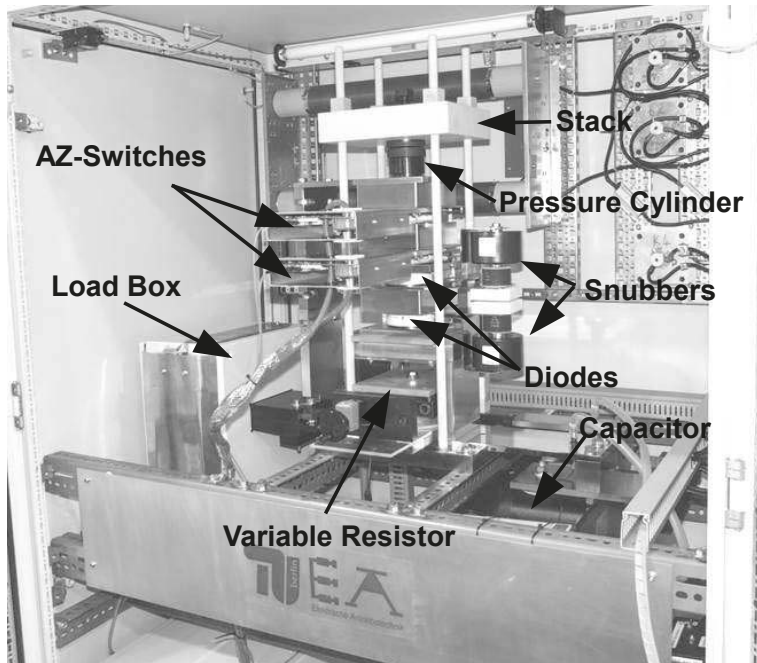


Fig. 4.10: Lab magnetizing circuit [25]

4.5 Rotor Design for Magnetization

Since the rotor geometry is influencing the magnetic fixture design and vice versa, it is important to take a close look at the rotor geometry, which was optimized for magnetization and quality control.

Usually the rotor is designed with respect to the stator, and in the end, the magnetizing coils are placed around it, resulting in several difficulties. This approach considers the magnetization during the rotor stator design process. Design parameters for a PAM rotor and its magnetizing fixture are:

- Full saturation of the magnets as introduced in section 4.1.3
- Penetration angle of the field
- Skewing of the magnet segments
- Mechanical strength of the magnetizing coil core material
- Good thermal path for the magnetizing coils
- Windability
- Fixation technique
- Design for Quality Control Magnetizer (QCM)

In the following sections, these aspects will be discussed in detail. The resulting magnetizing fixture, which generates the field, will be presented in chapter 5.

4.5.1 Magnetic Saturation during Magnetization

During magnetization it is very important that all parts of the magnets are fully saturated. Apart from not reaching the wanted output flux, non-complete saturation will result in magnetic impurities which will be the starting point of unwanted demagnetization of the whole magnet. Depending on how deep the magnets are buried, it is difficult to achieve full saturation. Rotor designs with very big L_q/L_d , where the magnets are buried very deep [102, 130] into the rotor suffer from fully reaching the necessary saturational field strength (see Tab. 4.1). Rotors with more than one magnet barrier per pole (see Fig. 4.11) for leakage flux reduction do not improve the saturation problem.

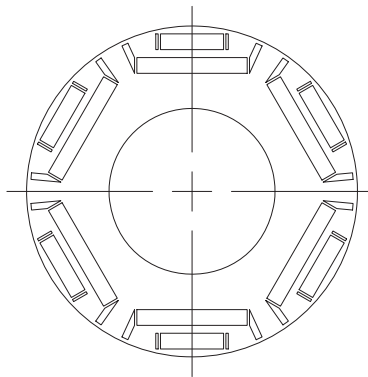


Fig. 4.11: Multi bar rotor topology

Magnetizing coils are usually wound around an electric steel lamination stack. Other than the stator windings which are wound automatically, winding for the magnetizing fixture is achieved by sticking the wire into holes, and winding them by hand similar to a needle thread technique. This allows higher mechanical strength and accurate positioning. The minimal distance between the inner diameter of the fixture and the wires was found to be 0.2 mm, and confirmed by several magnetizing companies. This is necessary because of the forces generated during manual winding. The clearance of the rotor inside the bore hole is 0.2 mm on each side, to account for lamination tolerances. These distances again limit the field strength through the rotor.

In a study [141] conducted at the TU-Berlin, several topologies were investigated. When purely looking at the saturation of the magnet, coils placed inside and outside of the rotor give the best results. Due to the radial placement of the coils and the alternating currents from pole to pole, the coils create a major force in the positive radial direction. For outside coils this is not a problem since the magnetic fixture is situated radially outside of the coils. For coils inside the rotor, the thin bridges in

between have to hold the coils during magnetization. This again limits the magnetizing field and hence the saturation.

4.5.2 Penetration Angle and Strength of the Field

When using just outer rotor coils, it is important to consider the penetration angle of the field when using anisotropic magnetic material. As already mentioned in section 2.4.2, flux concentrating rotors (see Fig. 2.12(c)) give the best results when using outer coils because the field is parallel to the easy axis of the magnet. After talks with several magnetization companies, it can be stated that to achieve maximum utilization of the magnet material, the angle between easy axis and field vector should be smaller than 35 degree.

4.5.3 Skewing of the Rotor

Segment skewing of the rotor is usually done because of the lower costs when compared to stator tooth skewing. Modern hybrid motors have a so called V-skewing. V-skewing means that the rotor is skewed in such a way that its segments form a V by skewing in one direction up to the middle and then back (see Fig. 4.12). This reduces acoustic noise [9]. V-skewing is very challenging for the magnetic fixture since the winding wires have also to be wound in V-direction, but through the magnetic fixture stack. For magnetic fixtures very thick wires 2 mm-4 mm are used, because of the big thermal capacitance of copper. From experience with winding of magnetizing fixtures in V-form, the skewing angle is limited to 5 degree mechanically.



Fig. 4.12: V-Skewing

4.5.4 Thermal Path for the Heat generated during Magnetization

The biggest portion of the energy needed to achieve high saturation fields is converted into heat inside the coils. Only a very small portion is necessary to align the dipoles

with the field. To achieve high throughput, it is necessary to have a very good thermal path to the heat sink. Talks with magnetizing companies it is advisable to keep the temperature increase for one current pulse in mass production below 40 K, to prevent cyclic mechanical stress between epoxy and copper wire. The epoxy has to fully penetrate all gaps to prevent any movement of the wires. Movement triggers insulation wear and results in electrical insulation faults.

4.5.5 Fixation Technique

Very important is the fixation of the rotor since it might be subject to large forces. These can move the rotor into the almost-zero field region and result in a very low magnetization. A pin as introduced in [102] can be used to fix the rotor in the magnetization fixture.

4.5.6 Rotor design for the Quality Control Magnetizer

As it will be shown in the next chapter, the quality of each magnet can be measured during magnetization. Since the method cannot differentiate between lamination and magnet, it is very important that equal steel qualities are used during production. This is not only limited due to the raw material, but also due to the cutting techniques [50]. Different laser types or wear of the cutting tool can change the behavior of the laminations, so that it becomes difficult to differentiate between possible magnetic tolerances of steel or magnets. To detect the field of the magnet and distinguish between quality difference and mechanical tolerance of magnet and lamination, it is important to fix the magnets precisely, as well as the rotor (see section 5.2.13).

5 The Quality Control Magnetizer

Usually, when a rotor is supposed to be tested for correct magnetization after being magnetized, the total flux is measured. During removal of the rotor out of the magnetic fixture, a coil at the entrance of the fixture bore sums up the flux over the entire surface [131]. This method is neither very sensitive, nor does it test for the correct demagnetization curve under magnetic stress. [82] measures the EMF of the rotating rotor inside the proper stator. Additionally, currents are applied to test the magnets under magnetic stress. For this test, bearings and the bearing shields have to be mounted - which takes additional time. Using the corresponding stator for this test can also be done, but it cannot be differentiated between a broken stator or rotor. Several authors measured the resultant field of the magnetized rotor with Hall sensor arrays, or a single movable Hall sensor [13, 87, 115]. By rotating the rotor a two dimensional field map can be generated. A similar study was conducted at the TU-Berlin [140], measuring the rotor field components after magnetization with three Hall sensors in all dimensions. Advancements in Hall sensor packaging led to a magnetic field camera which is also able to monitor the field vector [120]. These methods do not give any profound answers about the behavior of the magnets under magnetic stress. Additionally, these methods require an extra manufacturing station. In this section, a new method to measure IPM rotors, the Quality Control Magnetizer (QCM), is introduced. The QCM is able to measure part of the hysteresis curve of each magnet during the magnetization procedure without the need of an extra station or additional time.

The QCM is a combination of a normal pulse magnetizer with a resistance R_{free} in the free wheeling circuit as introduced in section 4.4, and a so called Pulsed Field Magnetometer (PFM). To understand how the QCM works, a firm understanding of the PFM is indispensable. The following section explains the PFM in detail, and presents the changes needed to built the QCM. The QCM is built up and several tests are performed.

5.1 Pulsed Field Magnetometer

The first industrial PFM was developed by Hirst[®] and the University of Plymouth in the early 2000s [20]. It was developed to characterize high coercive magnets in a high volume production line. Methods like the Vibrating Sample Magnetometer, which uses the super conductivity at 4K of the coils to generate high DC fields [20], are unsuitable in a high volume production environment, because of the low temperature. Other methods like high temperature superconductors for only the magnetizing coils like Nb₃Sn are investigated by [108] but are not market ready.

The PFM is currently used to characterize single magnets for their hysteresis loop, thereby also characterizing specific parameters like remnant flux density B_r and coercive field strength H_{cJ} [42, 164]. To understand the concept of the PFM, a magnetizing field investigation has to be conducted.

5.1.1 Pulsed Field Magnetometer Field Analysis

If magnetic material is subject to an external field, the magnetic working point inside is changing. The magnetic field can be separated into the following parts [164]:

$$\vec{H}_{\text{mag}} = \vec{H}_{\text{app}} - \vec{H}_{\text{eddy}} - \vec{H}_{\text{demag}} \quad (5.1)$$

$$\begin{aligned} \vec{H}_{\text{mag}} &:= \text{Magnetic field strength inside the magnet} \\ \vec{H}_{\text{app}} &:= \text{Applied magnetic field strength} \\ \vec{H}_{\text{eddy}} &:= \text{Resulting eddy field strength} \\ \vec{H}_{\text{demag}} &:= \text{Demagnetizing field strength} \\ \vec{M}_{\text{mag}} &:= \text{Magnetization of the magnet} \end{aligned}$$

In a pure DC field, the eddy current content reduces to zero. Analyzing the flux density inside the magnet leads to the following well known formula:

$$\vec{B}_{\text{mag}} = \mu_0 \cdot [\vec{H}_{\text{mag}} + \vec{M}_{\text{mag}}] \quad (5.2)$$

Inserting formula 5.1 into 5.2 for the DC-case leads to:

$$\vec{B}_{\text{mag}} = \mu_0 \cdot [\vec{H}_{\text{app}} - \vec{H}_{\text{demag}} + \vec{M}_{\text{mag}}] \quad (5.3)$$

Looking at Fig. 5.1, the particular field components can be seen separately. The demagnetizing field is the component which is responsible for setting the working point of the magnet. It is dependent on the geometry and not on the applied field. Therefore, formula 5.3 can be expressed in a different form by introducing the demagnetizing tensor \tilde{N}_d [90, 128]:

$$\vec{B}_{\text{mag}} = \mu_0 \cdot [\vec{H}_{\text{app}} - \tilde{N}_d \cdot \vec{M}_{\text{mag}} + \vec{M}_{\text{mag}}] \quad (5.4)$$

The demagnetizing tensor simplifies formula 5.3 and allows formula 5.4 to be solved for the magnetization \vec{M}_{mag} . When analyzing a strict homogeneous field, formula 5.4 can be simplified using the demagnetizing factor N_d :

$$B_{\text{mag}} = \mu_0 \cdot [H_{\text{app}} + (1 - N_d) \cdot M_{\text{mag}}] \quad (5.5)$$

When analyzing the demagnetizing field using this factor, one has to differentiate between the so called magnetometric $N_{d,m}$ and the fluxmetric $N_{f,m}$ demagnetizing factor. $N_{d,m}$ is the average demagnetizing factor over the whole specimen and a good approach for small samples [17]. $N_{f,m}$ is the demagnetizing factor over the mid plane of the specimen. All analytically calculated values are only valid if the specimen has uniform susceptibility χ_{mag} , which will be discussed in the next sections - where N_d will refer to $N_{d,m}$.

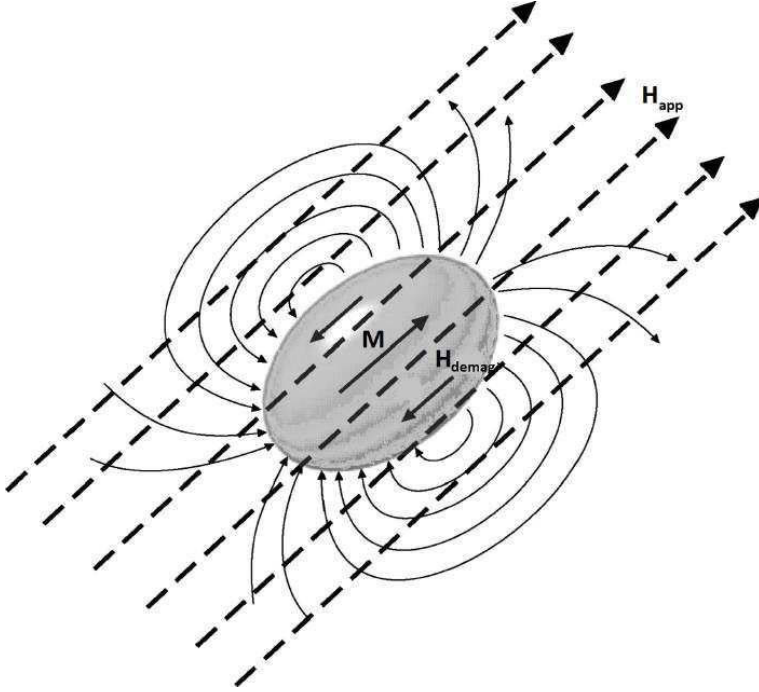


Fig. 5.1: Fields components inside magnetic material [140]

5.1.2 Pulsed Field Magnetometer Setup

The PFM uses this simplification by introducing the following basic setup shown in Fig. 5.2 for a strict homogeneous field. A cylindrical magnetic probe is situated within a search coil (B_{mag}). The field coil produces the magnetic field which drives the magnet around its hysteresis loop. The B_{app} coil measures the applied field far enough from the probe, to render its influence negligible. When inserting formula 5.6

$$B_{\text{app}} = \mu_0 \cdot H_{\text{app}} \quad (5.6)$$

$$J_{\text{mag}} = \mu_0 \cdot M_{\text{mag}} \quad (5.7)$$

into 5.5, the magnetization M_{mag} can be calculated:

$$M_{\text{mag}} = \frac{B_{\text{mag}} - B_{\text{app}}}{\mu_0 \cdot (1 - N_d)} \quad (5.8)$$

Plotting M_{mag} is usually done with respect to the intrinsic field strength H_{mag} . The following formula specifies the intrinsic field inside the magnet [32] - depending on the applied field H_{app} :

$$H_{\text{mag}} = H_{\text{app}} - N_d \cdot M_{\text{mag}} \quad (5.9)$$

These formulas are only valid if the coils are directly wound around the probe. To be able to change the probe easily - the coils are wound around a coil bobbin - which

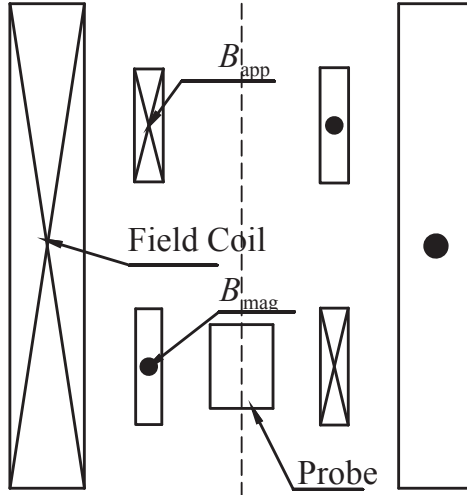


Fig. 5.2: Schematic cross section of a cylindrical PFM. B_{app} and B_{mag} are measured by integration over the induced voltage of the search coils [28]

increases the distance from probe to coil. In this case, B_{mag} which is usually calculated by integrating the induced voltage inside the coil, has to be multiplied by an effective field area fitting factor $X_{\text{A,fit}}$ [164]:

$$B_{\text{mag}}(t) = X_{\text{A,fit}} \int \frac{U_{\text{mag}}(t)}{N \cdot A_{\text{field}}} dt \quad (5.10)$$

- $U_{\text{mag}}(t)$:= Induced voltage inside B_{mag} search coil
- A_{field} := Field area
- $X_{\text{A,fit}}$:= Effective field area fitting factor

This linear consideration is only valid if ferromagnetic materials like a rotor are absent. In case of their presence, the effective field fitting factor becomes a function of their saturation. With the PFM, it is now possible to analyze cylindrical specimens with respect to their magnetization. These easy formulas 5.8, 5.9 do not include:

- Eddy current effects
- Magnetic viscosity
- Non-homogeneous fields
- Demagnetization tensor \tilde{N}_{d} - depending on susceptibility χ_{mag}
- Temperature dependence of the demagnetizing curves

These items complicate the determination of the magnetic specifications, and are therefore discussed in detail in the following sections. To be able to investigate these effects, a small cylindrical PFM similar to [18, 20, 45, 67, 96, 106, 164] was build up in our lab.

5.1.3 Eddy current Effects

As mentioned in the paragraphs before, a PFM uses pulsed fields instead of stationary fields to drive the specimen around its hysteresis loop. As a result, eddy currents are induced inside conductive specimens according to Maxwells law. Simply measuring the magnetization M_{mag} as stated in formula 5.8 without considering fields weakening effects caused by eddy effects leads to unrealistic hysteresis curves, usually recognizable by additional loops (see Fig. 5.3). It can be seen that they add a $\frac{\partial B}{\partial t}$ dependent component also known as dynamic magnetization M_{eddy} .

$$M_{\text{eddy}} \propto -\kappa_{\text{mag}} \frac{dB_{\text{mag}}}{dt} \quad (5.11)$$

Therefore, formulas 5.8 and 5.9 have to be rewritten:

$$\begin{aligned} M_{\text{eddy}} &:= \text{Dynamic magnetization due to eddy effects} \\ \kappa_{\text{mag}} &:= \text{Electric conductivity of specimen} \end{aligned}$$

$$M_{\text{mag}} = \frac{B_{\text{mag}} - B_{\text{app}} - \mu_0 M_{\text{eddy}}}{\mu_0 \cdot (1 - N_{\text{d}})} \quad (5.12)$$

$$H_{\text{mag}} = H_{\text{app}} - N_{\text{d}} \cdot M_{\text{mag}} - M_{\text{eddy}} \quad (5.13)$$

Several authors have dealt with the problem of eddy effects inside a PFM [27, 40, 44, 66] and proposed several solutions. [27] proposed and tested a so called $f/2f$ method, where the specimen is tested twice, once with a pulse with a frequency f , and once with a frequency of $2f$. Since they will cause different amounts of dynamic magnetization, formula 5.12 can now be corrected without knowing the conductivity. Changing the frequency is usually done by changing the capacitor, or by using an additional coil [164]. For this reason, another high current switch is needed, which makes the entire apparatus expensive.

[32] proposed a simple formula derived from the Biot-Savart formula for a uniform $\frac{dB_{\text{mag}}}{dt}$ over the whole cylindrical specimen. This can be done in case the skin effect depth $\delta_{\mu,r}$ [54] is large enough:

$$\delta_{\mu,r} = \sqrt{\frac{2}{\pi \kappa_{\text{mag}} f \mu_0 \mu_{\text{mag}}(H_{\text{mag}})}} \quad (5.14)$$

Since the permeability of the specimen $\mu_{\text{mag}}(H_{\text{mag}})$ might depend on the intrinsic

$$\begin{aligned} \delta_{\mu,r} &:= \text{Skin effect depth} \\ f &:= \text{Frequency} \end{aligned}$$

field, the biggest differential permeability has to be considered. Assuming a complete

penetration of the specimen, the following formula can be determined for the dynamic magnetization [32]:

$$M_{\text{eddy,cyl}}(t) = -\kappa_{\text{mag}} \frac{dB_{\text{mag}}(t)}{dt} \int_0^{R_{\text{cyl}}} \underbrace{\frac{(R_{\text{cyl}}^2 - r^2)r}{R_{\text{cyl}}^2 \left(\sqrt{1 + (2R_{\text{cyl}}/h_{\text{cyl}})^2} + \sqrt{1 + (2r/h_{\text{cyl}})^2} \right)}}_{c_1} dr \quad (5.15)$$

In Tab. 5.1 the electrical conductivities of several magnet types and their tolerances

$$\begin{aligned} R_{\text{cyl}} &:= \text{Radius of the cylindric specimen} \\ h_{\text{cyl}} &:= \text{Height of the cylindric specimen} \\ c_1 &:= \text{Geometry factor} \end{aligned}$$

in mass production are given. Since the conductivities might vary from sample to sample, the simple formula 5.15 cannot be applied since an insufficiently magnetic magnet, which lies outside the magnetic tolerances, might be evaluated as good because of the tolerated electric conductivity. Another obstacle is the anisotropic resistance

Tab. 5.1: Electric resistance of hard magnetic material [191, 192, 202]; || : parallel to the easy axis, \perp : perpendicular to the easy axis direction

Magnet material	Specific elec. resistance [Ωm]
NdFeB	$1.4 \cdot 10^{-6} - 1.6 \cdot 10^{-6} ; 1.2 \cdot 10^{-6} - 1.4 \cdot 10^{-6} \perp$
Sm ₂ Co ₅	$0.4 \cdot 10^{-6} - 0.7 \cdot 10^{-6}$
Sm ₂ Co ₁₇	$0.65 \cdot 10^{-6} - 0.95 \cdot 10^{-6}$
Ba ₁ Fe ₁₂ O ₁₉	$> 10^4$
Sr ₁ Fe ₁₂ O ₁₉	$> 10^4$

inside NdFeB magnets, which limits the use of formula 5.15. Therefore, only strict homogeneous fields should be investigated.

In Fig. 5.3, one can see the hysteresis curve of a commercially available NdFeB magnet [148] tested in our lab with the apparatus introduced in Fig. 5.2. At a magnetic field strength H_{mag} of 2,450 kA/m, the magnet is over-saturated, which can be seen in the north-eastern corner of this figure. In case of full saturation, the magnetization M_{mag} does not change anymore, so the plot is only dependent on H_{app} and its frequency. Depending on the frequency and magnitude of H_{app} , induced eddy currents inside the magnet lead to the typical bullet looking B-H-Curve. Near the maximum $H_{\text{app,max}}$, $J_{\text{mag}} = \mu_0 M_{\text{mag}}$ should be linear. One can state now that:

$$J_{\text{mag},1}(H_x) = J_{\text{mag},2}(H_x) \quad (5.16)$$

$$H_{\text{app},x}(t_1) = H_{\text{app},x}(t_2) \quad (5.17)$$

Of course, this is only valid if t_1 and t_2 are not too far away from the time corresponding to the maximum $H_{\text{app,max}}$. Using this assumption and combining formulas 5.12 and

5.15:

$$\frac{B_{\text{mag}}(H_{\text{app},x}(t_1)) - B_{\text{app}}(H_{\text{app},x}(t_1)) - \mu_0 M_{\text{eddy}}(H_{\text{app},x}(t_1))}{\mu_0 \cdot (1 - N_d)} = \quad (5.18)$$

$$\frac{B_{\text{mag}}(H_{\text{app},x}(t_2)) - B_{\text{app}}(H_{\text{app},x}(t_2)) - \mu_0 M_{\text{eddy}}(H_{\text{app},x}(t_2))}{\mu_0 \cdot (1 - N_d)}$$

$$B_{\text{mag}}(H_{\text{app},x}(t_1)) - B_{\text{app}}(H_{\text{app},x}(t_1)) + \mu_0 c_1 \kappa_{\text{mag}} \left. \frac{dB_{\text{mag}}}{dt} \right|_{H_{\text{app},x}(t_1)} = \quad (5.19)$$

$$B_{\text{mag}}(H_{\text{app},x}(t_2)) - B_{\text{app}}(H_{\text{app},x}(t_2)) + \mu_0 c_1 \kappa_{\text{mag}} \left. \frac{dB_{\text{mag}}}{dt} \right|_{H_{\text{app},x}(t_2)}$$

$$\kappa_{\text{mag}} = \frac{[B_{\text{mag}}(H_{\text{app},x}(t_1)) - B_{\text{app}}(H_{\text{app},x}(t_1))] - [B_{\text{mag}}(H_{\text{app},x}(t_2)) - B_{\text{app}}(H_{\text{app},x}(t_2))]}{\mu_0 c_1 \left[\left. \frac{dB_{\text{mag}}}{dt} \right|_{H_{\text{app},x}(t_1)} - \left. \frac{dB_{\text{mag}}}{dt} \right|_{H_{\text{app},x}(t_2)} \right]} \quad (5.20)$$

With this formula, the curves in Fig. 5.3 can be corrected and are shown in Fig. 5.4.

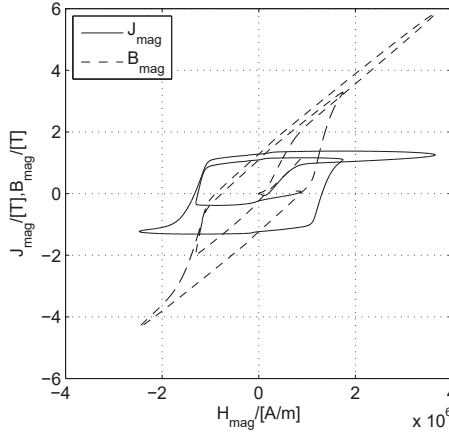


Fig. 5.3: Hysteresis curve of a NdFeB with eddy effects

For magnetizers where the maximum producible field strength is limited by the costs and the heating of the system, the magnets are not driven into over-saturation, so the developed method has to be modified (see section 5.2.9).

To find the geometry factor c_1 , a method introduced in [44] can be used. The magnet is replaced by a pure conductor, e.g. copper, which is not magnetic polarizable. Applying a pulsed field will result in a pure dynamic magnetization M_{eddy} , similar to the one shown in Fig. 5.4. Since the electric conductivity of the copper is known, formula 5.20 can be transposed to c_1 . It is important to heat treat the copper "magnets" at 650 °C for four hours to fully relief mechanical stress [44], which can be responsible for distortion of the electric conductivity. c_1 can only be used if formula 5.15 is valid for the magnet material and the copper, which is dependent on the skin effect. After finishing the development of the method, a patent [133] was found describing this method, but without giving any measured data.

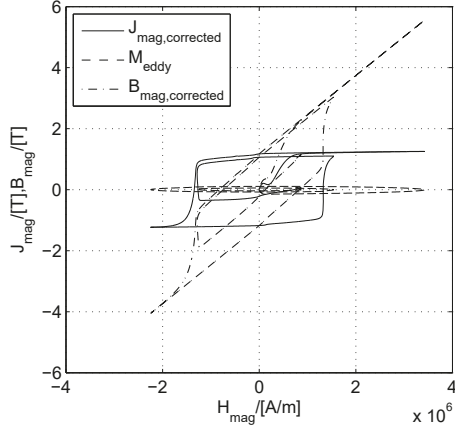


Fig. 5.4: Corrected Hysteresis curve of a NdFeB and J_{eddy}

5.1.4 Magnetic Viscosity

Magnetic viscosity in a PFM has been investigated by several authors [32, 38, 43, 55, 76, 86]. The magnetic viscosity describes a time dependent relaxation of the magnetization. Applying a static magnetic field, i.e. by a vibration sample magnetometer [55], one can state that the magnetization will differ from the one measured by a fast changing field. Physically, this can be explained by the wall domain motion whose equilibrium will be achieved asymptotically. The domain wall motion occurs at a distinct speed due to the mobility, which depends on the effective mass or inertia. Due to the thermal activation of the movement, it highly depends on the applied temperature. Therefore, it can be stated that the magnetic viscosity only depends on the material and temperature, but not on geometric factors. In [43], it is stated that it does not depend on $\frac{dH}{dt}$ - which cannot be confirmed by the statements made in [86].

[112] gives the following formula for the coercive field strength $H_{cJ}(t)$ - depending on the relaxation time t :

$$H_{cJ}(t) = \frac{8 \cdot \pi \cdot A_c \cdot K_c \cdot N_c}{k \cdot T \cdot M_s} \frac{1}{\ln\left(\frac{t}{\tau_0}\right)} \quad (5.21)$$

- A_c := Exchange energy
- K_c := Anisotropic energy
- N_c := Density of defects
- M_s := Saturation Magnetization
- k := Boltzmann Constant
- T := Temperature
- τ_0 := Magnetization reversal process time constant

τ_0 lies in between 10^{-12} s and 5×10^{-7} s and depends on the magnetization reversal process [112]. The constants of formula 5.21 are difficult to determine, but as can

be seen, the change in coercive field strength is not dependent on $\frac{dH}{dt}$. [32] built a PFM with a low oscillation time, minimizing the error resulting from eddy effects to measure the ΔH_{cJ} . The difference measured by the true hysteresis loop obtained by slow changing magnetic fields and the PFM was found to be in the order of about 10% of H_{cJ} - for a NdFeB magnet. A deeper analysis of this problem would go beyond the scope of this thesis, but should be considered when choosing the right measurement routine for the QCM.

5.1.5 Non-homogeneous fields and their Consequences on the demagnetizing Tensor

Non-homogeneous applied fields inside the magnets are a big problem. First, due to the anisotropic sintering process, the magnets only develop their full potential when magnetized along their easy axis. Second, the demagnetizing field becomes more complicated to calculate. The demagnetizing tensor \tilde{N}_d is composed of a diagonal matrix [5, 90]:

$$\tilde{N}_d = \text{diag} [n_{x,d}, n_{y,d}, n_{z,d}] \quad (5.22)$$

$$\text{trace}(\tilde{N}_d) = n_{x,d} + n_{y,d} + n_{z,d} = 1 \quad (5.23)$$

The analytical computation of \tilde{N}_d is difficult, and some approaches can be found in [5, 74, 90]. For cylinders with homogeneous applied fields in the easy axis, [17] gives comprehensive calculations.

For this dissertation, it was concluded that the demagnetizing factor can be approached by an FEA calculation and averaged over the entire probe. Hence, a known demagnetizing curve was used in the FEA. This approach is not fully correct, and only works if the field is homogeneous enough. Future studies have to show up to which angle, between field vector and easy axis of the magnet, this is technically functioning.

5.1.6 Demagnetization Tensor depending on Susceptibility

When analyzing materials in an open-loop measurement system like a PFM, the demagnetization tensor cannot be seen to be constant anymore. To understand this, one has to take a look back at formula 5.1 while neglecting the eddy currents. Considering just strict homogeneous fields, one can rewrite this formula as:

$$H_{\text{mag}} = H_{\text{app}} - H_{\text{demag}} \quad (5.24)$$

$$M_{\text{mag}} = [H_{\text{app}} - N_d(\chi_{\text{mag}}(H_{\text{mag}})) \cdot M_{\text{mag}}] \cdot \chi_{\text{mag}}(H_{\text{mag}}) \quad (5.25)$$

$$M_{\text{mag}} = \frac{\chi_{\text{mag}}(H_{\text{mag}})}{1 + \chi_{\text{mag}}(H_{\text{mag}}) \cdot N_d(\chi_{\text{mag}}(H_{\text{mag}}))} H_{\text{app}} \quad (5.26)$$

$$M_{\text{mag}} = \chi_{\text{mag,appa}}(H_{\text{mag}}) \cdot H_{\text{app}} \quad (5.27)$$

$$\chi_{\text{mag,appa}}(H_{\text{app}}) = \frac{\chi_{\text{mag}}(H_{\text{mag}})}{1 + \chi_{\text{mag}}(H_{\text{mag}}) \cdot N_d(\chi_{\text{mag}}(H_{\text{mag}}))} \quad (5.28)$$

$\chi_{\text{mag,appa}}(H_{\text{app}})$ is the apparent or external susceptibility [90]. So figuratively speaking, the apparent susceptibility links the magnetization M_{mag} to the external field H_{app} . Observing how $\chi_{\text{mag,appa}}$ changes if $\chi_{\text{mag}} \rightarrow \infty$:

$$\chi_{\text{mag,appa}} = \frac{\chi_{\text{mag}}(H_{\text{mag}})}{1 + \chi_{\text{mag}}(H_{\text{mag}}) \cdot N_{\text{d}}(\chi_{\text{mag}}(H_{\text{mag}}))} \xrightarrow{\chi_{\text{mag}} \rightarrow \infty} \frac{1}{N_{\text{d}}(\chi_{\text{mag},\infty})} \quad (5.29)$$

One can state now that for big χ_{mag} , the apparent susceptibility is governed by its shape. If $\chi_{\text{mag}} \rightarrow 0$, $\chi_{\text{mag,appa}}$ becomes 0 as well. Therefore, the following margin analysis can be performed:

Tab. 5.2: Demagnetizing factor N_{d} dependence

Material Property	value of χ_{mag} at working point	dominance
unsaturated ferromagnetic material	$\chi_{\text{mag}} \gg 0$	N_{d} depending on shape
magnet	$\chi_{\text{mag}} \rightarrow 0$	N_{d} depending on material

In context of the PFM, Tab. 5.2 can be interpreted as follows:

- $N_{\text{d}}(H_{\text{mag}})$ can be considered to be constant when analyzing the demagnetizing curve of a magnet in the second quadrant
- $N_{\text{d}}(H_{\text{mag}})$ is not constant at the magnetization curve or near the knee point, when χ_{mag} is large

Therefore, it is difficult to analyze magnetic materials, like $\text{Sm}_2\text{Co}_{17}$ or $\text{Ba}_1\text{Fe}_{12}$ magnets, where the demagnetizing curve looks similar to soft ferrites near the knee point [164]. To overcome the problem of $N_{\text{d}}(H_{\text{mag}})$, [128] proposed a toroidal specimen, where $N_{\text{d}}(H_{\text{mag}}) = 0$. Such a specimen is difficult to manufacture, especially when the material is anisotropic.

5.1.7 Temperature dependence of the demagnetizing Curves

As already concluded in section 5.1.3, eddy effects will influence the magnetic polarization by adding a $\frac{dB}{dt}$ dependent field. The eddy effects cause heating inside the magnet, and might influence the thermal working point of the magnet. Additionally, the field producing coils will heat up due to the high current, so that it has to be verified that this will not affect the magnetic thermal working point. For the PFM setup, the thermal barrier between the field coils and the sample holder was kept sufficiently large to avoid any heat flow. The heating of the magnet by eddy currents was estimated by a transient FEA during magnetization, and was below 4 K for a 255/200 magnet. Since most of the NdFeB magnets have similar electric conductivities, it was concluded that the eddy currents will not have an effect on the small cylindric magnet.

5.2 Designing the Quality Control Magnetizer

After discussing the PFM setup for single magnets in section 5.1, it is necessary to discuss the changes needed to convert it into a QCM for a rotor with inserted but non magnetized magnets.

5.2.1 Specifications for a Quality Control Magnetizer

As mentioned in section 1, handling magnetized magnets in a production environment can be difficult. Therefore, they are magnetized after inserting them into the rotor. Unfortunately, several aspects remain unknown after magnetization:

- Was the magnetization successful?
- Were all magnets inserted?
- Are all the magnets of sufficient quality?
- Would they survive a stator short without demagnetization?
- Do they have the correct electrical conductivity?

A QCM should be able to detect all these aspects during magnetization - also considering the following boundaries:

- It should be possible to integrate the quality control application into an already existent production line
- Quality control has to be non-destructive
- The quality control should show the variance of the magnetic material in terms of B_r , χ_{mag} and κ_{mag}
- No additional measurement station
- The additional tests should be done during magnetization, so that the station time is not affected
- The temperature inside the production environment might vary by 20 K, or even more depending on climatic conditions

5.2.2 Limitations of the developed Quality Control Magnetizer

For this dissertation, the limitations were set as follows:

- Each magnet is considered to have a uniform distribution of the specified magnet material, i.e. impurities at one particular place cannot be detected
- The rotor steel is of acceptable quality and does not have to be investigated
- The temperature of the magnets is uniform and known

- The pulse repetition of the device is set to 15 min
- The maximum life span is 1000 pulses, limited by the magnetizing fixture
- The magnetization unit is placed right next to the magnetizing pulse circuit to avoid long and expensive cables

5.2.3 Testing Oscillations

To satisfy all needs, an apparatus which is a mixture between a PFM and a pure magnetizer is built with an additional resistance R_{free} in its free wheeling circuit, as has already introduced in Fig. 4.8. In contrast to the PFM, the magnets inside the rotor are not driven around their complete hysteresis loop because that would demagnetize them. Afterwards, it would require more energy and a higher field strength to remagnetize them. Only heating them over the Curie temperature would result in a quasi-magnetic original state (see section 4.1.2). Therefore, the negative amplitude which drives the magnet into the demagnetizing quadrant is open loop controlled - to provide the largest magnetic stress the magnets have to withstand in a rotor's lifespan [25].

In Fig. 5.5, the QCM oscillation testing scheme is shown using an example of a hard magnetic material:

- The first half oscillation magnetizes the magnets
- The second half oscillation simulates the maximum magnetic stress
- Between second and third half oscillations the rotor magnets are rechecked for remnant flux density
- The third oscillation is used to estimate the electric conductivity

The conductivity has to be estimated in the third oscillation because it requires $J_{\text{mag}}(H_{\text{eff},4.1}) = J_{\text{mag}}(H_{\text{eff},4.2})$ (see section 5.1.3). Since $J_{\text{mag}}(H_{\text{eff},2-3})$ might change when applying the negative field, the third oscillation, because of its low H_{mag} , gives reliable information for κ_{mag} .

During the development of the QCM, it was also suggested that the permanent magnet material be characterized according to their magnetization curve. This can be applied, when eddy effects as well as magnetic viscosity can be neglected. The following sections will demonstrate why these effects are important to consider. Additionally, it might be interesting for the manufacturer of a motor to know how the demagnetizing curve of the permanent magnet material varies in-between the allowed magnetic tolerances, which is difficult to determine just by using the magnetization curve. Additionally, from the experience gained during testing, it is very hard to tell from the magnetization curve if the magnetization was successful - especially for NdFeB magnets.

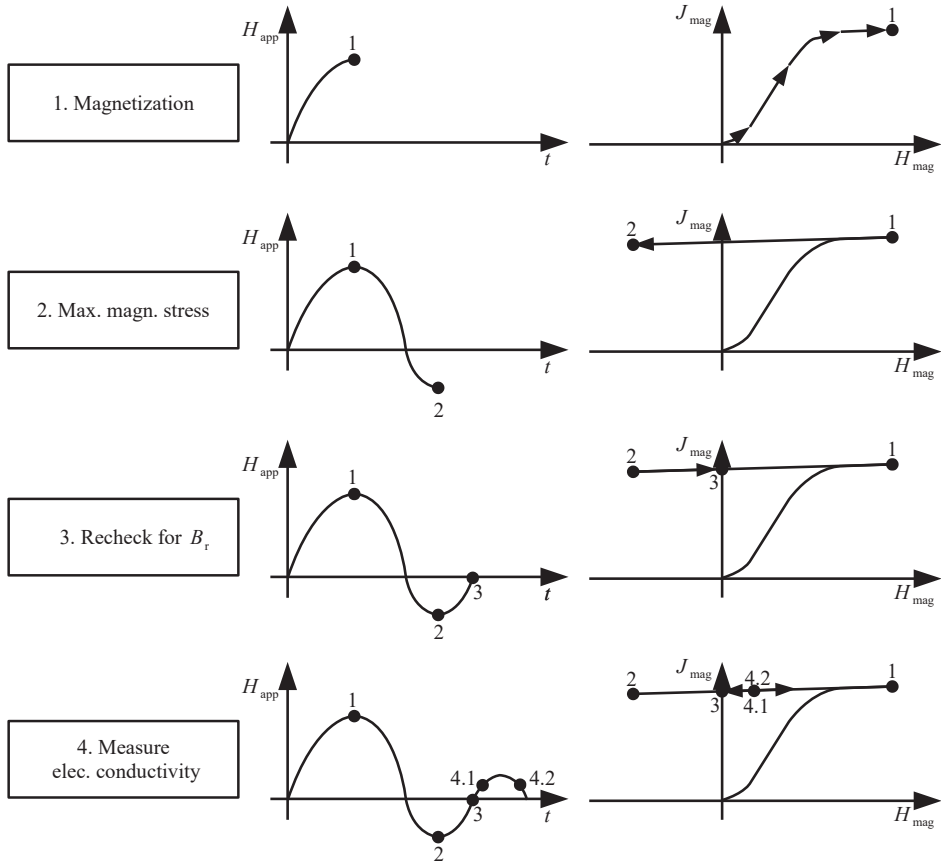


Fig. 5.5: Quality Control Magnetization Scheme

5.2.4 Arrangement of the Coils

The PFM coil arrangements shown in Fig. 5.7 have to be modified for a complete rotor. In Fig. 5.6, the cross section of a QCM is shown. The field coils are placed around and inside the rotor so that the rotor magnets are saturated according to Tab. 4.1. Search coils are placed around the magnets. Looking at Fig. 5.8, the search coils measuring the signals B_{mag} and B_{app} are placed in a similar way to Fig. 5.7. Underneath the B_{app} search coil, the compensator rotor is placed. The compensator is equal to the laminations of the rotor, but does not have to have the same length. It should compensate for part of the saturation, eddy current and hysteresis influences of the rotor. The rotor and compensator are placed in a certain distance from each other, so that the influence of the field from the magnets is lower than 0.5% of the maximum field amplitude of the magnets. The compensator is 2/3 smaller when compared to the real rotor to limit the inductance and the power losses inside the field coils. Hence, the magnetic flux linkage is kept the same by increasing the number of turns N_2 of the

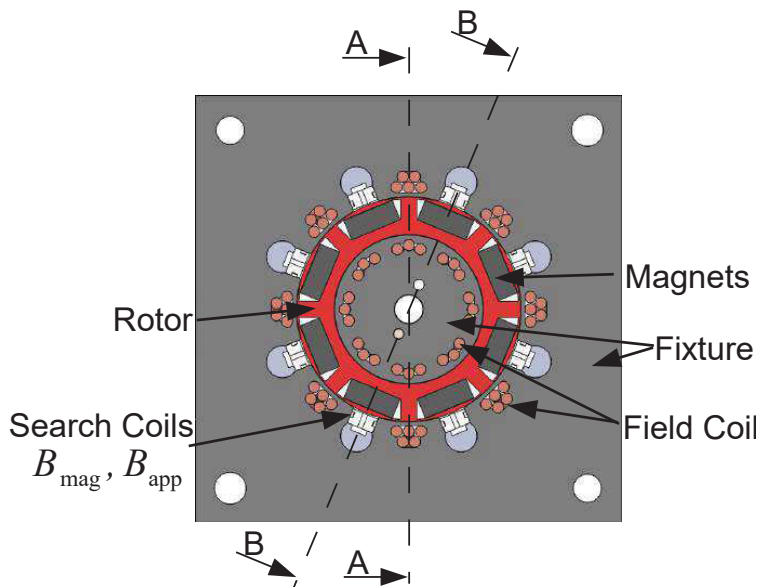


Fig. 5.6: Schematic cross section of the QCM with cuts A-A and B-B

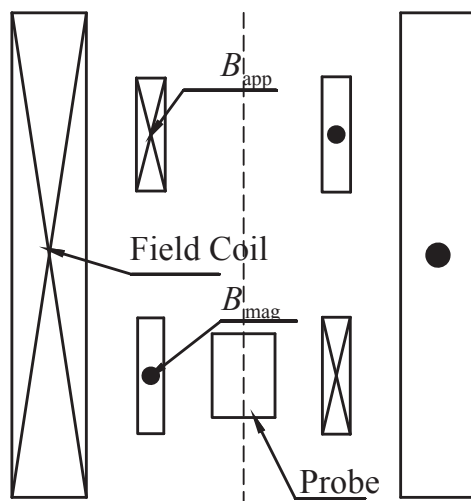


Fig. 5.7: Schematic cross section of a cylindrical PFM equal to Fig. 5.2

B_{app} coil, so that if no magnets are inserted $\int_{A_1} N_1 \cdot B_{\text{mag}} \cdot dA'_1 - \int_{A_2} N_2 \cdot B_{\text{app}} \cdot dA'_2 = \Psi_{\text{mag}} - \Psi_{\text{app}} = 0$.

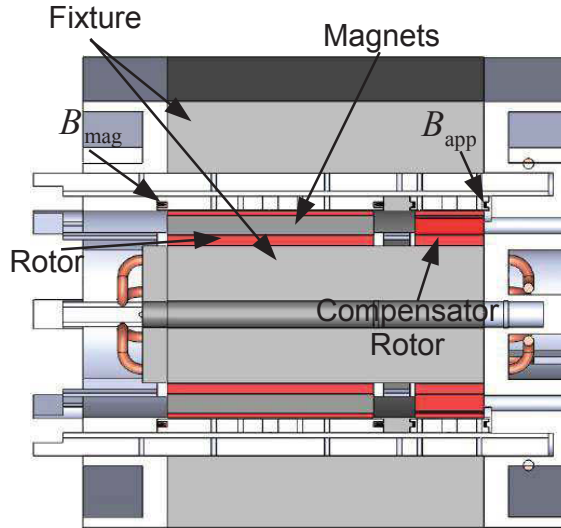


Fig. 5.8: Cut B-B of Fig. 5.6

5.2.5 Field and Force Calculations for the Coils

At the maximum current of 30,438 A, the applied field is big enough to fully saturate the magnets as can be seen in Fig. 5.10. All windings are wound in series summing up to a total of 8 turns per pole. The magnets are not penetrated by a fully homogeneous field, even though the inside windings help to homogenize the field. In [141], several other winding topologies are investigated, stating that the configuration with inside and outside windings gives the best results in terms of maximum saturation, and field angle inside the magnets. The design satisfies all requirements mentioned in section 4.5. As seen in Fig. 5.6, the search coils are mounted as close as possible to the rotor at a very homogeneous part of the field.

The Lorentz forces have to be considered iteratively when setting up the minimum material strength above the inner part of the fixture. From a magnetic FEA, the forces are calculated and then inserted into a structural FEA. Since the force is constant along the wire, a 2D structural FEA can be conducted. For the fixture, a glass fiber material was used. With the experience gained from section 2.4.1, the total safety factor was set to 8 for the inner windings. During winding, the thin bridges above the wires broke at the intake points, so the safety factor was increased to 14.

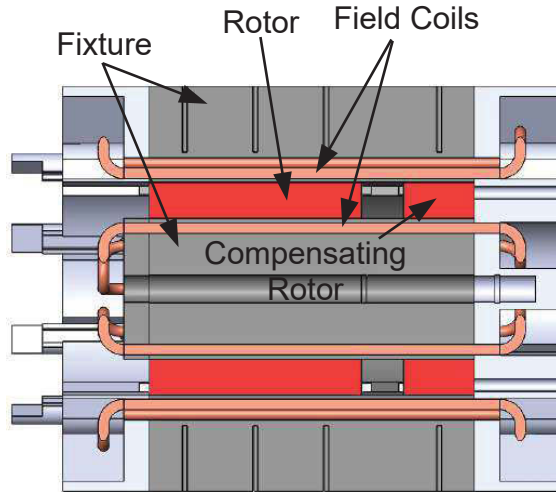


Fig. 5.9: Cut A-A of Fig. 5.6

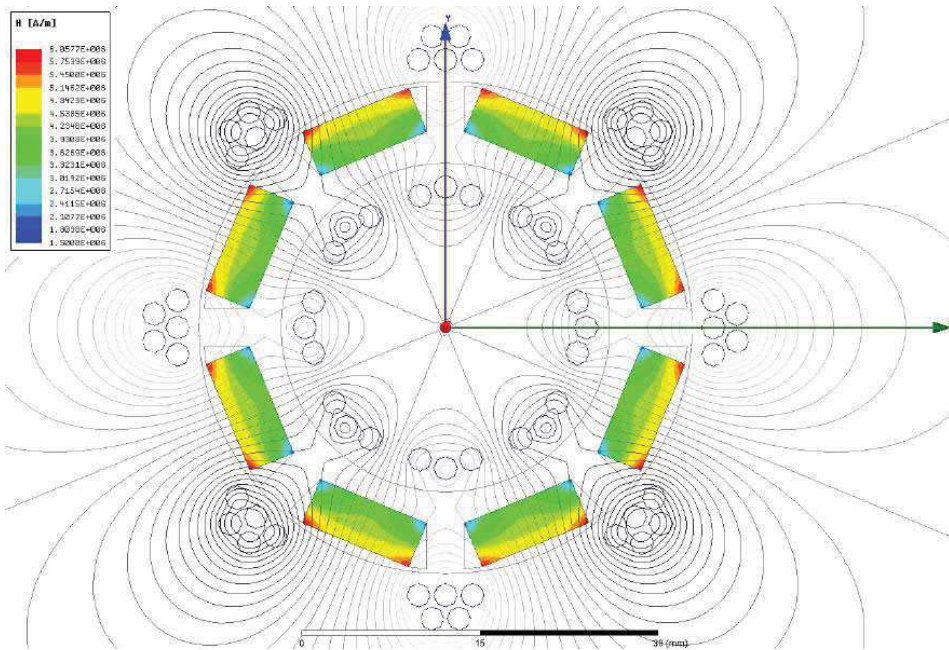


Fig. 5.10: Applied Field at 30,438 A winding current

5.2.6 The demagnetizing Factor/Function

Before applying the effects discussed for the PFM, one has to take a look into the fundamental formulas of the PFM. The operation mode of the PFM depends on knowing the demagnetizing factor N_d . As stated, this factor links the apparent with the intrinsic field. For the PFM with a cylindrical probe, this can easily be analytically calculated. For the geometry shown in Fig. 5.10, this is slightly more difficult because of:

- Neighboring magnets
- Saturation curve of the rotor steel

The demagnetizing factor becomes a function of these effects. So instead of a factor, it will be discussed as a function, referred to as the \mathfrak{D} -function. To estimate this function in a homogeneous field, formula 5.12 will be rewritten as:

$$M_{\text{mag}} = \frac{B_{\text{mag}} - B_{\text{app}} - \mu_0 M_{\text{eddy}}}{\mu_0 \cdot (1 - \mathfrak{D})} \quad (5.30)$$

$$\mathfrak{D} = \frac{B_{\text{app}} - B_{\text{mag}} - \mu_0 M_{\text{eddy}}}{\mu_0 M_{\text{mag}}} + 1 \quad (5.31)$$

The H_{mag} also depends on the \mathfrak{D} -function:

$$H_{\text{mag}} = H_{\text{air}} - \mathfrak{D} \cdot M_{\text{mag}} - M_{\text{eddy}} \quad (5.32)$$

$H_{\text{air}} :=$ Magnetic field in a magnet and steel free environment

Taking a closer look at formula 5.32, one can see that the former H_{app} is replaced by H_{air} . This is the field proportional to the load current, without the influence of the rotor steel. This has to be done in case of the QCM, because the applied field H_{app} is influenced by the compensator rotor which will give false information about the intrinsic magnetic field inside the magnet. To save an extra H_{air} coil, the load current, which is directly proportional to the field, is fitted corresponding to the H_{air} field. This fitting can be done with an empty magnetizer without the influence of the magnets or rotor steel. To solve formula 5.32, one has to measure the intrinsic field H_{mag} inside the magnet while applying the current inside the field coils. This can be solved with an FEA measuring the intrinsic flux density, the intrinsic field strength and the average magnetization inside the magnet. Since the search coils are not directly wound around the magnets, the effective area fitting factor $X_{A,\text{fit}}$ introduced for the PFM has to be used to account for the distance. Because of the saturation curve of the steel, this factor also becomes a function and will be referred to as the $\mathfrak{X}_{A,\text{fit}}$ -function. In section 6.3.1 and 6.4, it is explained how this function is composed for the PFM and the QCM, respectively.

In Fig. 5.11, the \mathfrak{D} -function for equipped rotors with different kinds of steel is shown, depending on the current in the second half oscillation (see Fig. 5.5). The current is

limited to $-5,700$ A before the resulting field becomes too big, and the demagnetization of the 255/200 magnets used for this application starts. The \mathfrak{D} -functions for M330-35A and M270-35A steel are very similar. The simulations were conducted with a current pulse with 2,000 Hz.

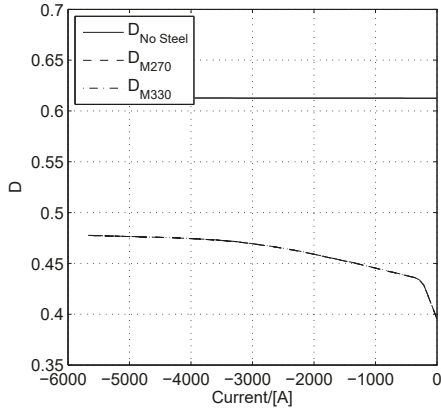


Fig. 5.11: \mathfrak{D} -function for different kind of steels and no steel vs. negative current of the second half oscillation

When replacing the steel with a non-conductive material, the \mathfrak{D} -function becomes almost constant over the entire current. This is of course only valid if the susceptibility stays almost constant, as shown in section 5.1.6. If the susceptibility changes, the \mathfrak{D} -function also changes as shown in Fig. 5.12, where the \mathfrak{D} -function for a $\text{Sr}_1\text{Fe}_{12}\text{O}_{19}$ 28/26 magnet [190] is shown. The magnet loses its magnetization at around -250 A. Starting from this point, the \mathfrak{D} -function also starts do change.

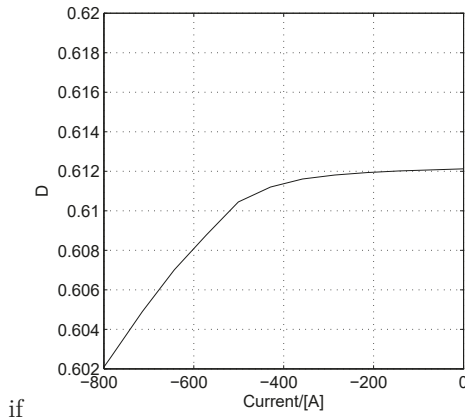


Fig. 5.12: \mathfrak{D} -function for a $\text{Sr}_1\text{Fe}_{12}\text{O}_{19}$ 28/26 magnet [190], demagnetizing at around -250 A for a non-conductive rotor

The \mathfrak{D} -function for the steels are somehow related to the virgin curve of the steel. This means that the compensator rotor does not fully compensate for the impact of the

steel, because the magnets in the rotor steel result in different saturations. This also means that a different magnet will result in a different \mathfrak{D} -function. The aim of the following sections will be to discuss how accurate the measured demagnetizing curve of a magnet close to the reference 255/200 magnet will be, when the reference \mathfrak{D} -function is used.

5.2.7 The reference demagnetizing Function for different Magnets

In a QCM, unknown magnets are tested usually for their quality. In the section before, the \mathfrak{D} -function was obtained by using a reference magnet with a known demagnetizing curve. Now it is interesting to see how a modified magnet will be measured in a QCM with the help of the reference \mathfrak{D} -function. Looking at Fig. 5.14, one can see how the magnets would be measured in a QCM using the reference \mathfrak{D} -function for a 255/200 magnet with $B_r = 1.21$ T and $\mu_r = 1.04$. The QCM over-estimates J_{mag} of a magnet with poorer B_r , but $\mu_r = 1.04$. This changes when investigating a magnet with $B_r = 1.16$ T and $\mu_r = 1.03$. In case of a different μ_r , the QCM underestimates J_{mag} . The \mathfrak{D} -functions caused by the different magnets shown in Fig. 5.13 are very close to

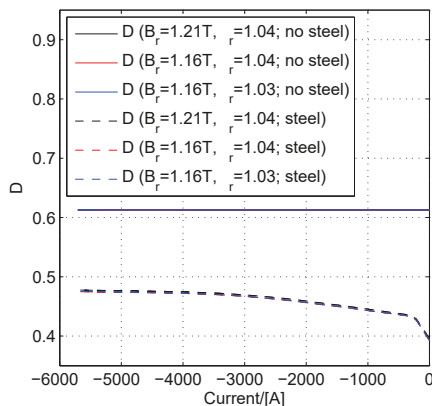


Fig. 5.13: \mathfrak{D} -function for different magnets without steel and with M330-35A

each other, but still dependent on the saturation curve of the steel.

The simulations have shown that the QCM can detect the demagnetizing curve of a magnet in certain ranges depending on the permeability and remnant flux density differences among the magnets. Eddy effects and differences in steel quality will be discussed in the next sections.

5.2.8 Detection of Demagnetization

As mentioned earlier in section 5.2.3, the second half oscillation stresses the magnets and drives them deep into the second quadrant in a $J_{\text{mag}}(H_{\text{mag}})$ plane, before partial

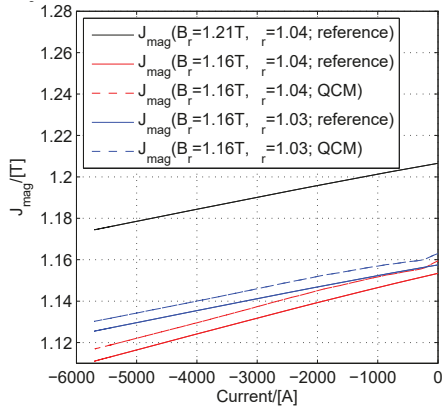


Fig. 5.14: Comparison of magnets measured with the QCM and a \mathfrak{D} -function obtained with a reference 255/200 magnet

demagnetization takes place. In Fig. 5.15 J_{mag} of one magnet at a demagnetizing field corresponding to a negative current of $-8,200$ A is shown. The magnet is partially demagnetized at this point. The demagnetization starts at the upper corners, where the magnetizing field (compare Fig. 5.10) has been the strongest. The QCM is only

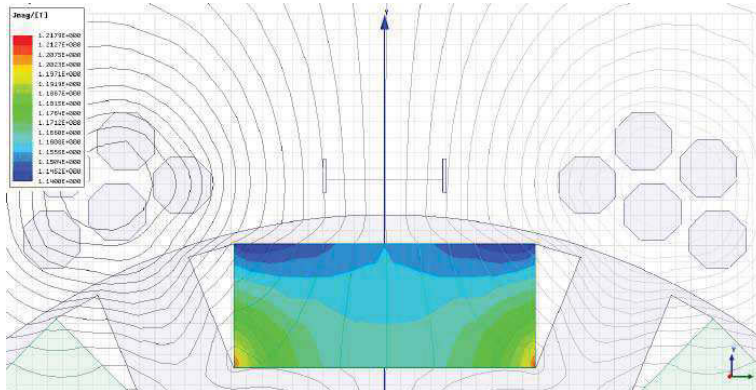


Fig. 5.15: J_{mag} of a reference 255/200 magnet at $-8,200$ A

able to detect an average polarization of the corresponding magnet. A simulation with the following parameters can be done to find out at which point the QCM starts to detect demagnetization:

- Usage of the \mathfrak{D} -function corresponding to a 255/200 magnet
- Simulation with modified magnet

Same χ_{mag} but different $H_{\text{cJ,min}}$ (1,000 kA/m instead of 2,000 kA/m)

- Negative half oscillation with $-5,700$ A peak

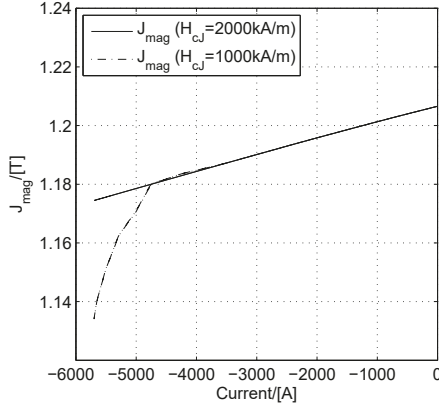


Fig. 5.16: J_{mag} measured with QCM of a reference 255/200 magnet with $H_{cJ,\text{min}}=2,000$ kA/m and a modified 255/200 magnet with same $\chi_{\text{mag,ref}}$ but $H_{cJ,\text{min}}=1,000$ kA/m measured with the reference \mathfrak{D} -function

In Fig. 5.16, the demagnetizing curve measured in the QCM of the reference 255/200 magnet and the one with a smaller $H_{cJ,\text{min}}$ are shown. The latter is measured using the reference \mathfrak{D} -function obtained from the 255/200 reference magnet. Secure detection of the demagnetization can be obtained starting from $-4,730$ A, even though it already started at $-4,000$ A.

5.2.9 Eddy Effects

As introduced in section 5.1.3 eddy effects have a big influence on the measurement of the hysteresis loop. The simple calculations mentioned in section 5.1.2 have to be adopted for the setup of a QCM, resulting in the following difficulties:

- Magnets are not cylindric anymore
- Additional hysteresis from the rotor laminations
- Skin penetration depth is not uniform
- Non-uniform electric conductivity

In our case, the magnets are ashlar-formed. Starting from Maxwell's equation:

$$\oint_s \vec{E} \cdot d\vec{s} = - \int_A \frac{d}{dt} \vec{B}_{\text{mag}} \cdot d\vec{A} = - \frac{d}{dt} \Phi_{\text{mag}} \quad (5.33)$$

$$\oint_s \vec{E} \cdot d\vec{s} = I_{\text{seg}} \cdot R_s(\vec{s}) \quad (5.34)$$

Looking at Fig. 5.17 the field is only considered to have a z-component, which will cause approximately rectangular eddy currents. Therefore, $R_s(\vec{s})$ can be rewritten

as:

$$R_s = 2 \frac{2y}{\kappa_{\text{mag}} \cdot \Delta x \cdot \Delta z} + 2 \frac{2x}{\kappa_{\text{mag}} \cdot \Delta y \cdot \Delta z} \quad (5.35)$$

$$\frac{\Delta x}{\Delta y} = \frac{x}{y} = \frac{w}{h} \quad (5.36)$$

$$y = \frac{x \cdot h}{w} \quad (5.37)$$

$$R_s = \frac{4}{\kappa_{\text{mag}} \cdot \Delta z} \frac{x}{\Delta x} \frac{h}{w} \left[1 + \left(\frac{w}{h} \right)^2 \right] \quad (5.38)$$

Formula 5.33 can be converted into:

$$\Phi_{\text{mag},z} = \int_{-x}^{+x} \int_{-y}^{+y} \vec{B}_{\text{mag}} \vec{e}_z dy dx = 4xy B_{\text{mag},z} \quad (5.39)$$

Inserting formula 5.38 into 5.34 and using 5.39 together with the parameterization 5.37 leads to:

$$I_{\text{seg}} = \frac{\kappa_{\text{mag}} \cdot x \cdot \frac{dB_{\text{mag},z}(t)}{dt}}{\left[1 + \left(\frac{w}{h} \right)^2 \right]} \Delta z \cdot \Delta x \quad (5.40)$$

According to the Biot-Savarts law, this current will cause an opposing field $B_{\text{mag},z}(t)$.

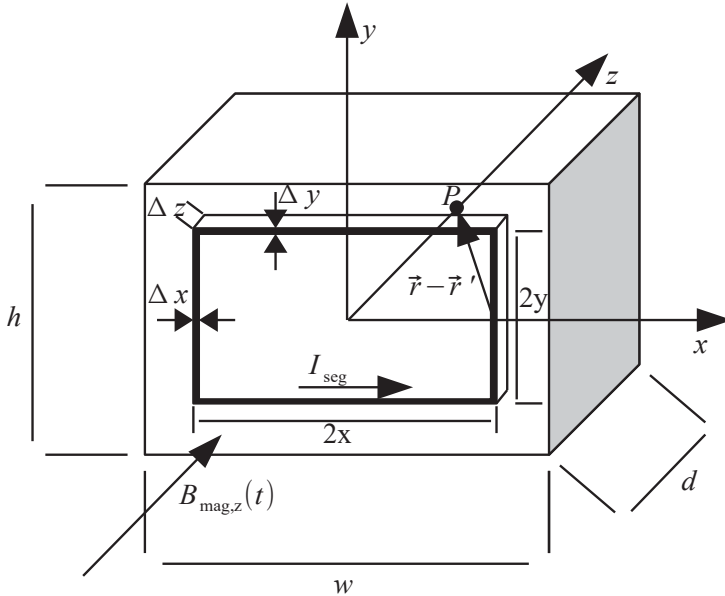


Fig. 5.17: Simplified eddy currents resulting from field $B_z(t)$

Two symmetries, one in y- the other in x-direction, can be obtained:

$$H_{z,y} = \frac{I_{\text{seg}}}{4\pi} \int_0^y \left[\vec{e}_y \times \frac{\vec{r} - \vec{r}'}{|\vec{r} - \vec{r}'|^3} \right] \vec{e}_z dy' \quad (5.41)$$

Replacing \vec{r} and \vec{r}' by

$$\vec{r} = z\vec{e}_z \quad (5.42)$$

$$\vec{r}' = x\vec{e}_x + y'\vec{e}_y \quad (5.43)$$

and inserting them into 5.41:

$$H_{z,y} = \frac{I_{\text{seg}}}{\pi} \int_0^y (\vec{e}_z \times \vec{e}_y) \frac{z\vec{e}_z - (x\vec{e}_x + y'\vec{e}_z)}{(x^2 + y'^2 + z^2)^{3/2}} dy' \quad (5.44)$$

$$= \frac{I_{\text{seg}}}{\pi} \int_0^y \frac{x}{(x^2 + y'^2 + z^2)^{3/2}} dy' \quad (5.45)$$

$$= \frac{I_{\text{seg}}}{\pi} \frac{xy}{(x^2 + z^2)(x^2 + y^2 + z^2)^{3/2}} \quad (5.46)$$

The symmetry in x-direction leads to:

$$H_{z,x} = \frac{I_{\text{seg}}}{\pi} \frac{yx}{(y^2 + z^2)(x^2 + y^2 + z^2)^{3/2}} \quad (5.47)$$

Now all currents have to be considered. Hence, the ashlar will be discretized using N and M pieces:

$$w = N\Delta x \quad (5.48)$$

$$h = N\Delta y \quad (5.49)$$

$$d = M\Delta z \quad (5.50)$$

The variables x, y, z have to be transformed to account for the discretization with the index variables n and m :

$$x \rightarrow x_n = (n - \frac{1}{2})\Delta x \quad (5.51)$$

$$y \rightarrow y_n = (n - \frac{1}{2})\Delta y \quad (5.52)$$

$$z \rightarrow z - z_m = z - (m - \frac{1}{2})\Delta z \quad (5.53)$$

In this case the resistance (formula 5.38) becomes:

$$R_s = \frac{4}{\kappa_{\text{mag}} \cdot \Delta z} \frac{x_n}{\Delta x} \frac{h}{w} \left[1 + \left(\frac{w}{h} \right)^2 \right] \quad (5.54)$$

Now the dynamic magnetization $M_{\text{eddy,rect},z}(z, t)$ using formulas 5.40, 5.46, 5.47, 5.48, 5.49 can be described:

$$M_{\text{eddy,rect},z}(z, t) = -\kappa_{\text{mag}} \frac{dB_{\text{mag},z}(t)}{dt} \cdot \underbrace{\frac{\frac{w}{N} \frac{d}{M}}{\pi \left[1 + \left(\frac{w}{h} \right)^2 \right]} \cdot \sum_{m=1}^M \sum_{n=1}^N \frac{x_n y_n}{(x_n^2 + y_n^2 + (z - z_m)^2)} \left[\frac{1}{x_n^2 + (z - z_m)^2} + \frac{1}{y_n^2 + (z - z_m)^2} \right]}_{c_2} \quad (5.55)$$

This formula includes a lot of assumptions. First, the current will not flow in a rectangular manner in parts of the magnet; second, the field $B_{\text{mag},z}$ does not include the influence of the eddy current; third, it is only valid if the skin depth $\delta_{\mu,r}$ is bigger than d . So the real field causing the eddy currents will be smaller. This formula shows that the conductivity is the only parameter not dependent on the geometry. Since the field in the application is not uniform as assumed above, it is better to measure the so called geometry factor, in this case c_2 , similar to the PFM method. Therefore, a pure dynamic eddy polarization in z-direction at a distinct distance z is assumed:

$$M_{\text{eddy,rect},z}(t) = -\kappa_{\text{mag}} \frac{dB_{\text{mag},z}(t)}{dt} c_2 \quad (5.56)$$

This factor can be estimated by inserting a non-ferromagnetic material with a known κ_{mag} , which is not subject to the skin effect at the given test frequency. Knowing c_2 , formula 5.20 can be used to calculate κ_{mag} and eventually $M_{\text{eddy,rect},z}(t)$.

5.2.10 Magnetic Viscosity

The magnetic viscosity can change the real hysteresis curve of a permanent magnet when obtained in an oscillating field. When analyzing the effect in a QCM, one has to investigate the effect at regions with reversible susceptibility χ_{rev} and irreversible susceptibility χ_{irr} . The slope at any given point of the magnetization curve $OABC$

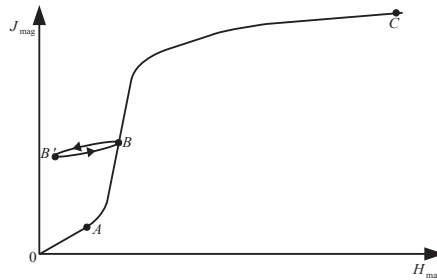


Fig. 5.18: Reversible χ_{rev} and irreversible χ_{irr} susceptibility of the polarization curve [19]

(see Fig. 5.18) is defined as the differential susceptibility χ_{diff} . The slope of the curve OA is called the initial susceptibility χ_a . Increasing the magnetic field strength H_{mag} beyond point A leads to an irreversible magnetization whose slope is defined as χ_{irr} . If the field is increased until the point B , the magnetization does not come back along the BAO line, but in the minor loop BB' . Increasing the field until point C results in a large reversible susceptibility χ_{rev} which is repelled when crossing the knee point in the second quadrant of the $J_{\text{mag}}(H_{\text{mag}})$ plane. χ_{diff} can be written as [19]:

$$\chi_{\text{diff}} = \chi_{\text{rev}} + \chi_{\text{irr}} \quad (5.57)$$

Considering a magnet under the influence of the magnetic viscosity S , the polarization $J_{\text{mag}}(t)$ can be written as follows [46, 47, 65]:

$$J_{\text{mag}}(t) = J_{\text{mag}}(0) - S \ln \frac{t}{\tau_0} \quad t > \tau_0 \quad (5.58)$$

$$J_{\text{mag}}(t) = J_{\text{mag}}(0) - \frac{S_v \chi_{\text{irr}}}{1 - N_d \chi_{\text{rev}}} \ln \frac{t}{\tau_0} \quad t > \tau_0 \quad (5.59)$$

$$S_v = - \frac{k \cdot T}{\frac{dE}{dH}} \quad (5.60)$$

S_v is the magnetic viscosity related to the activation volume v , $\frac{dE}{dH}$ can be interpreted as the differential energy barrier with respect to intrinsic field change. It is said in [46] that $S_v \propto H_{cJ}^{1.5}$ for various types of magnet material. Going back to formula 5.59, one can see that in case $\chi_{\text{irr}} \rightarrow 0$, the magnetic viscosity effect is of minor importance; as also proven by [32]. Therefore, it might be more suitable to analyze the quality of a magnet in the second quadrant rather than by analyzing the magnetization curve, where $\chi_{\text{irr}} \gg 1$. In the latter case, temperature fluctuations have a direct influence on S_v (see formula 5.60) which does not enhance the quality estimation in a production environment.

[31] gives magnetic viscosity values for commercially available NdFeB magnets measured with a Hall probe after magnetization, using formula 5.58. It is noted that because of EMI and trigger problems, the field decay could not be measured at the very early point of magnetization.

Tab. 5.3: Magnetic viscosity values S measured by [31] for different NdFeB at J_{max}

Magnetic material	B_r	H_{cJ}	S
210/220h	1.12 T	2,500 kA/m	19×10^{-4} T
270/95h	1.28 T	1,100 kA/m	5.5×10^{-4} T

5.2.11 Temperature Dependence of the demagnetizing Curves

Analyzing the temperature dependence in a QCM is similar to the PFM. The only difference is the absence of a big thermal insulator between the coils and the magnets. Therefore, it might be useful to investigate how the heat from the coils is conducted to the rotor, and eventually to the magnets. A thermal model similar to the one used for the stator in section 3 was adapted for the field coils. The analytical model was then verified by an FEA. By applying the testing oscillations mentioned in section 5.2.3, the temperature rose by only 5 K inside the magnets. The heat from the coils show a moderate temperature increase inside the magnets after the oscillations of about 15 K, when the rotor is kept inside for thirty seconds. Because of the low heating of the magnets during the oscillations, the temperature effect was not investigated any further.

5.2.12 Influence of neighboring Magnets

Magnets due to their production tolerances produce different fields inside the air gap of a BLDC. When analyzing them in the QCM the fields are influencing each other, so a single magnet cannot be characterized absolutely. In Tab. 5.4, 4 common cases which are analyzed among three neighboring magnets are shown. It turned out, that the coupling between other pairs of magnets is insignificant, and therefore not investigated any further. Case 0 describes the ideal state, whereby all magnets have the same properties.

Tab. 5.4: Differences of neighboring magnets in terms of magnetic behaviour

	left neighbor magnet	center magnet	right neighbor magnet
Case 0	$B_{r,c}$ $\chi_{mag,c}, \mu_{mag,c}$	$B_{r,c}$ $\chi_{mag,c}, \mu_{mag,c}$	$B_{r,c}$ $\chi_{mag,c}, \mu_{mag,c}$
Case 1	$B_{r,l}$ $\chi_{mag,c}, \mu_{mag,c}$	$B_{r,c}$ $\chi_{mag,c}, \mu_{mag,c}$	$B_{r,r}$ $\chi_{mag,c}, \mu_{mag,c}$
Case 2	$B_{r,c}$ $\chi_{mag,x}, \mu_{mag,x}$	$B_{r,c}$ $\chi_{mag,c}, \mu_{mag,c}$	$B_{r,c}$ $\chi_{mag,x}, \mu_{mag,x}$
Case 3	$B_{r,l}$ $\chi_{mag,l}, \mu_{mag,l}$	$B_{r,c}$ $\chi_{mag,c}, \mu_{mag,c}$	$B_{r,r}$ $\chi_{mag,r}, \mu_{mag,r}$
Case 4	$B_{r,x}$ $\chi_{mag,x}, \mu_{mag,x}$	$B_{r,c} = 0$	$B_{r,x}$ $\chi_{mag,x}, \mu_{mag,x}$

In case 1 mentioned in Tab. 5.4, all magnets have the same permeability/susceptibility but different B_r . In case 2, all magnets have the same B_r , but different μ_{mag}/χ_{mag} . Case 3 describes the most realistic state, where all magnets have different μ_{mag}/χ_{mag} and remnant flux densities. Case 4 assumes a missing center magnet. To understand these influences better, Tab. 5.5 gives a small example of how the different properties will affect the measurements within a QCM. B_r of each magnet is measured within a QCM, and alone in a permeagraph. μ_{mag} is measured only in a permeagraph. Case

Tab. 5.5: Differences between measurements with QCM, and permeagraph influenced by neighboring magnets with different μ_{mag} and B_{mag} ; μ_{mag} is only measured with a permeagraph

	left neighbor magnet		center magnet		right neighbor magnet	
	B_r measured with QCM/permeagraph		B_r measured with QCM/permeagraph		B_r measured with QCM/permeagraph	
	μ_{mag}	B_r in [T]	μ_{mag}	B_r in [T]	μ_{mag}	B_r in [T]
Case 0	1.03	1.21/1.21	1.03	1.21/1.21	1.03	1.21/1.21
Case 1	1.03	1.20/1.21	1.03	1.18/1.16	1.03	1.20/1.21
Case 2	1.03	1.20/1.21	1.04	1.20/1.21	1.03	1.20/1.21
Case 3	1.03	1.20/1.21	1.04	1.18/1.16	1.03	1.20/1.21
Case 4	1.03	1.07/1.21	x	0.21/0	1.03	1.07/1.21

1 shows that QCM will not detect the correct B_r since the neighboring magnets will affect each other even though the error is very small. Case 2 shows the state for the same remnant flux density but different permeability. This affects the values obtained

by the QCM in the same way as case 1, since the working point of the magnet will be different. If the susceptibility of the magnet material also changes, the demagnetizing factor/function changes. So to get the correct values for B_r one has to know the susceptibility prior. With a QCM, it is only possible to measure B_r within certain tolerances. Case 3 marks a realistic combination, whereby B_r and the susceptibility vary compared to their neighboring magnets. The differences of the real and measured data are small but detectable. Case 4 shows the results for a missing center magnet. The impact can be detected well.

5.2.13 Mechanical Tolerances

The rotor steel and the magnets themselves have mechanical tolerances. These tolerances have an impact on the field, so that the search coils have to be compensated. This is one of the key issues and can be solved with an FEA optimization algorithm. Beforehand, it is chosen to place the search coil outside of the outer diameter of the rotor because of manufacturability reasons. The coils should be placed as close as possible to the rotor magnets to maximize the detectable flux. Hence, this distance is only limited by manufacturability and fixed in the optimizer. The optimizer varies the width of the coil. One goal is to maximize the flux through the coil while still being immune to mechanical tolerances. Two different mechanisms of mechanical tolerances are investigated:

- Mechanical offset of the magnet ± 0.1 mm
- Eccentricity of the rotor including magnets ± 0.1 mm to ± 0.2 mm

The direction of the displacements is sketched in Fig. 5.19. For the simulation, it is

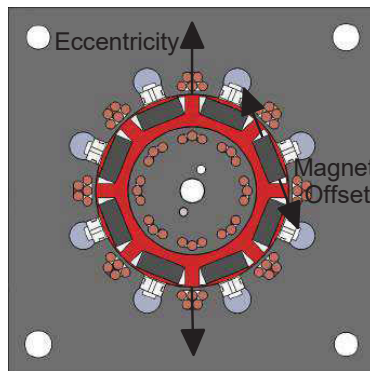


Fig. 5.19: Sketch of investigated tolerances

assumed that the demagnetizing \mathfrak{D} -function is measured with a perfectly positioned system. Additionally, it is assumed that the compensator rotor is also perfectly positioned. Now the tolerated rotor with the magnets is inserted. In Fig. 5.20, the impact of the mechanical tolerances is shown. A magnet offset has little impact. Eccentricity

of the whole rotor including magnets is more challenging. As a result, the rotor has to have a very smooth surface, and the tolerance for the bore hole of the magnetizer has to be kept as small as possible.

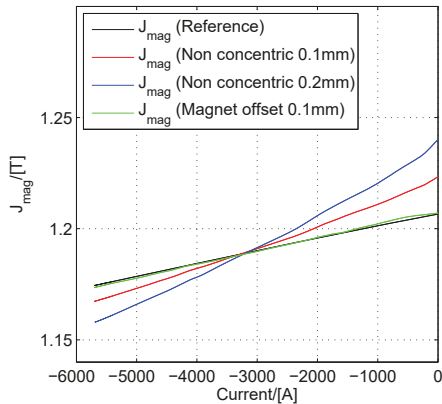


Fig. 5.20: Impact of mechanical tolerances on the measurement of J_{mag} in a QCM

5.2.14 Variations in Rotor Steel

When trying to compensate for the rotor steel effects, one not only has to consider different magnetic working points inside the compensator and the rotor steel, but also variations inside the lamination production batch. Variations will have an impact on:

- The saturation curve
- The hysteresis curve
- Different eddy current losses due to steel quality
- Eddy effects caused by the burrs of the stacked laminations [50]

It is difficult to get significant information on how much the quality of the lamination might vary in production, since influences like the wear of the cutting tool also have a big impact on the saturation curve [50]. In Fig. 5.21, the 255/200 magnets are measured once with a system where rotor and compensator are made out of the same material M330-35A, and once more where the rotor laminations are changed to M270-35A. For both simulations, the reference \mathfrak{D} -function is used. As can be seen, the differences are negligible.

5.2.15 Hysteresis of the Compensator Steel

Another tolerance error might occur if the compensator and rotor have different hysteresis curves. In this case, it is assumed that the difference of the hysteresis would be

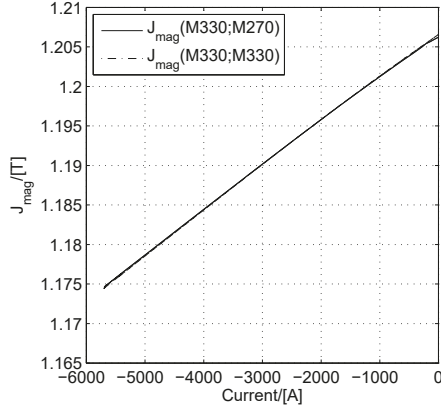


Fig. 5.21: Polarization result of magnetic stress of 255/200 magnets in the QCM with M270-35A and M330-35A rotor steel and M330-35A compensator [197]

accounted incorrectly for additional magnet polarization. Hysteresis is one of the more difficult aspects in numerical magnetic field calculations. There are several models for calculating hysteresis:

- Preisach model [59]
 - only the basic hysteresis curve is needed as an input
 - high accuracy
 - high computational cost
 - in the basic version, it does not account for rotational fields
- Jiles Model [22]
 - is derived from a more physical model of the hysteresis
 - several factors have to be fitted to the hysteresis curve
 - less accurate
- Vector play models [84, 85]
 - only the basic hysteresis curve is needed as an input
 - high accuracy
 - low computational costs
 - accounts for rotational field

ANSYS[®] Maxwell[®] uses the latter-most model. It is not intended by the author to carry out detailed simulations to compare these models. This will be done in a follow up Ph.D. thesis and for the reason of delimiting those research activities, it will not be discussed any further.

To find out if possible differences in the hysteresis might be a problem for the QCM,

different hysteresis curves were implemented for the compensator and the rotor. Similar to the simulations mentioned before, the demagnetizing function was calculated with the compensator and rotor having the same hysteresis. Then the rotor was changed to have a different lamination package with different hysteresis. Unfortunately, it was very difficult to find data on how much the hysteresis would vary in production, hence the hysteresis difference was estimated to be about 20% in the worst case scenario, considering the DC curve (see Fig. 5.22). The differences in the demagnetizing curve obtained by the QCM are below 0.135 mT and can be neglected.

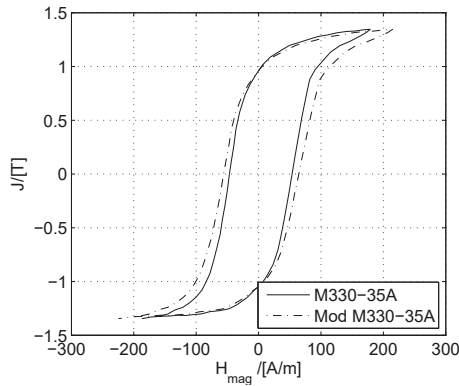


Fig. 5.22: DC hysteresis curve of M330-35A as well as H_{mag} modified by 20%

5.2.16 Steel for the magnetizing Fixture

When looking at state of the art magnetic fixtures from various manufacturers [177, 179], they are usually made of electrical steel. This has several advantages over non-ferrous materials:

- Better heat conductivity
- Higher mechanical strength
- Easier magnetization of deep IPM rotors

The main disadvantages are the eddy effects and the additional magnetization curve of the steel. Using ferrous material for the magnetic fixture in a QCM might be possible, since the same steel is also present around the compensation coil. In this dissertation, the material was chosen to be non-ferrous because of the risk of a predominant eddy and magnetization effects, which would superimpose the field of the magnet. Additionally, steel laminations increase the influence of neighboring magnets.

6 Testing and Analysis

In this chapter, all tests for the motor, the can and the QCM are shown including their test setups. Due to financial limitations, only 6 cans could be tested. The lab PFM and QCM will be presented and several tests including ferrites and REE magnets will be presented.

6.1 Motor Testing

For testing the motor, a new dynamometer setup is built, which is also capable of conducting dynamic performance tests. The setup consists of:

- Siemens 1FT6084-8SK71-1TG0 Load Machine [194]
- REFU RPCS 600 Load Inverter [186]
- Lorenz DR-2212 Torque Transducer [175]
- 3 x Zes Zimmer PSU200 Current Transducers [209]
- Zes Zimmer LMG 670 Power Analyzer [208]
- Labview[®] sbRIO-9642 FPGA Controller [180]

The fixtures for the components are made of AlZnMg plates. The whole setup can be seen in Fig. 6.1. The tests, especially the efficiency tests, are done by an automated testing program controlling both the dynamometer and the power analyzer. This has to be done because of the amount of torques, speeds, lead angles and DC voltages that have to be tested. Additionally, the automatization limits the heating during testing and provides more accurate and repeatable results. The program is written in Labview[®] and executed on the FPGA controller.

For the measurement of the cogging torque, another test bench is setup - including a stiff connection from the motor shaft to the torque sensor and an indexing head (see Fig. 6.2). The indexing head can be rotated at a distinct angle. Considering the clearance inside the head, the measurement only gives good results up to the inflection point. The other flank of the cogging torque has to be measured in the reverse direction.

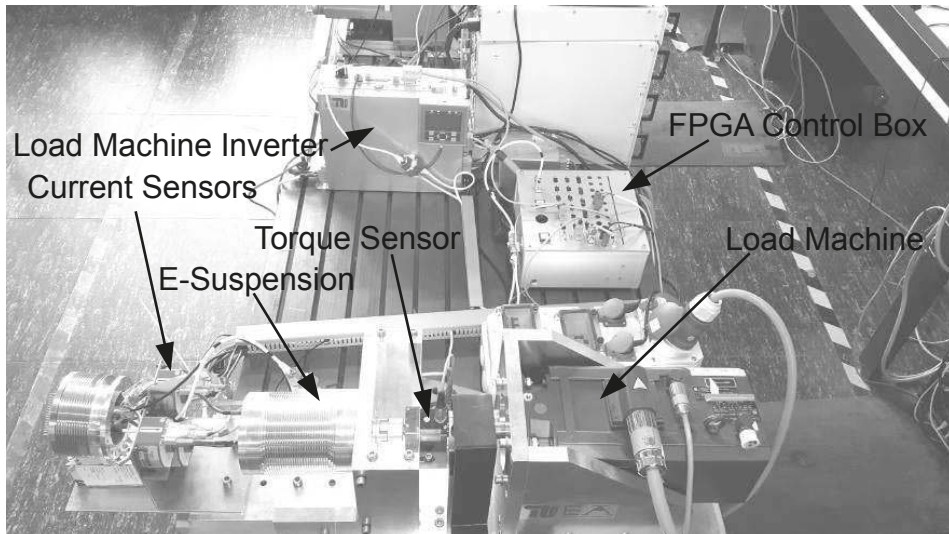


Fig. 6.1: Dynamometer Setup for the E-Suspension drive

6.1.1 Resistance, Inductance and EMF

The average resistance per single tooth at 20 °C is calculated to be 76.3 m Ω . The line to line resistance per phase element is 12.9 m Ω - which is very close to the estimated value of 12.8 m Ω . Since the IPM topology leads to a saliency, the motor inductance will be investigated depending on the rotation angle, also using the indexing head (see Fig. 6.2). A sinusoidal current with 0.67 A at a frequency of 300 Hz is used to measure

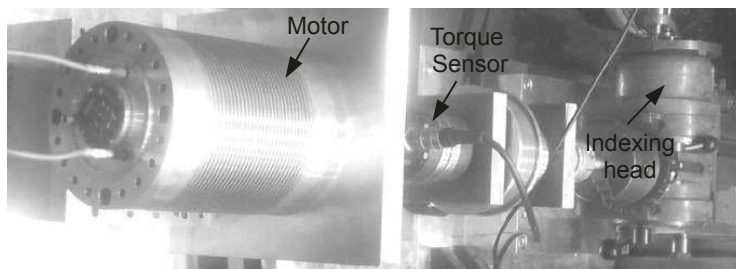


Fig. 6.2: Test bench for cogging torque and d- and q-inductance measurements

the inductance characteristic. Comparing the measured and simulated inductances (see Tab. 6.1), one can see that the simulation overestimates the values by about 7%-9%. The inaccuracy might come from mechanical tolerances of the rotor and stator diameter. In Fig. 6.3, the simulated and measured EMF is shown for 1,000 RPM. The simulation underestimates the induced voltage by about 12% at the peak. This can be explained by lower tolerances of the magnets inside their pockets which reduce the overall air gap, as well as a better general stator inner diameter and rotor outer

Tab. 6.1: Measured and simulated d- and q-inductances at a sinusoidal current of 0.67 A with 300 Hz

	Measured	Simulated
L_d	241 μH	260 μH
L_q	306 μH	334 μH

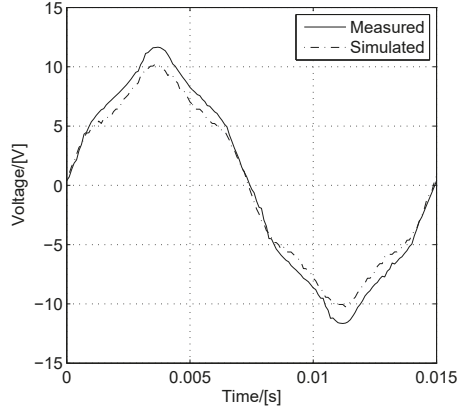


Fig. 6.3: EMF at 1,000 RPM FEA - simulated and measured

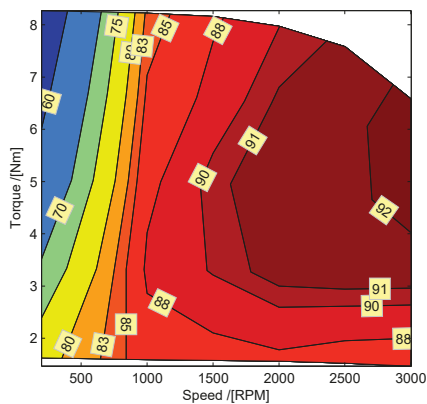
diameter tolerance. Additionally, the remanent flux density B_r of the magnets is bigger when compared to the one used in the simulation $B_{r,\min}$ [202].

6.1.2 Motor Efficiency Measurements

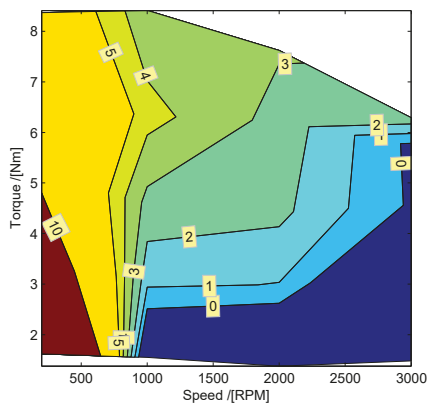
As can be seen in Fig. 6.4, the measured efficiencies agree well with the theoretical ones in Fig. 2.35. At low speeds, the difference is bigger because of measurement tolerances of the torque sensor. At higher speeds, the difference becomes small. The measured total losses are lower compared to the simulations (see Fig. 6.5). This is because of the same reasons mentioned for the induced voltage. For completeness, the efficiency of the whole electric drive is shown in Fig. 6.6. The claim to have more than 75 % efficiency at all working points could not be fulfilled. To reach such high efficiencies, even at speeds lower than 900 RPM, the motor would have had to be much bigger and also heavier. Higher efficiency can be achieved by reducing the copper losses.

6.1.3 Cogging Torque Measurements

The torque sensor (Lorenz DR-2643 [176]) between the indexing head and the motor that should be tested is connected with rotational backlash-free clutches. The measurements have to be done in both directions because of the play inside the indexing head. Both curves are adjusted subsequently to one common curve, which can be seen in Fig. 6.7. The estimated amplitude is higher than the measured one, and also the

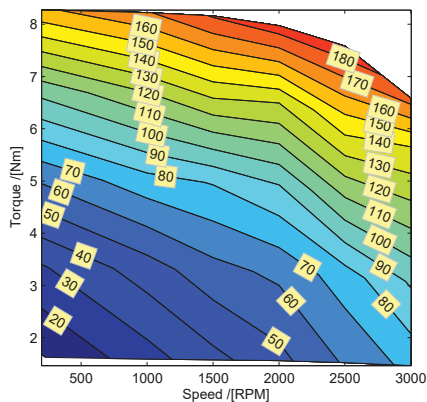


(a) Measured efficiency[24]

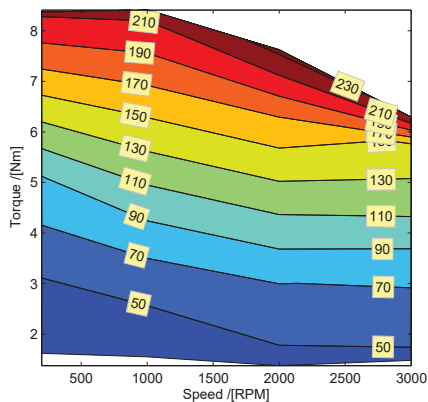


(b) Difference between simulation and measured efficiency

Fig. 6.4: Measured efficiency and the difference between simulation and measured efficiency of the motor in [%] at 38 V DC



(a) Measured



(b) Simulated

Fig. 6.5: Measured and simulated losses of the motor in [W] at 38 V DC

slope differs in between 2.5 deg to 12.5 deg. This could be due to the tolerances of the inner bore of the stator, and also due to different magnet properties.

6.2 Can Test Setup and Analysis

To test the cans a quasi-stator without any electric or magnetic functions is built. This is done because of the huge costs of each real stator prototype. In Fig. 6.8 and 6.9,

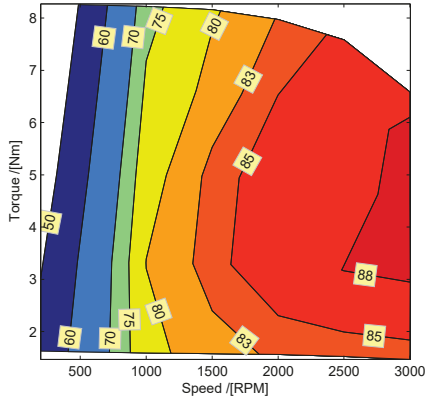


Fig. 6.6: Measured efficiency in [%] of the whole drive at 38 V DC [39]

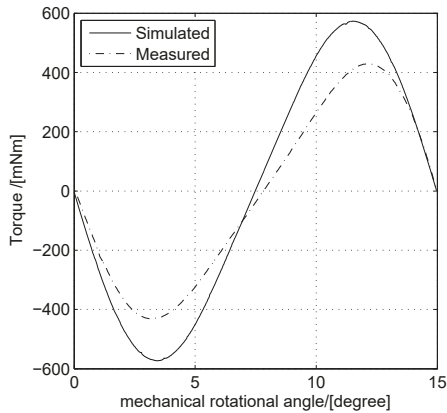


Fig. 6.7: Simulated and measured cogging torque vs. mechanical position of the rotor

the setup is shown. It consists of the equivalent teeth and slot openings where the slot wedges are inserted.

The cans can also be tested without the equivalent teeth (see Fig. 6.9).

The pressure inside the can is measured by a manometer [171] connected to one side of the can. The can is filled with water from the other side, ensuring that no air is left inside it for safety reasons. A high speed camera is installed in front of it (see Fig. 6.10) to detect weepage/trackage.

6.2.1 Can Test Setup without an equivalent Stator

This test is done prior to the test with an equivalent stator since the can has to withstand the whole pressure by itself, and is not stabilized by the equivalent tooth and wedges. A glass fiber and a carbon fiber can are tested for comparability. Later in the

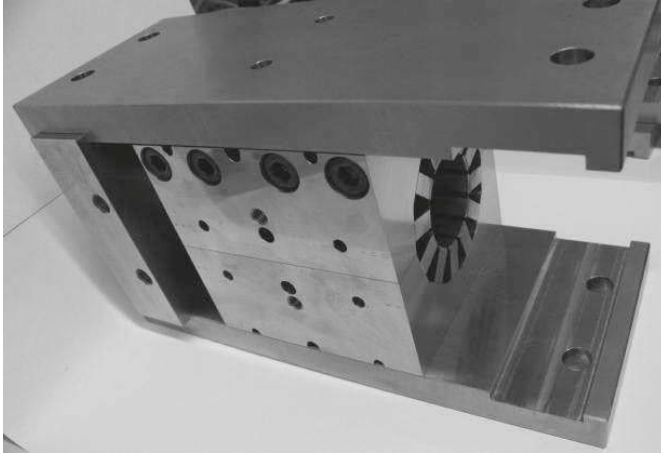


Fig. 6.8: Can test setup side view with an equivalent stator

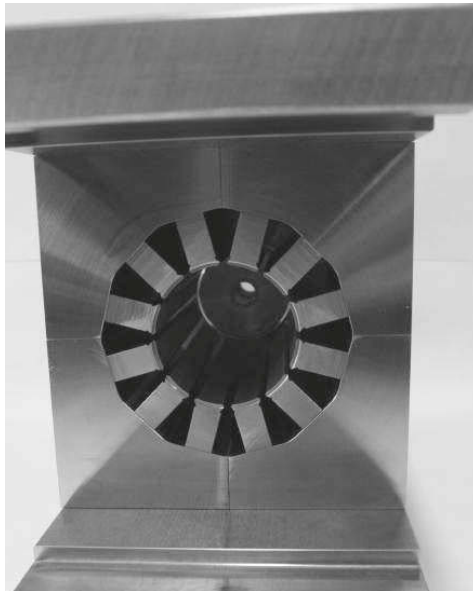


Fig. 6.9: Can test setup front view with an equivalent stator

pump, only glass fiber cans are used because of their electric insulation. For these tests, water is used instead of oil for cleaning reasons. Since water is barely compressible, the pressure pump flow has to be tuned precisely. The pressure is ramped up until any damage or pressure loss is detected. Maximum pressure is 200 bar, which has to be held for at least 5 min. This ensures that weepage can be detected. Pressure losses due to the leakage inside the pump can be avoided by closing the inlet valve when reaching maximum pressure.

The carbon fiber can withstands a pressure of 196 bar [24] for several hours. The glass

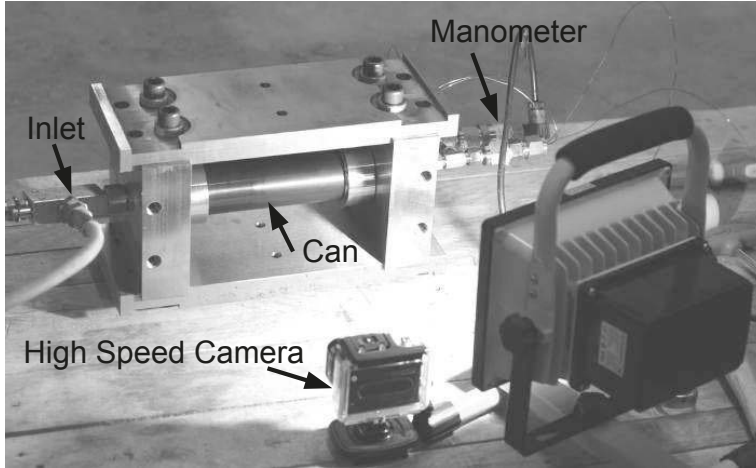


Fig. 6.10: Can pressure setup assembled without quasi stator

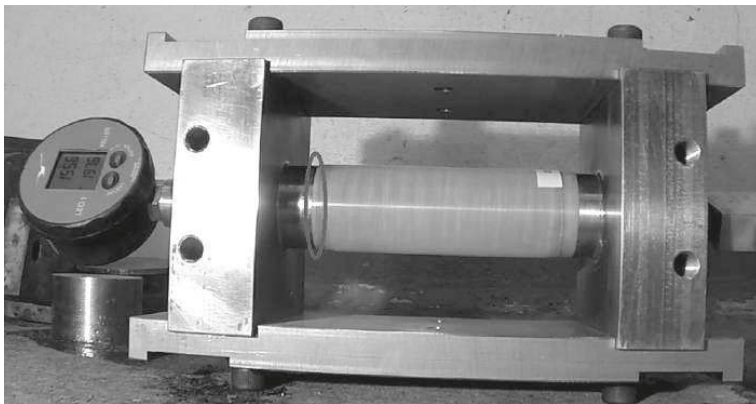


Fig. 6.11: Can testing setup viewed from high speed camera; circled: sealing point

fiber tube cracks at a pressure of 159 bar at the sealing point (see Fig. 6.11, sealing point circled). Both tubes do not show any indication of weepage.

6.2.2 Can Test Setup with an equivalent Stator

The setup with equivalent stator is tested the same way. The carbon fiber tube is not damaged and withstands a pressure of 200 bar for several hours without showing any kind of weepage. The glass fiber tube brakes at 150 bar, again at the sealing point.

6.2.3 Analysis of the pressure Testing

Having just 3 cans each for testing, especially when made out of wound fiber, cannot give a profound answer. Therefore, the results have to be taken academically. All damaged cans broke at the sealing point. When pressurizing the cans, the sealing is pressed against the can wall with static pressure applied from the inlet. Additionally, when increasing the pressure, the sealing is compressed and induces stress into the fiber can in an axial direction. The high pressure leads to an elastic expansion of the can, which increases the tolerated gap between inlet and can as shown in Fig. 6.12 detail F. Because of the purely radial winding of the cans, axial stability is only provided by the epoxy resin, which is very limited.

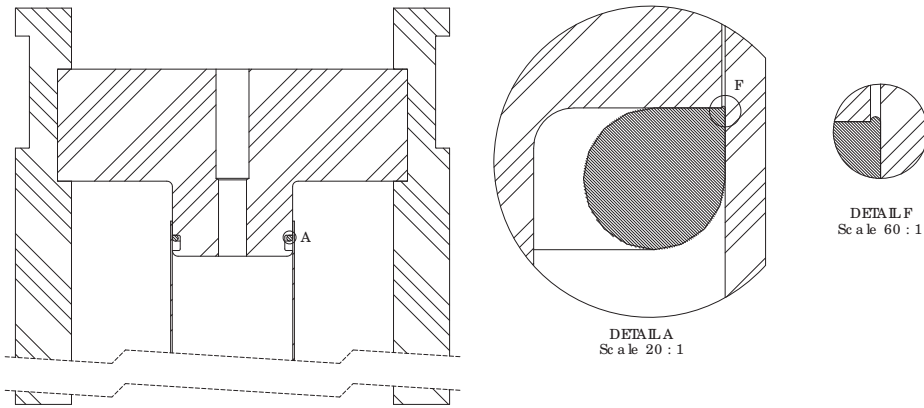


Fig. 6.12: Estimated sealing deformation during pressurization; cut through the inlet (see Fig. 6.10)

To avoid such damage, the can has to be wound with a lower angle, which increases the complexity of the tolerated outer wall. Hence, RTM technique has to be used to achieve a smooth epoxy surface on the outside for good contact ability by the supporting stator.

6.3 Magnetizer Test Setup and Analysis

The signals of the search coils which measure the EMF caused by the fields B_{app} and B_{mag} are in the range of 200 V for NdFeB magnets. After integrating and dividing them by the effective turns and the coil area to get the magnetic flux density, these two signals are subtracted and divided by $1 - N_d$ or $1 - \mathfrak{D}$ as already seen in formula 5.8 and 5.30, respectively. The remaining signal is small and hence it would be better to do the subtraction before the conversion into a digital signal [16, 28, 30, 45, 75, 116]. In Fig. 6.13 the search coil connection is shown. The changing fields generate the EMFs $U_{EMF,app}$, $U_{EMF,mag}$ and $U_{EMF,comp}$. When not inserting any magnetic active part

into the magnetic fixture, both voltages $U_{EMF,app}$ and $U_{EMF,mag}$ should be similar and result into a zero voltage U_M . Unfortunately, because of mechanical tolerances, this signal has to be offset compensated, which is done using the compensation coil (Comp Coil). This compensation coil is wound around the B_{app} coil and with the H-Bridge composed of resistors R_1, R_2, R_4, R_5 and potentiometer R_3 , both positive and negative offsets can be compensated. From the authors experience, this electrical compensation is more reliable than mechanical compensations [103] where an additional coil wound in series to one of the main coils is rotated in the field so that U_M becomes zero in case of the absence of any sample. The load resistances and capacitors $R_{app,load}, R_{M,load}, C_{app,load}, C_{M,load}$ are chosen according to [75]. $L_{app}, R_{app}, L_{mag}, R_{mag}, L_{comp}, R_{comp}$ are the search coils resistors and inductances.

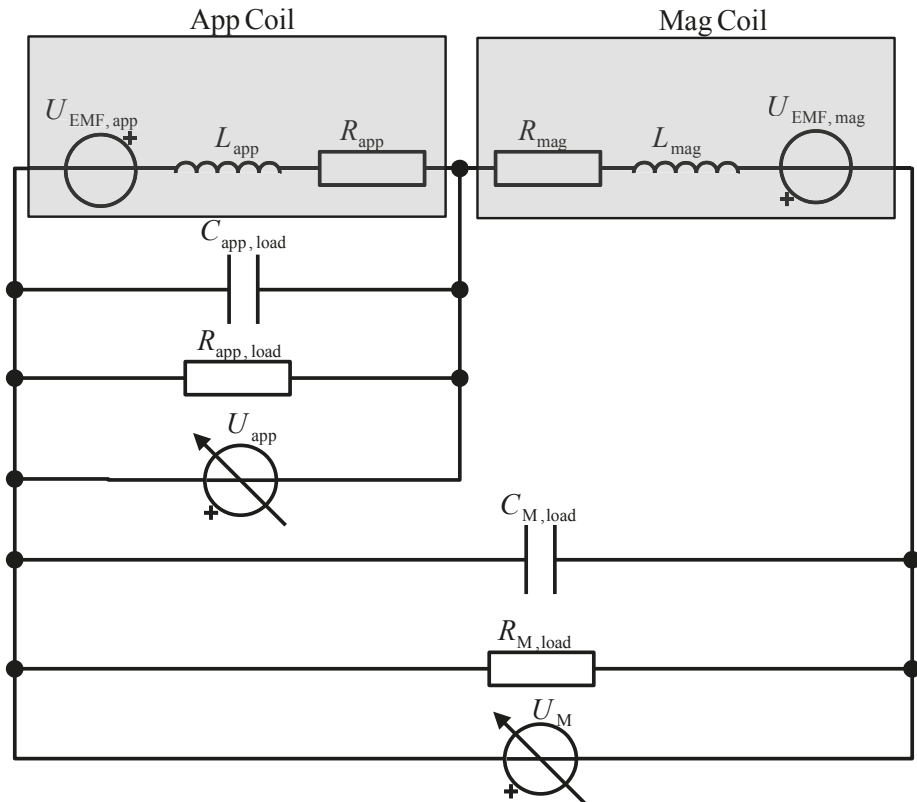


Fig. 6.13: Search coil connection and compensation

For the quality measurements of the magnets, the following measurement equipment was used:

- Yokogawa Transient Recorder DL850 [207]
 - high speed, high resolution modules (720211 isolated Module) for U_{app} and U_{M}
- PEM LFR 30/300 Rogowski coil for load current measurements [183]
- Testec TT-SI 9010 [195] capacitor voltage measurement

6.3.1 Calibration of the Pulse Field Magnetometer

To get an idea, how the QCM could be calibrated, a PFM was built up and several tests were performed:

- Test with a cylindric $\text{Sr}_1\text{Fe}_{12}\text{O}_{19}$ ferrite [189], pre-measured in a permeagraph
- Tests with a copper/aluminum cylinder with a defined electrical conductivity
- Test with a cylindric NdFeB magnet

The PFM is designed according to the sketch shown in Fig. 5.2. In Fig. 6.14, the drawing of the PFM for cylindrical samples is shown. The search coils as well as the probe are mounted on a probe holder, which is screwed in the field coil holder. This makes it possible to calibrate the coils by screwing the probe holder more or less onto the field coil holder, so that the search coils are subject to more or less field. In Fig. 6.15 the test setup is shown.

The cylindric sample probes have a diameter of 6 mm and a height of 5 mm. This standard size is widely available and inexpensive to buy. The reference measurements of the ferrites are done with a permeagraph [178]. This enables the calibration of PFM and later on, the QCM with the same measurement equipment. NdFeB can only be measured with a permeagraph up to a certain field strength because of the saturation inside the yokes. Hence, the calibration measurements can only be performed with low coercive ferrites. Additionally, the $\text{Sr}_1\text{Fe}_{12}\text{O}_{19}$ ferrites have a very low electrical conductivity and do not exhibit big eddy current effects (see section 5.1). The demagnetizing factor for the sample size can be found in [17]:

$$N_{\text{d,cyl}} = 0.345 \tag{6.1}$$

Usually, the search coils are not directly attached to the magnets, in this setup they are 1.5 mm away from the probe - which leads to a decreased field inside the B_{mag} coil. This is usually compensated for by fitting the effective turn area $N \cdot A_{\text{eff}}$ of the coil by

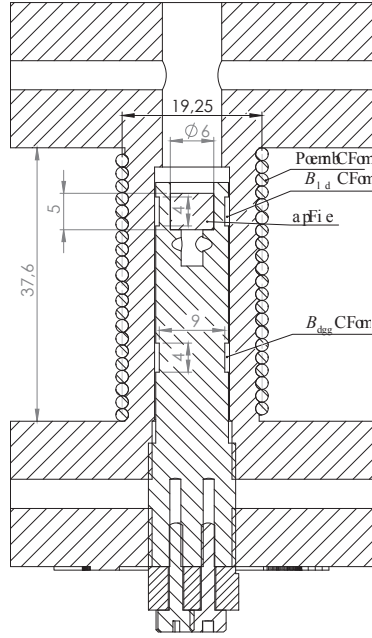


Fig. 6.14: Cut through PFM test coil for cylindric probes

the fitting factor, introduced in section 5.1.2 [164]. Hence, the signals measured by the circuit shown in Fig. 6.13, U_M and U_{app} have to be adapted:

$$J_{\text{mag,appa}}(t) = B_{\text{mag}}(t) - B_{\text{app}}(t) - \mu_0 M_{\text{eddy}}(t) \quad (6.2)$$

$$J_{\text{mag,appa}}(t) = X_{A,\text{fit},J} \int \frac{U_M(t)}{N \cdot A_{\text{field}}} dt \quad (6.3)$$

$$B_{\text{app}}(t) = X_{A,\text{fit},\text{app}} \int \frac{U_{\text{app}}(t)}{N \cdot A_{\text{field}}} dt \quad (6.4)$$

- $J_{\text{mag,appa}}$:= Apparent polarization
- $X_{A,\text{fit},J}$:= Apparent polarization area fitting factor
- $X_{A,\text{fit},\text{app}}$:= Applied field area fitting factor

Equation 6.7 also shows the limits of the search coils. If the magnets are magnetized and then magnetically stressed, the demagnetizing curve will only show the change in magnetization but not the absolute values. Absolute values can be measured e.g. with hall sensors, which was tried in our lab [140]. The problem of induced voltages inside the connecting wires and capacitive coupling effects could not be solved with the used equipment, therefore only search coils together with demagnetized magnets were investigated.

To find out the effective turn area $N \cdot A_{\text{eff}}$, a reference $\text{Sr}_1\text{Fe}_{12}\text{O}_{19}$ 26/24 ferrite [189],

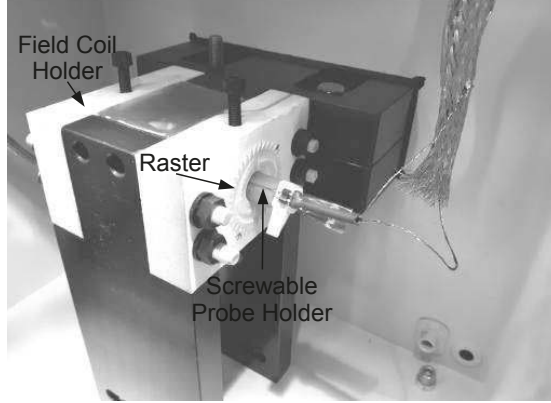


Fig. 6.15: PFM test setup picture

which is demagnetized thermally at 650 °C for 4 h is used. In Fig. 6.16, such a measurement is shown. The effective field area fitting factor is calculated to $X_{A,fit,J} = 3.17$ so that both B_r measured by PFM and permeagraph have the same value. The error

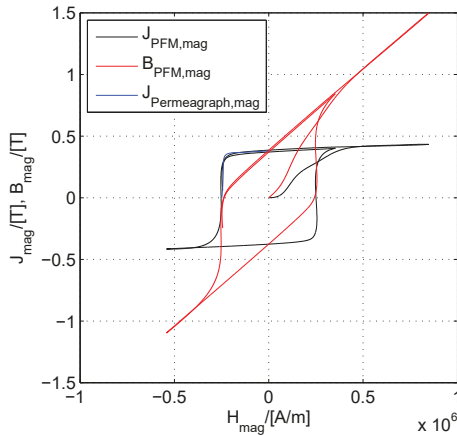


Fig. 6.16: Polarization J_{mag} measured by lab PFM as well by a permeagraph [178] and B_{mag} by lab PFM for a 26/24 Sr₁Fe₁₂O₁₉ ferrite [189]

made by the PFM is low in the B_r region, and rises with increasing H_{mag} . It is interesting to see that with negative increasing H_{mag} the error rises, since the demagnetizing factor becomes a function of the susceptibility (see section 5.1.6). Part of the error also comes from the magnetic viscosity, which will not be discussed in detail. On the other hand, H_{cJ} is predicted very well. In Fig. 6.17 the error $J_{Permeagraph,mag} - J_{PFM,mag}$ is shown. Up to the knee point, the error is below 0.025 T.

To get an idea of how eddy currents will affect the measurements, a copper cylinder with the same size as the ferrite is investigated to calculate the geometry factor c_1

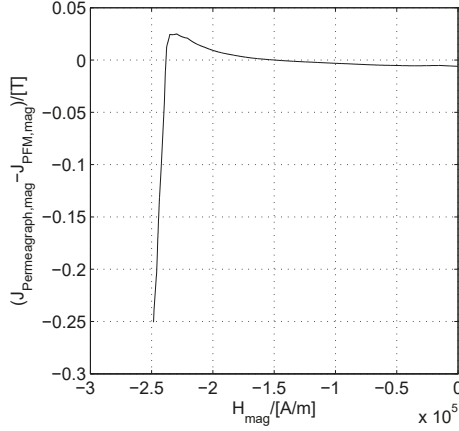


Fig. 6.17: Polarization measurement error between permeagraph and lab PFM; measurements for a 26/24 Sr₁Fe₁₂O₁₉ ferrite [189]

from formula 5.15 for the PFM. In this case, the sample reacts only with eddy currents which can be measured, and so the formula can be rewritten as:

$$c_1 = -\frac{M_{\text{eddy,cyl,z}}(t)}{\kappa_{\text{sample}} \frac{dB_{\text{mag}}(t)}{dt}} \quad (6.5)$$

In Fig. 6.18, $M_{\text{eddy,cyl,z}}(t)$ which is calculated by different methods is shown. First, by measured values using formula 5.8 and 5.9, second by FEA using the same formula, and third by formula 5.15.

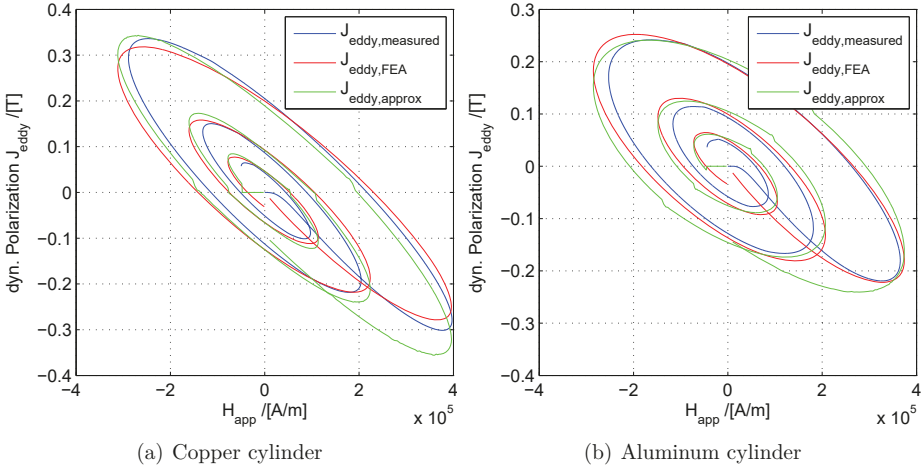


Fig. 6.18: Measured and simulated (FEA) J_{eddy} vs. H_{app} and approximated by formula 5.15 for a copper cylinder

As can be seen, the approximation by formula 5.15 of the dynamic magnetization varies especially at $H_{\text{mag}} = 0$. It should start at the origin, but starts at a negative J_{eddy}

because B_{mag} is a damped sinusoidal oscillation, and therefore the biggest slopes occur at zero crossings. This means that formula 5.15 and also 6.5 cannot be used in the very beginning, i.e. during the first half oscillation. The transient FEA predicts the effect better. Tolerances in the setup reduce the accuracy of the simulation. Still, the approximation seems to be a good way to predict eddy currents, except at the beginning.

With these calibrations, NdFeB magnets can be measured. In Fig. 6.19 the measurements of a nickel coated 263/135 magnet [148] are shown. Looking at the origin of the magnetizing curve, the wrong estimation of the eddy currents in the first half oscillation leads to an offset of J_{mag} and B_{mag} .

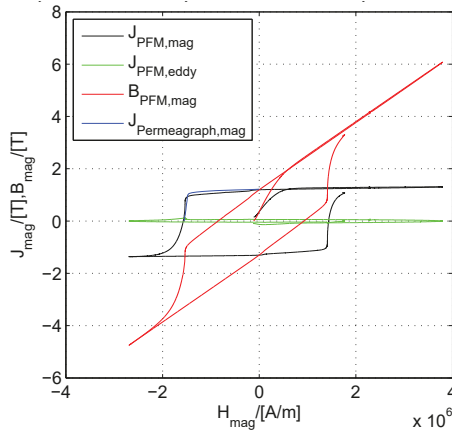


Fig. 6.19: PFM measurement of a NdFeB nickel coated 263/135 magnet [148]; $1/\kappa_{\text{mag}} = 1.54 \times 10^6 \Omega\text{m}$ by method from section 5.1.3

The PFM demagnetizing curve measurements fit well with the permeagraph measurements. Similar to the $\text{Sr}_1\text{Fe}_{12}\text{O}_{19}$ ferrite measurements, the error increases with decreasing H_{mag} . Additionally, there are several dips in the demagnetizing curve, which can be traced back to the nickel coating according to [164]. For the QCM, the magnets are epoxy coated to prevent such a possible behavior.

As can be seen, the demagnetizing curve can be estimated well by the PFM. It can be stated that a reference estimation of the magnetizing curve cannot be done inside the PFM because of the problems discussed before. Other PFM like [164] have a longer pulse period length of 40 ms compared to the investigated one with 0.3 ms. Such a long pulse period length comes along with a lot of heating of the coil, and therefore with a low repetition rate, which is essential when it comes to mass production. In commercial rotor magnetizers, pulse period lengths in the range of our PFM are quite common. Still, for the designed problem, where only the demagnetizing curve should be measured, it is a good solution.

6.4 Calibration of the Quality Control Magnetizer

For these tests, the magnetizing fixture shown in Fig. 6.20 is built up and connected to the magnetizing circuit (see section 5.2.4). The analysis electronics unit is comprised of the circuit shown in Fig. 6.13. This electronics unit measures the voltages of the B_{mag} and B_{app} search coils as already mentioned for the PFM, and adds the constituent signals so that the composite signal $J_{\text{mag,appa}}$ is generated. In case of the presence of a ferromagnetic material with a saturation curve, $J_{\text{mag,appa}}$ can be calculated as:

$$J_{\text{mag,appa}}(t) = B_{\text{mag}}(t) - B_{\text{app}}(t) - \mu_0 M_{\text{eddy}}(t) \quad (6.6)$$

$$J_{\text{mag,appa}}(t) = \mathfrak{X}_{\text{A,fit,J}}(t) \int \frac{U_{\text{M}}(t)}{N \cdot A_{\text{field}}} dt \quad (6.7)$$

$$B_{\text{app}}(t) = \mathfrak{X}_{\text{A,fit,app}}(t) \int \frac{U_{\text{app}}(t)}{N \cdot A_{\text{field}}} dt \quad (6.8)$$

$\mathfrak{X}_{\text{A,fit,J}}$ and $\mathfrak{X}_{\text{A,fit,app}}$ are area fitting functions dependent on the saturation of the steel. These functions are calculated by FEA as the quotient of the intrinsic field measured at the position of the magnet, and the position of the search coils:

$$\mathfrak{X}_{\text{A,fit,J}}(t) = \frac{J_{\text{mag,appa}}(t)}{\underbrace{\int \frac{U_{\text{M}}(t)}{N \cdot A_{\text{field}}} dt}_{J_{\text{mag,appa,coil}}(t)}} \quad (6.9)$$

$$\mathfrak{X}_{\text{A,fit,app}}(t) = \frac{B_{\text{app}}(t)}{\underbrace{\int \frac{U_{\text{app}}(t)}{N \cdot A_{\text{field}}} dt}_{B_{\text{app,coil}}(t)}} \quad (6.10)$$

- $\mathfrak{X}_{\text{A,fit,J}}(t) :=$ Apparent polarization area fitting function in a QCM
- $\mathfrak{X}_{\text{A,fit,app}}(t) :=$ Applied field area fitting function in a QCM
- $J_{\text{mag,appa,coil}}(t) :=$ Apparent polarization measured at the position of the search coils in the QCM
- $B_{\text{app,coil}}(t) :=$ Applied field measured at the position of the coils in the QCM

As shown before, several error sources might affect the measurements, so calibrating the system is of major importance. To calibrate the QCM, the following tests have to be conducted:

- Hysteresis measurements of rotor without magnets
 - repeatability measurements after reinserted rotor
- Eddy current calibration
 - with magnet shape copper ashlars with a non-conductive rotor
 - repeatability measurements after complete reinsertion (rotor/magnets)

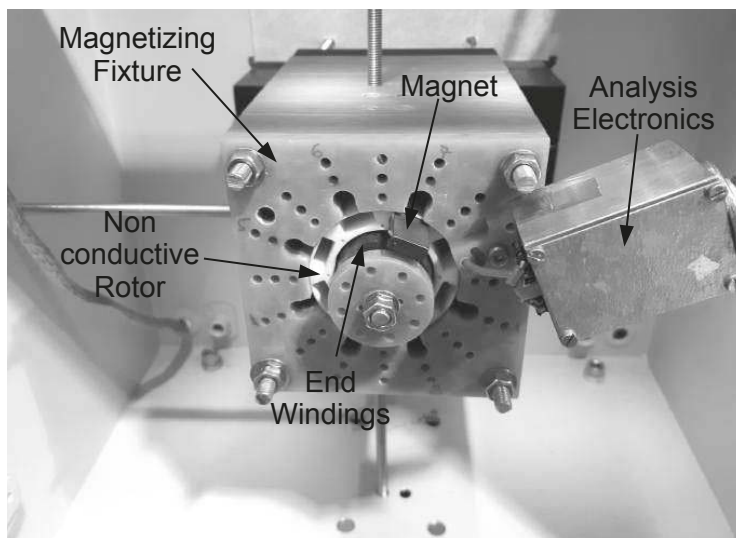


Fig. 6.20: A picture of the magnetizing fixture with a single magnet inserted halfway, and a non-conductive rotor as well as one analysis electronics

6.4.1 Hysteresis Measurements of a Rotor in a Quality Control Magnetizer

For this test, a laminated rotor is inserted into the magnetic fixture without magnets, as well as without a compensating rotor. During testing the M330-35A rotor broke and had to be replaced by an eroded M270-35A rotor. Fig. 6.21(a) shows the measured and the calculated polarization curves of the rotor. The polarization in this case is plotted vs. the applied field. This has to be done, because of the very different saturation levels inside the laminated rotor. Hysteresis effects are not included in the simulation but the core loss effects on the field. Looking at the origin magnified in Fig. 6.21(b), one can see the core loss effects on the field. Measured and simulated curves cross the y- and x-axis at almost the same point, which is an indicator for the right estimation of the core losses. To estimate the error caused by the repeatability, the rotor was inserted into the magnetizing fixture and measured several times without taking it out. To account for any remaining polarization inside the rotor, the idle time between the tests was set to 10 min. The results are shown in Fig. 6.22(a). In a second test, the rotor was taken out and reinserted after 10 min. The results are shown in Fig. 6.22(b). Comparing both figures in Fig. 6.22, one can see that the error increases in the first quadrant, when the rotor is taken out and reinserted into the magnetizing fixture, but stays almost the same in the third quadrant.

Two M270-35A rotors were manufactured. The differences in the hysteresis curves among the rotors can be seen in Fig. 6.23. This error is bigger compared to Fig. 6.22(b).

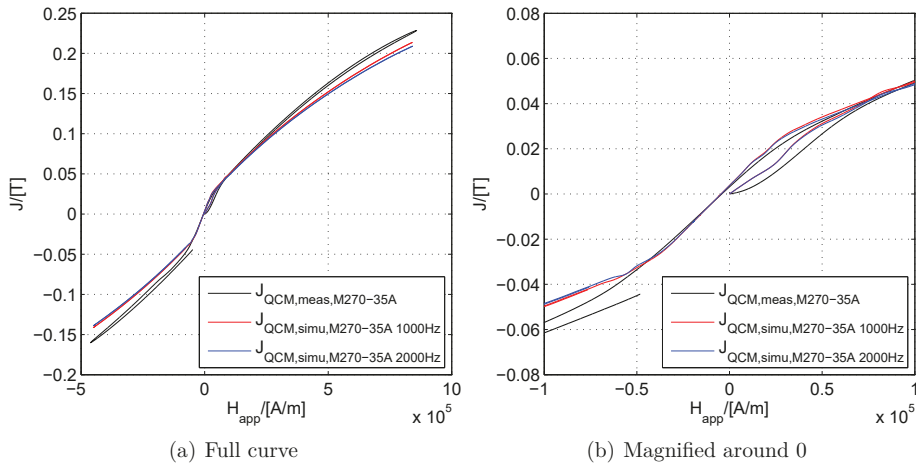


Fig. 6.21: Measured and simulated polarization J of the rotor vs. applied field H_{app} for different magnetization curves of M270-35A; full and magnified around 0

6.4.2 Eddy Current Calibration in a Quality Control Magnetizer

As already conducted for the PFM, one has to estimate the geometry factor from formula 6.5 for rectangular magnets. In the QCM, this can be done with a non-conductive rotor and copper ashlars that have the same size as the real magnets - which are inserted later on. c_2 from formula 5.56 was estimated to be 3.66×10^{-11} compared to $c_1 = 7.32 \times 10^{-12}$ for the PFM. As already mentioned for the PFM, the dynamic polarization cannot be estimated correctly for the first half oscillation. Also, the QCM estimates the dynamic polarization incorrectly as can be seen in Fig. 6.24. The FEA simulation of J_{eddy} is close to the measured values. With copper ashlars and a non-conductive rotor, it is very easy to estimate the repeatability since copper is not subject to permanent polarization. To differentiate between electric and mechanical repeatability, the rotor and copper magnets were measured consecutively (see Fig. 6.25(a)). Then the non-conductive rotor was taken out of the magnetizing fixture and reinserted. The error is shown in Fig. 6.25(b) and is a little bigger compared to the first test.

6.5 Quality Control Magnetization of Ferrites

6.5.1 Magnetization with a non-conductive Rotor

At first, $Sr_1Fe_{12}O_{19}$ HF 28/26 ferrites [190] are tested in a non-conductive rotor, so that repeatability errors coming from the laminated rotor and the magnets can be differentiated. Again, these ferrites were chosen because of their inexpensive availability and an almost constant susceptibility inside the second quadrant until the knee point.

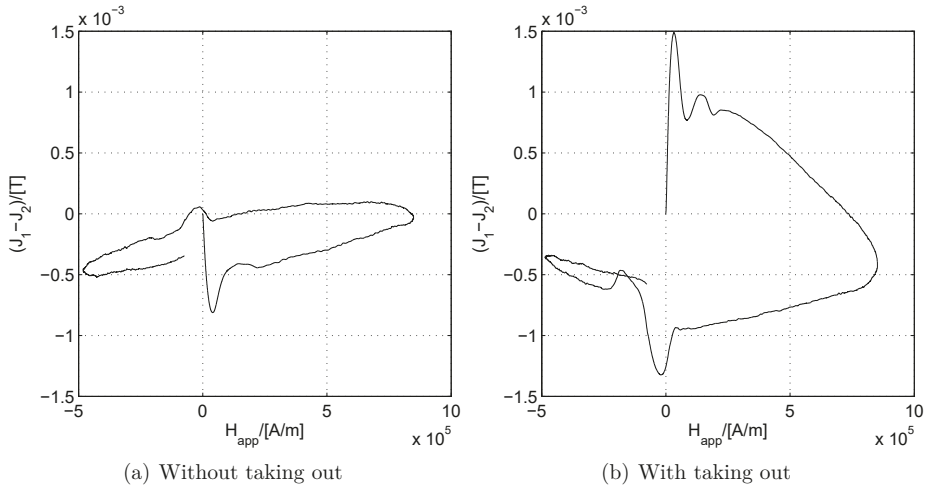


Fig. 6.22: Measured repeatability of a M270-35A rotor with and without taking it out

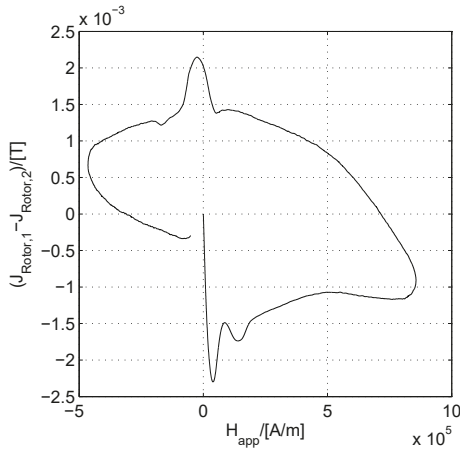


Fig. 6.23: Polarization difference $J_{\text{Rotor},1} - J_{\text{Rotor},2}$ vs. H_{app} among two M270-35A rotors without inserted magnets

They were pre-measured in a permeagraph [178] according to DIN-EN 60404-5 [154]. All ferrites have approximately the same specifications, which can be seen in Tab. 6.2. The demagnetizing factor at almost constant susceptibility for the search coils shown in Fig. 5.6 and 5.8 was calculated by FEA to be:

$$N_{d,\text{QCM}} = 0.614 \quad (6.11)$$

As already mentioned for the PFM, since the coils are not directly wound around the magnets, the effective turn area $N \cdot A_{\text{eff}}$ for the $J_{\text{mag,app}}$ has to be fitted with a field fitting factor $X_{A,\text{fit},J} = 2.113$. The applied field with the factor $X_{A,\text{fit,app}} = 0.87$. For a setup without a steel rotor, this is a constant factor for an almost constant

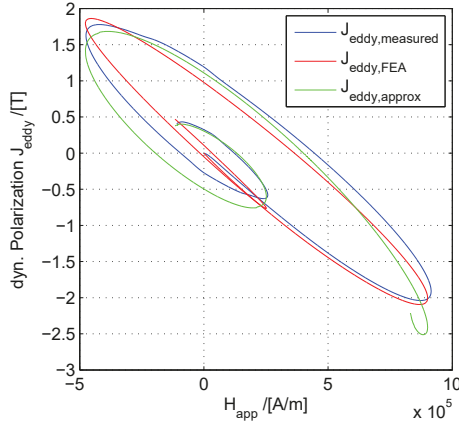


Fig. 6.24: Measured, simulated and approximated dynamic polarization J_{eddy} of the copper "magnets" vs. H_{app}

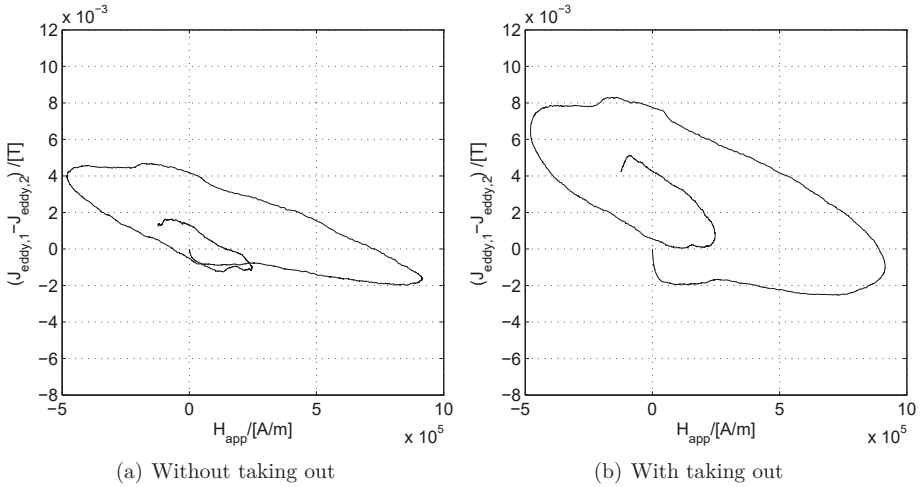


Fig. 6.25: Measured repeatability of J_{eddy} of the copper "magnets" with and without taking out the magnets between measurements

susceptibility. For comparability between permeagraphic and QCM measurements, the magnets were magnetically stressed over H_{cJ} . In Fig. 6.26(a) the measurements can be seen. The magnetizing curve measured with QCM and permeagraph agree well up to 4.5×10^5 A/m, when the poles of the permeagraph start to saturate and the measurement error increases. Due to the chosen constant $N_{\text{d,QCM}}$, the magnetizing curve cannot agree fully. The accuracy of the susceptibility in the second quadrant is also very good. H_{cJ} is achieved at a higher magnetic field, compared to the permeagraph measurement. The FEA simulation is very close to the measurements, but shows a bigger H_{cJ} . The simulated remanent flux density is at about 0.399 T compared to the QCM measurement of 0.406 T and the permeagraph measurement of 0.405 T. For mass

Tab. 6.2: Permeagraph measurements of used $\text{Sr}_1\text{Fe}_{12}\text{O}_{19}$ HF 28/26 magnets

Magnet Number	B_r /[T]	H_{cB} /[kA/m]	H_{cJ} /[kA/m]	BH_{\max} /[kJ/m ³]
1	0.401	281	286	31
2	0.405	280	284	31
3	0.393	283	290	30
4	0.405	277	282	31
5	0.402	282	287	31
6	0.401	284	289	31
7	0.402	281	286	31
8	0.401	282	287	31

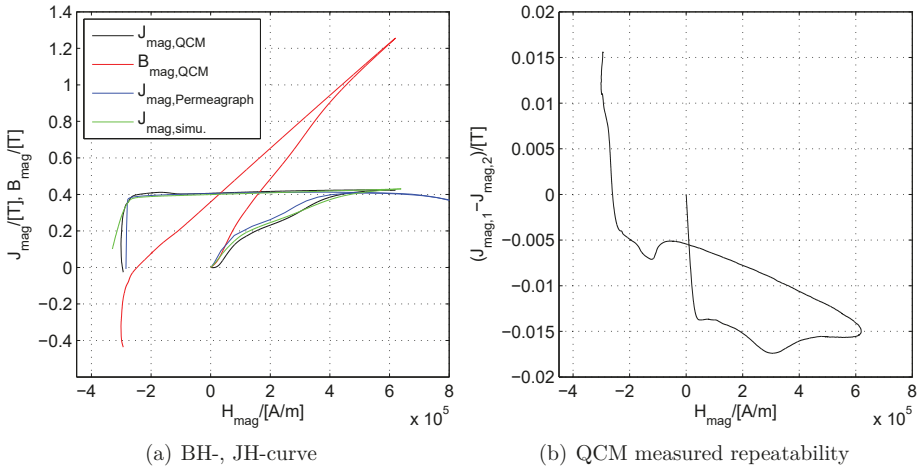


Fig. 6.26: J_{mag} measured by QCM as well as a permeagraph [178] and FEA of $\text{Sr}_1\text{Fe}_{12}\text{O}_{19}$ HF 28/26 ferrites [190] in a non conducting rotor as well as the repeatability error $J_{\text{mag,1}} - J_{\text{mag,2}}$

production, the repeatability is more important, since the measured values correspond to an OK magnet which can be declared as a reference. Therefore, the ferrites were magnetized, taken out, heated up to 650 °C and then reinserted into the non-conductive rotor. The difference between the polarization measurements are shown in Fig. 6.26(b). At B_r , the difference is below 0.006 T. H_{cJ} varies by 12×10^3 A/m, which is not much compared to the coercive field of 2.845×10^5 A/m.

6.5.2 Magnetization with a laminated Steel Rotor

For the second test, the rotor measured for its hysteresis in section 6.4.1 is equipped with the same ferrites from the last section. In Fig. 6.27 the BH- and JH-curve of the magnets in a M270-35A rotor (see Fig. 6.21) as well as the repeatability error $J_{mag,1} - J_{mag,2}$ are shown. B_r measured by the QCM is estimated to be 0.401 T compared to the permeagraph measurement of 0.405 T. Starting from B_r , the demagnetizing curves oscillate, which is repeatable. H_{cJ} is estimated to be 3.129×10^5 A/m compared to the permeagraph measurement of 2.845×10^5 A/m. The simulation shows a remanent flux density of 0.389 T and a coercive field strength of 3.22×10^5 A/m.

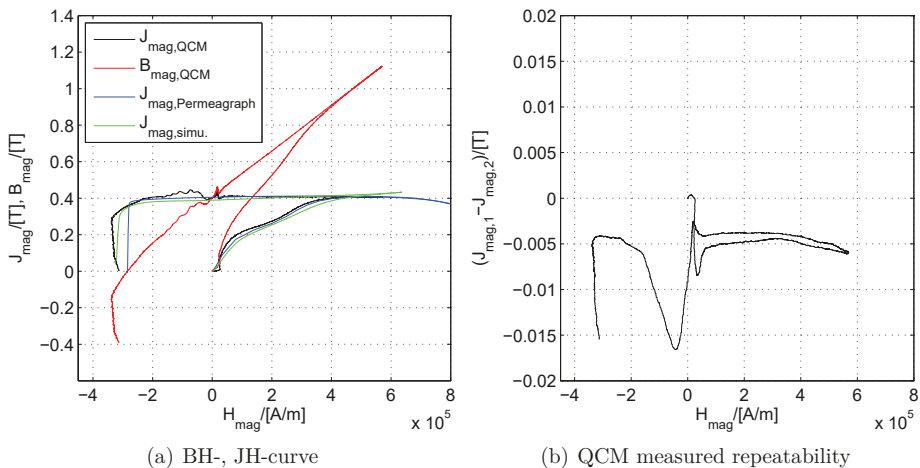


Fig. 6.27: J_{mag} measured by QCM as well by a permeagraph [178] and FEA of $Sr_1Fe_{12}O_{19}$ HF 28/26 ferrites [190] in a M270-35A rotor as well as the repeatability error $J_{mag,1} - J_{mag,2}$

6.5.3 Magnetization with a different Rotor

Since the quality of the rotor might vary as can be seen in Fig. 6.23, it is important to know how this quality difference will affect the magnetic measurements. According to the theory presented in section 5.2.14, small variations should not influence the measurement. For this test, the rotors compared in Fig. 6.23 were equipped with the

same magnets. The differences are shown in Fig. 6.28, and are in the same range as for the repeatability of the non-conductive variation presented in Fig. 6.26.

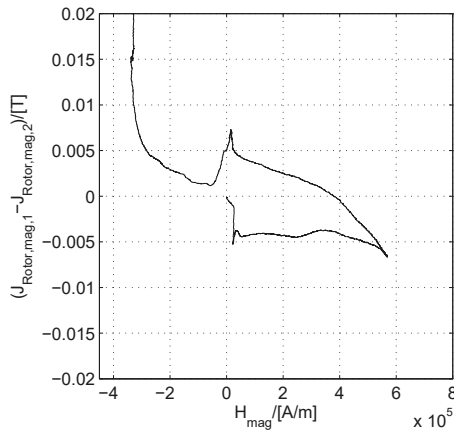


Fig. 6.28: Polarization difference $J_{\text{Rotor,mag},1} - J_{\text{Rotor,mag},2}$ vs. H_{mag} for identical magnets inserted in two different M270-35A rotors

6.5.4 Missing Magnet

To test the neighboring effect described in section 5.2.12, one rotor was equipped with seven magnets leaving the first pocket empty. According to Tab. 5.5, the search coils for magnet one should still measure a small amount of field because of the influence of the neighboring magnets. In Fig. 6.29 B_{mag} , as well as J_{mag} are shown for the search coils corresponding to the empty pocket. The measured B_r is below 0.004 T, which is in the range of the repeatability. The simulation shows a remanent flux density of 0.001 T. Looking at the magnet next to the empty pocket, B_r will be lower compared to the measurement obtained by the permeagraph. In Fig. 6.30, the BH- and JH-curve of the magnet measured next to the empty pocket is shown. B_r is estimated to be 0.368 T, compared to the permeagraph measurement of 0.405 T. The coercive field strength stays about the same. The simulation estimates the remanent flux density to be 0.350 T, and also shows a similar coercive field strength as measured with the QCM.

6.6 Quality Control Magnetization of NdFeB Magnets

Unfortunately, this measurement could not be performed with the coil shown in Fig. 6.20, because of manufacturing errors. The end windings covered by black epoxy were not reinforced by a fiber sleeve, so the necessary magnetizing current of 30 kA for NdFeB magnets might have caused mechanical destruction of the coil. Due to the lack of time, an additional coil could not be fabricated.

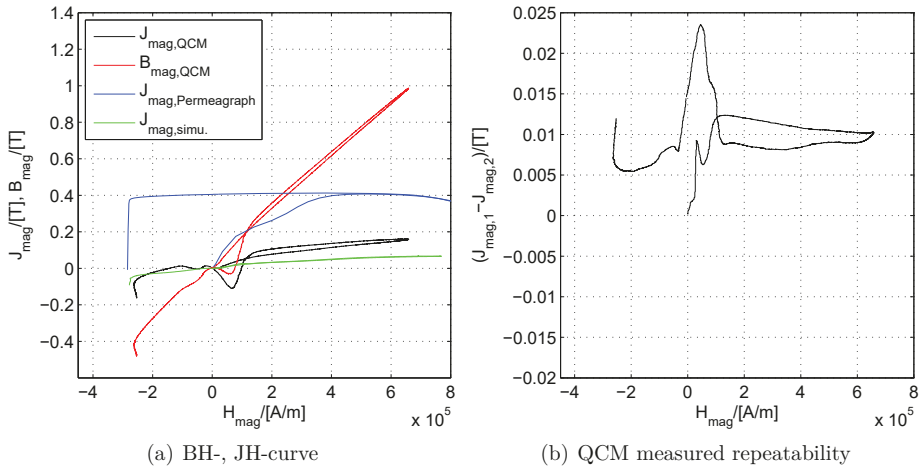


Fig. 6.29: J_{mag} for a missing magnet measured by a QCM and by FEA in a M270-35A rotor as well as the repeatability error $J_{\text{mag},1} - J_{\text{mag},2}$

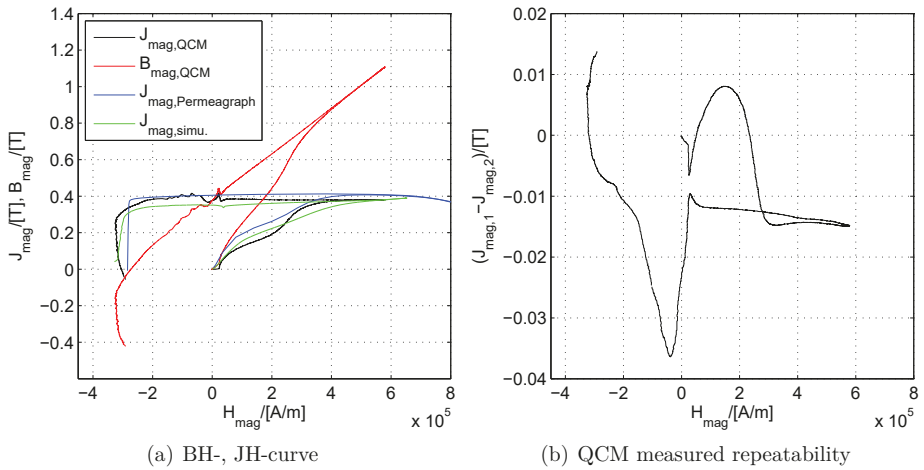


Fig. 6.30: B_{mag} , J_{mag} for the magnet next to the empty pocket measured by a QCM in a M270-35A rotor as well as the repeatability error $J_{\text{mag},1} - J_{\text{mag},2}$

7 Conclusion and Discussion

First, in this section, conclusions from the manufacturing process and the measurements of the Electric Suspension System are drawn. Second, detailed thermal investigations were conducted and wound fiber cans were tested. Both investigations have the objective to decrease the temperature inside the motor, hence decreasing the temperature inside the rotor, and using the magnet flux more effectively. Third, conclusions and limits of thermal optimizations are illustrated. Several sensitivity analyses are presented with the objective to find compatible insulation materials. The consequences of conductive cans in terms of heating and torque reduction are presented and discussed as well.

To be more independent from magnet material price shocks, a Quality Control Magnetizer was introduced in the last sections. In this section, the limits in terms of eddy compensation, EMI and manufacturability are illustrated. Errors are discussed and improvements are proposed.

7.1 Electric Suspension System

The ESS was chosen for this project as an example drive because of the difficult specifications, ability for mass production and direct specifications of an automotive company. During production several difficulties, which have direct influence on the design were detected. The stator teeth are long and thin which has a big impact on the mechanical tolerances. Since the used rotor steel M330-35A has a thickness tolerance of $\pm 8\%$ [4, 196], the worst case scenario for the lamination sheet is a complete skewed slab with a thickness of 0.378 mm on one side, and 0.322 mm on the other side, which results in a curved tooth. This can be partially compensated, when rotating the stamping tool by 180 degree since the next sheet will show similar tolerances, but vice versa. The parallelism of the tooth is assured by the winding fixture, and later fixed by the windings. When using lasered backing lacquer laminations for prototypes, the backing fixture assures the parallelism of the tooth, which means that the backing lacquer serves as an equalizing layer besides gluing, which could result in lower bonding strength. The longer the tooth, the more difficult the parallelism, which in turn becomes very important when forming the stator out of the twelve teeth. Additionally, there is a higher risk of having one sheet sticking out and potentially harming the can with a long tooth. Bigger tolerances of the tooth also deteriorate the shrinking into the housing. Having a smaller diameter compared to the length has the advantage that torque adaptations can be performed easily by changing the tooth length, without changing the whole production line. In times of fast changing sales volume, such an adaptation is very helpful. In this case stamping tools as well as linear winding machines only need small

setup changes. Because of the tolerances of the stator inner diameter, the cans have to be designed to hold against the whole pressure which makes them thicker than necessary. However, thicker cans result in a larger magnetic air gap, bigger magnetic leakage flux and therefore lower efficiency. Also, the additional reluctance torque which is proportional to $L_q - L_d$ becomes smaller. Avoiding any cans and filling the complete motor with the working fluid results in very large wall thicknesses of the housing and end shields, since the force increases linear, with diameter - while keeping the pressure constant. This increases the weight of the motor.

Winding a tooth with a length of $L_{stk} = 120$ mm and a tooth width of just $TWS = 5$ mm tooth width with a 1.6 mm wire results in a big belly as shown in section 3.2. This can be partially avoided by shaping the end caps with a larger winding radius as compared to the one used for this design (2 mm). Filar winding, e.g. with two parallel 1.13 mm wires, improves the belly behavior but reduces the fill factor S_{fg} and increases the complexity. Pressing the wires and heating them by electric current can be done very quickly (7 s for the prototype) and is also easy to integrate into a production line. Using normal wire without backing lacquer already results in an adequate reduction of the winding belly. The backing lacquer increases the stability against mechanical loads, like vibrations, and improves the thermal behavior.

Besides forming the windings by pressing while heating, another method, the hot wire winding technology, could be used. The winding wire is therefore heated up during winding and wound hot around the cold tooth [125]. Because of the temperature difference, the windings shrink causing additional axial forces inside the copper wire, which cause a smaller belly. Additionally, the copper wire adapts slightly better to the bobbin when wound hot.

Using an IPM rotor already includes a centrifugal force protection which would otherwise require an additional fiber bandage. Other advantages like the additional reluctance torque can only be used if the air gap stays small, otherwise L_q and L_d would level each other. Decreasing the can thickness by improving the tolerances of the inner stator diameter and improving the packetization will lead to a decreased magnetic air gap. Due to the larger ratio of reluctance to non-salient torque, the motor will also show better field weakening performance. Having a smaller air gap also results in a lower height of the magnets, which saves material.

The used rotor topology gives the best output performance compared to the investigated magnet material when inner and outer magnetization coils are chosen. When using just single sided magnetization coils, the concentrated rotor topology (see Fig. 2.12(c)) can be designed such that the field during magnetization penetrates the magnet to some degree along the easy magnetization axis, which gives the best output performance. For this application, a concentrated topology would have resulted in bigger inertia of the rotor, which was counterproductive for the dynamic performance specifications.

Besides all the advantages of a long stator in terms of building set for various applications, the mechanical tolerances increase the complexity of the system and produce higher amounts of defective goods. Hence, in a second design iteration of the ESS, the main dimensions should be modified if possible.

7.2 Maximum flux Utilization and metallic Cans

Minimizing stray fluxes leads to better usage of the given magnet material. Using a metallic instead of a non-conducting fiber can made out of a nickel alloy 2.4610 with an electrical conductivity of $\kappa_{2.4610} = 0.76 \times 10^6 \text{ 1}/\Omega\text{m}$ [165], would increase the total losses by about 15 % at 100 A peak and 1,000 RPM (see Tab. 7.1). The additional 32.9 W

Tab. 7.1: Comparison of simulated losses with and without, can made out of a 2.4610 material at 1,000 RPM

	Peak Current/[A]	Torque /[Nm]	Copper Losses/[W]	Iron Losses/[W]	Magnet Losses/[W]	Can Losses/[W]
Can	100	8.34	181.7	27.5	15.6	25.4
No Can	100	8.41	181.7	27.0	8	0

would probably lead to a temperature increase of the working fluid, which leads to an increase in magnet temperature. At higher speeds, 100 A peak and 3,000 RPM, the can losses become even more severe (see Tab. 7.2). At this working point, the extra losses

Tab. 7.2: Comparison of simulated losses with and without can made out of 2.4610 material at 3,000 RPM

	Peak Current/[A]	Torque /[Nm]	Copper Losses/[W]	Iron Losses/[W]	Magnet Losses/[W]	Can Losses/[W]
Can	100	6.03	163.5	39.3	53.1	128.3
No Can	100	6.29	164.5	38.4	25.7	0

increase by 68.7 %. It is interesting to notice that the magnet losses double also when introducing the can. The nickel alloy used for this simulation is very expensive, but has a low conductivity. Using a cheaper stainless steel, e.g. 1.4571 with a conductivity of $\kappa_{1.4571} = 1.33 \times 10^6 \text{ 1}/\Omega\text{m}$ [153], leads to almost doubled can losses shown in Tab. 7.3, as compared to the nickel alloy 2.4610. The can losses become dominant, and the torque decreases by 7 % due to the field weakening effect of the eddy current the torque decreases. Because of the various reasons discussed before, non-conductive cans are a

Tab. 7.3: Comparison of simulated losses with and without, can made out of 1.4571 material at 3,000 RPM

	Peak Current/[A]	Torque /[Nm]	Copper Losses/[W]	Iron Losses/[W]	Magnet Losses/[W]	Can Losses/[W]
Can	100	5.85	164	38.6	51	215.3
No Can	100	6.29	164.5	38.4	25.7	0

good choice for highly efficient pressurized drives. Future tests with several glass fiber cans will have to show if problems like sealing cracks can be solved.

7.3 Sensitivity Analysis for different Insulation Material Combinations

Due to the good match between the simulation and the measurements for the thermal model (see section 3), several sensitivity analyses can be conducted. Some combinations of insulation materials with different thermal conductivities are not effective. Looking at Fig. 7.1, one can see that an increase in thermal conductivity of the epoxy leads to a quasi-saturation. For the investigated geometry, it can be stated from experience that a larger conductivity above 1 W/mK for the epoxy might even result in larger temperatures since the epoxy will not penetrate all wire gaps. Even for the investigated epoxy with a conductivity of about 0.9 W/mK and a viscosity of 6 Pa s - 10 Pa s at 25 °C, the gap between the first layer and the liner is sometimes not fully filled, even under vacuum. Another analysis can be conducted by comparing differ-

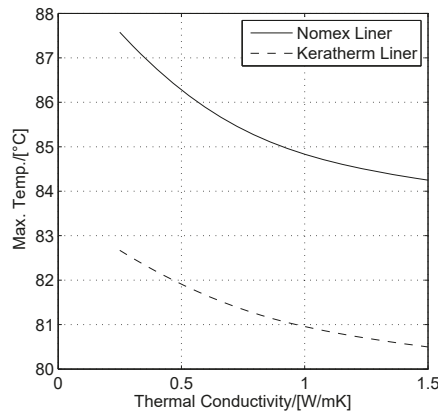


Fig. 7.1: Simulation of thermal conductivity of epoxy vs. max. temperature and different liners for a K.E.G2.Y and N.E.G2.Y (see Tab. 3.2 for abbreviation explanation) configuration

ent hypothetical thermal conductivities of the wire insulation material varying from 0.28 W/mK up to 1 W/mK. The combined thermal conductivity k_3 can be calculated to 2.45 W/mK to 8.36 W/mK using formula 3.13. As can be seen in Fig. 7.2 the wire insulation material conductivity, leads to a quasi-saturation. This can also be seen for the Keratherm[®] liner curve, where the quasi-saturation occurs at higher conductivities. Looking at Fig. 7.3 one can see the dependency of the thermal conductivity of the epoxy vs. the thermal conductivity of the wire insulation vs. maximum temperature for a Nomex[®] or Keratherm[®] insulation material, respectively. For a normal class 155 or 200 wire insulation with a conductivity of 0.27 W/mK to 0.28 W/mK epoxies with a conductivity larger than 1 W/mK result in a small drop in temperature. The higher the conductivity of the wire insulation, the higher the epoxy conductivity, should be chosen. Probably one of the most important plots is Fig. 7.4. For a fixed class 200 wire insulation material with a thermal conductivity of 0.28 W/mK, the dependency of thermal conductivity of the epoxy vs. thermal conductivity of the liner vs. maximum temperature is shown. As can be seen, a temperature drop can be achieved

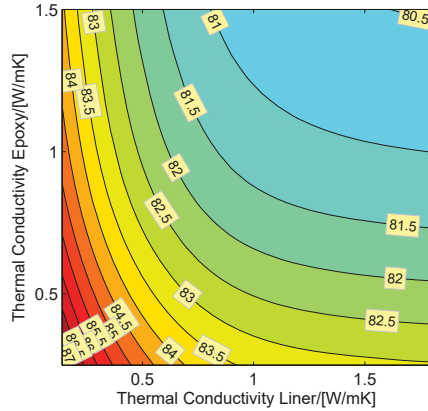


Fig. 7.4: Simulation of thermal conductivity of liner vs. thermal conductivity of epoxy vs. max temperature for a standard class 200 wire insulation

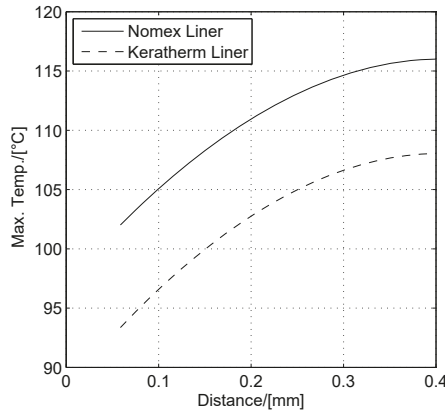


Fig. 7.5: Distance between liner and first winding layer vs. max. winding temperature

stated that optimizing just one material for better heat conductivity can sometimes result in even higher temperatures. Therefore, for every motor design, these thermal investigations should be conducted to find the most suitable insulation combination. These investigations should also include the fin to ambient resistance.

Before starting to conduct deep thermal analysis a winding test should be conducted to improve the thermal model in terms of winding air gaps. The better the heat can be removed from the stator the smaller the drive can be built resulting in lower magnet material usage.

To use even less magnet material, one also has to reduce the losses. Predominant losses are copper losses, which cannot be decreased much with the technology used. Hair pin winding [70], where the wires are formed before winding them to fit into the winding window, reduce the amount of air thereby increasing the fill factor. The wave winding technology [63, 71] is also another approach.

7.4 Magnetization and Quality Control

In section 4 the design for magnetization is explained. Double sided magnetization windings for the rotor allow a homogeneous field, which is useful for the quality control procedure, and even for the maximum usage of the given material. The arrangement of the coil allows for full saturation for NdFeB magnets which could not be tested because of production errors. The quality of the magnets can be estimated well, even though the coercive field is not measured correctly. Due to the false prediction of the hysteresis loop of the rotor steel (see Fig. 6.21), several dents inside the demagnetizing curve can be seen. To analyze this a new measurement quantity, the apparent QCM polarization $J_{\text{mag,appa,QCM}}$, is introduced:

$$J_{\text{mag,appa,QCM}} = \int \frac{U_M(t)}{N \cdot A_{\text{field}}} dt \quad (7.1)$$

$J_{\text{mag,appa,QCM}}$ is free of any area fitting function or demagnetizing functions. This makes it possible to differentiate between the wrong prediction of the \mathfrak{D} -function, $\mathfrak{X}_{\text{A,fit,J}}$ -function and measurement/simulation differences. $J_{\text{mag,appa,QCM}}$ is generated by integrating the U_M voltage shown in Fig. 6.13. In Fig. 7.6, the $J_{\text{mag,QCM}}$ vs. H_{app} and the $J_{\text{mag,appa,QCM}}$ vs. time curves with markings are shown. Looking at the magnetization curve until 1.26×10^{-4} s, one can see that the simulation reaches higher $J_{\text{mag,appa,QCM}}$ than the measured values. This can be traced back to the different saturation levels of the rotor steel, which were shown in Fig. 6.21. In the demagnetizing curve from point P1 to P2, the bridges of the rotor (see Fig. 2.13) start to de-saturate because of the decaying applied field. Here, small differences can also be seen when comparing simulation and measurements. From P2 to P3 the bridges start again to be influenced by the rising negative applied field. The small differences between the measured and the applied curve also affect the J_{mag} curve shown in Fig. 7.6(b). This is because the corresponding \mathfrak{D} -function, shown in Fig. 7.7(a), is calculated using the simulated values which are also used to plot the $J_{\text{mag,QCM}}$ curve. Redoing the test to get the J-H-curve as shown in Fig. 7.7(b) reveals that the oscillations are not randomly distributed, so the difference can be traced clearly to a false prediction of the \mathfrak{D} -function. Later in production, the measured curve will be fitted into a reference permeagraph measurement, so that different magnets can be drawn on a correct J-H-curve basis. In Fig. 7.7(a) the corresponding \mathfrak{D} -function is shown. The dips in the \mathfrak{D} -function originate from the saturation of the rotor steel which guides a large portion of the magnet flux through the thin bridges in case no stator is available (see Fig. 7.8). This becomes even more important when looking at the $\mathfrak{X}_{\text{A,fit,J}}$ -function shown in Fig. 7.9. This function, as introduced in section 5.2.6, links the flux leaving the magnet and arriving at the search coils. When the current becomes close to zero, the bridges are not saturated as much anymore by the applied field, so that more flux coming from the magnet is guided through them. This results in a maximum marked with P2 in Fig. 7.9. This maximum is heavily dependent on the saturation curve inside the bridges, which might be influenced not only by the quality of the lamination, but also by the cutting and packetization of the rotor [50]. Hence, this might be a common error in the prediction of the correct demagnetizing curve from point P2 to P3. For these tests the eroded M270-35A rotor was used to minimize the effect of cutting [50].

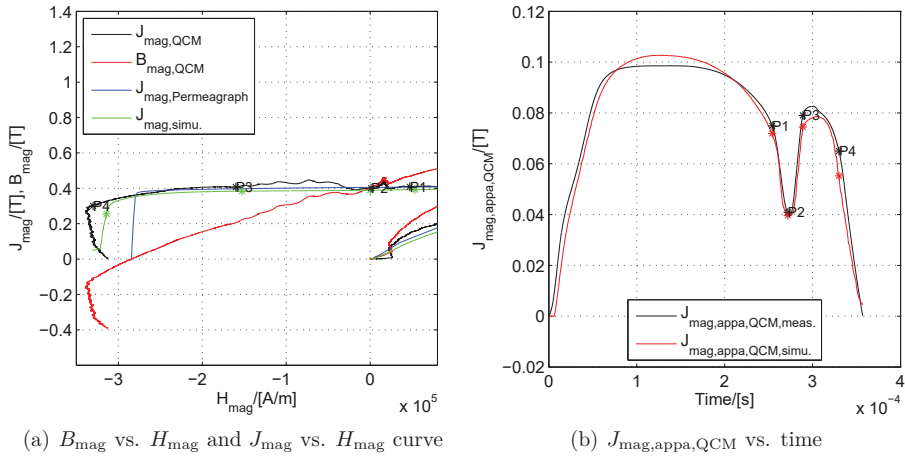


Fig. 7.6: Points of interest at the J_{mag} vs. H_{mag} and $J_{\text{mag,appa,QCM}}$ vs. time

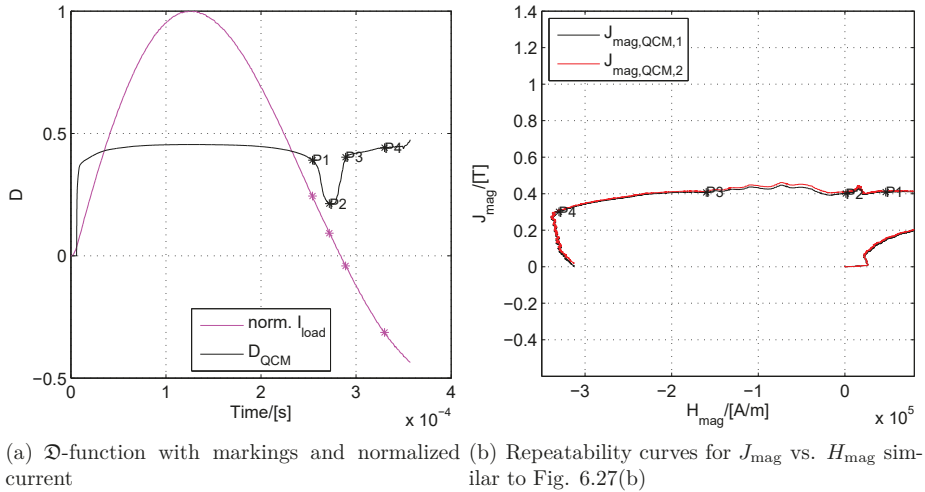


Fig. 7.7: Points of interest at the \mathfrak{D} -function vs. time and repeatability curves for J_{mag} vs. H_{mag}

Looking at the magnetic flux lines of a simple steel fixture (see Fig. 7.10), one can see that most of the flux is guided through the search coil in case of no applied field. In this case, the $\mathfrak{X}_{A,\text{fit},J}$ -function also becomes smaller - which might decrease the problem of the rotor steel bridge quality. As shown in Fig. 7.6, the coercive field strength H_{cJ} is not predicted correctly. Also the simulation overestimates H_{cJ} . It is still not clear where this originates from exactly. Since this is also repeatable, it can be stated that the magnetic field $H_{\text{mag,QCM}}$ is not predicted correctly. Looking back at formula 5.32 and neglecting eddy effects,

$$H_{\text{mag,QCM}} = H_{\text{air,QCM}} - \mathfrak{D} \cdot M_{\text{mag}} \quad (7.2)$$

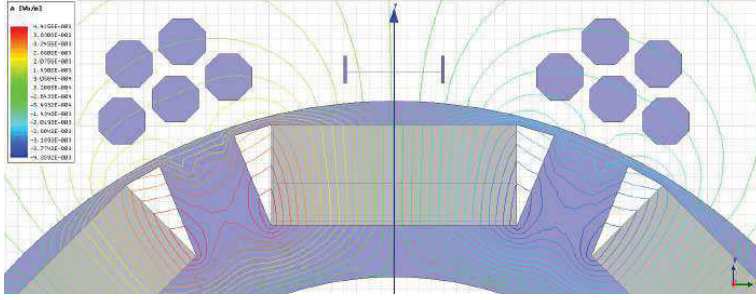


Fig. 7.8: Field for 0 A for a non-ferrous magnetizing fixture with magnetized magnets

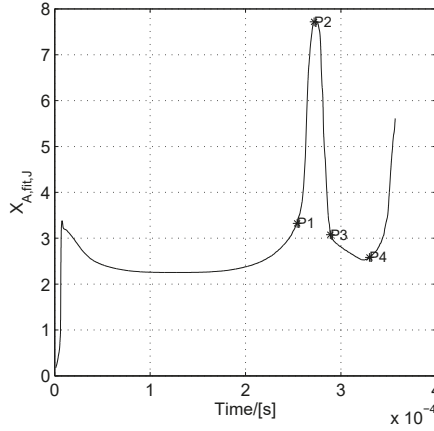


Fig. 7.9: $\tilde{x}_{A,fit,J}$ -function vs. time

it can be seen that there are three error sources for $H_{mag,QCM}$. First, the applied field which is measured by the current and fitted for the applied field at the position of the magnet. This field is also used for the calculation with a non-conductive rotor shown in Fig. 6.26(a). The prediction of H_{cJ} is very close to the permeagraph measurements, so that it can be assumed this quantity is measured correctly. Second, as already mentioned before, the \mathfrak{D} -function is not predicted correctly, so M_{mag} is not subtracted with the right factorization. When rewriting formula 7.2 using the apparent polarization,

$$H_{mag,QCM} = H_{air,QCM} - \frac{\mathfrak{D}}{1 - \mathfrak{D}} \frac{J_{mag,appa}}{\mu_0} \quad (7.3)$$

it can be seen how the incorrect prediction of $J_{mag,appa}$ and the \mathfrak{D} -function, shown in Fig. 7.6(b), will affect the estimation of H_{mag} . Future studies have to show how the estimation of $J_{mag,appa}$ as well as the \mathfrak{D} -function can be improved.

To measure the repeatability, several tests were conducted with the same specimen. Due to the lack of time only five repetitions were done for each magnetization test. Assuming that by heating the magnets over the Curie temperature the magnets will return to their default state, it can be said that for the test with a non-conductive

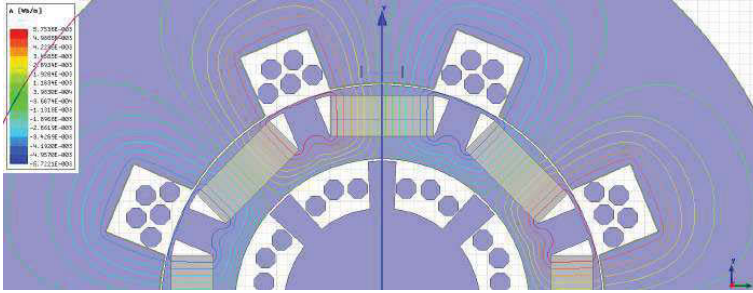


Fig. 7.10: Field for 0 A for a ferrous magnetizing fixture with magnetized magnets

rotor, the repeatability error is caused by mechanical and electrical tolerances. To differentiate between electrical and mechanical tolerances, copper ashlar which have the same size as the magnets were magnetized in a non-conductive rotor. The repeatability error, when carrying out a consecutive magnetization without taking the rotor out in between, are in the same range compared to pure consecutive measurements (see Fig. 6.25). It can be stated that either a majority of the errors originate from electrical tolerances, i.e. measurement tolerances, or the force due to the high current causes small vibrations of the search coils, mentioned in [28], or even of the magnets of the rotor. The repeatability error for a hysteresis measurement of a M275-35A rotor without magnets where the same procedure was conducted is shown in Fig. 6.22. The repeatability error for the demagnetizing curve is in the same range for both methods. The repeatability error for a non-conductive and a steel rotor (see Fig. 6.26(b) and Fig. 6.27(b)) are also in the same range, which might support the theory of the moving coils. Using a different M270-35A rotor but with same magnets also shows a repeatability error in the same range (see Fig. 6.23).

Detecting a missing magnet can be done very precisely with the introduced method as shown in section 6.5.4. The simulation agrees well with the measurements, also for the neighboring magnet next to the empty pocket. In the future, different magnets, i.e. with different coercive field strength, should be tested to see how the magnets influence each other.

Eddy effects which influence the measurements the most, can be compensated except within the first half oscillation. The very easy method introduced in section 5.2.9 is dependent on $\frac{dB_{mag,z}}{dt}$ which has a maximum at $t = 0$. Therefore in this case, the total field including eddy effect field weakening has to be investigated at the beginning, and not only the $B_{mag,z}$ field component. Solving this is difficult because it presumes that the conductivity of the magnet is already known. Eddy effects could not be investigated for ashlar NdFeB magnets for the magnetizing coil because of manufacturing errors of the magnetizing fixture. For the PFM, it was shown that the method to compensate, these effects works well.

EMI problems are one of the most difficult aspects in a QCM and PFM due to very high currents. Even though the frequency of the load current is only about 1.8 kHz, commutating diodes in the freewheeling path generate high interferences, which might be resolved by better snubbers. Nevertheless, capacitive coupling between the field coil and the search coils also becomes a problem, especially if the B_{app} and the B_{mag} coils do not have the same length. In this case, these effects are not compensating each other and high peaks can be detected in the induced voltages. In Fig. 7.11, the compensated voltage U_M according to Fig. 6.13 with no magnets inserted is shown. As can be seen, this voltage is not zero, and is one of the major error sources of this measurement. Due to the different capacitive couplings of the search coils with the field coils, a big spike at 0 s is generated. Capacitive shielding might resolve this problem, which becomes

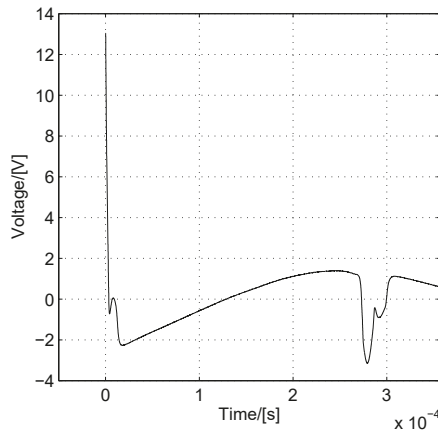


Fig. 7.11: U_m measured with no magnets after compensation

easier to manufacture if the wire of the search coil is not wound around a coil bobbin as for this prototype, but etched on a PCB or a direct bonded copper with a ceramic substrate [49]. From experience with the PFM described in section 6.3.1, two equal search coils with the same length and the same number of turns are easier to compensate. For the QCM this means that the length of the field coils have to be increased, resulting in larger inductances and resistances demanding bigger capacitive energies to generate the current necessary to magnetize the magnets.

Having magnetizing coils in and outside of the rotor increases the complexity of the magnetizing fixture. During testing it emerged that it is very useful to be able to access the compensator rotor from both sides, especially for the QCM, which is not possible with inner windings, since both sides have to be connected somehow. Changing the compensator easily might become necessary in case the lamination quality of the rotor differs.

A complete investigation of the tolerance chain has not been done yet because of the lack of time. For a detailed investigation, the tolerances have to be modeled in relation

to each other [36], which might become very time consuming and should be done in a follow up study.

8 Summary and Outlook

The goal of this work was to find ways to decrease the amount of magnet material by stray flux optimization. Additionally, it was shown that by simple insulation enhancements, the temperature inside the windings can be decreased, which might lead to a reduction in the size of the motor which saves magnet material. Additionally, the maximum temperature of the magnets can be decreased, leading to a reduction of the usage of HREE material. In case of a large increase in the price of the magnets, it is possible to change the vendor quickly without the need for a time consuming quality audit, since every magnet can be tested during magnetization.

8.1 Design for maximum Magnet material Exploitation

Easy to apply insulation material improvements can decrease the temperature inside the windings and lead to a higher continuous torque, or to a smaller/shorter motor. This helps to use less magnet material. The proposed ceramic filled liner which is already a standard material in power electronics has good mechanical strength, a high breakdown voltage and a good temperature resistivity. Additional thermal path improvements, e.g. by epoxies, lead to slightly better heat removal, but suffer from higher costs and might be subject to quality problems. Molded thermoplastics became a very common replacement for epoxies, but cannot fully penetrate every winding. Therefore, thermoplastics are just a good way to fixate the coils. The new thermal model is able to estimate all these effects for orthocyclically wound stators. The model can also predict compressed windings, and is therefore more effective than layer winding models [107]. In the future, this model should be also verified in real motor operation.

By using non-conductive cans, additional losses, which would increase the oil temperature and consequently the magnet temperature, are non-existent. Therefore, the Dysprosium content inside the magnets can be decreased leading to a lower H_{cJ} . This is acceptable if a decrease in short circuit current capability which results from a lower H_{cJ} is admissible. Glass fiber cans could be produced cheaper than their nickel alloy counterparts and might become even more important for environmental friendly automotive CO₂ air conditions [83]. In this case, even gas tightness can be assured by a second inner layer [33]. Zero Dy content for magnets used in combustion engine powered cars is still not achievable. Electric cars, where the maximum temperature is much lower compared to their combustion counterparts, might lead to Dy-Free auxiliary drives.

8.2 Design for Magnetization and Quality Control

Changing the magnet supplier quickly is important when it comes to rapidly fluctuating prices. With the Quality Control Magnetizer (QCM) it is possible to analyze every magnet during Post Assembly Magnetization (PAM). The quality estimation does not add any production time, and improves the state of the art total flux measurement method which cannot measure the demagnetizing curve.

The magnetization fixture has to be replaced by a laminated steel fixture for better heat removal, mechanical strength, tolerances and easier saturation of deep IPM rotors. The additional saturation as well as hysteresis effects will be challenging. According to simulations, the neighbor effect is aggravated if a steel magnetic fixture is used. Flux traps and magnetic guides generated by air pockets inside the magnetizing fixture have to be designed in such a way as to shield every magnet from its neighbor.

Bibliography

Scientific References

- [1] T. Albrecht, J. Franke, M. Merklein, and M. Schmidt. *Optimierte Fertigungstechnologien für Rotoren getriebeintegrierter PM-Synchronmotoren von Hybridfahrzeugen*. Meisenbach, 2014.
- [2] E. Algaer. *Thermal Conductivity of Polymer Materials-Reverse Nonequilibrium Molecular Dynamics Simulations*. PhD thesis, TU Darmstadt, 2010.
- [3] M.-L. Bash. *Modeling and design of wound-rotor synchronous machines using mesh-based magnetic equivalent circuits*. PhD thesis, PURDUE UNIVERSITY, 2010.
- [4] P. Beckley. *Electrical steels for rotating machines*. Number 37. IET, 2002.
- [5] M. Beleggia and M. De Graef. On the computation of the demagnetization tensor field for an arbitrary particle shape using a Fourier space approach. *Journal of Magnetism and Magnetic Materials*, 263(12):L1 – L9, 2003. ISSN 0304-8853.
- [6] N. Bianchi. *Electrical machine analysis using finite elements*. CRC press, 2005.
- [7] N. Bianchi, S. Bolognani, and P. Frare. Design criteria of high efficiency SPM Synchronous Motors. In *Electric Machines and Drives Conference IEMDC*, volume 2, pages 1042–1048, 2003.
- [8] K. Binnemans, P. Jones, B. Blanpain, T. Van Gerven, Y. Yang, A. Walton, and M. Buchert. Recycling of rare earths: a critical review. *Journal of Cleaner Production*, 51:1–22, 2013.
- [9] J. Blum, J. Merwerth, and H.-G. Herzog. Investigation of the segment order in step-skewed synchronous machines on noise and vibration. In *Electric Drives Production Conference (EDPC), 2014 4th International*, pages 1–6. IEEE, 2014.
- [10] A. Boglietti, A. Cavagnino, M. Lazzari, and M. Pastorelli. A simplified thermal model for variable-speed self-cooled industrial induction motor. *Industry Applications, IEEE Transactions on*, 39(4):945–952, 2003.
- [11] A. Boglietti, A. Cavagnino, and D. Staton. Determination of critical parameters in electrical machine thermal models. *Industry Applications, IEEE Transactions on*, 44(4):1150–1159, 2008.

- [12] M. Bonfe and M. Bergo. Mechatronic design of a PM brushless motor-driven gear pump with sensorless control. In *Power Electronics, Electrical Drives, Automation and Motion, 2008. SPEEDAM 2008. International Symposium on*, pages 239–244, June 2008. doi: 10.1109/SPEEDHAM.2008.4581081.
- [13] M. Brela, M. Michalski, H. Gebhardt, and J. Franke. Hall measurement method for the detection of material defects in plastic-embedded permanent magnets of rotors. In *Industrial Electronics Society, IECON 2013-39th Annual Conference of the IEEE*, pages 3928–3934. IEEE, 2013.
- [14] S. Brodersen and A. Kühn. Werkstoffe für Spalttöpfe und Spaltröhre bei leckagefreien Pumpen. *Technik Kompakt*, 3:6–8, 2000.
- [15] Y. Burkhardt. *Optimierter Entwurf hocheffizienter PM-Spaltröhrenmotoren für Pumpenapplikationen*. Shaker, 2011.
- [16] M. Buzio. Fabrication and calibration of search coils. *arXiv preprint arXiv:1104.0803*, 2011.
- [17] D.-X. Chen, J. Brug, and R. B. Goldfarb. Demagnetizing factors for cylinders. *Magnetics, IEEE Transactions on*, 27(4):3601–3619, Jul 1991. ISSN 0018-9464.
- [18] S.-y. Chen, K. Huang, and F. Juang. Improvement of a capacitor discharge impulse magnetizer circuit. In *Power Electronics and Drive Systems, 2003. PEDS 2003. The Fifth International Conference on*, volume 2, pages 1162–1163. IEEE, 2003.
- [19] S. Chikazumi and C. Graham. *Physics of Ferromagnetism*. International Series of Monographs on Physics. Clarendon Press, 1997. ISBN 9780191569852.
- [20] R.-N. Cornelius. *Pulsed Field Magnetometry for High-Speed Characterisation of Rare Earth Magnets*. PhD thesis, University of Plymouth, 2005.
- [21] G. Dajaku and D. Gerling. New methods for reducing the cogging torque and torque ripples of PMSM. In *Electric Drives Production Conference (EDPC), 2014 4th International*, pages 1–7. IEEE, 2014.
- [22] A. Demenko, J. V. Leite, A. Benabou, and N. Sadowski. Accurate minor loops calculation with a modified Jiles-Atherton hysteresis model. *COMPEL-The international journal for computation and mathematics in electrical and electronic engineering*, 28(3):741–749, 2009.
- [23] C. Dinca and U. Schäfer. Circulating currents of delta connected fractional slot machines for mass production. *e & i Elektrotechnik und Informationstechnik*, 132(1):68–74.
- [24] C. Dinca, M. Bushe, A. Giedymin, and U. Schafer. Mass producible optimized BLDC motor for automotive dynamic pump applications. In *Electrical Machines (ICEM), 2014 International Conference on*, pages 1286–1292. IEEE, 2014.

- [25] C. Dinca, A. Stockli, E. Ramezani, D. Schwarzer, Y. Cat, P. Korneluk, and U. Schafer. Characterization of a 7KJ magnetizing pulsed circuit for online quality control of permanent magnets. In *Pulsed Power Conference (PPC), 2015 IEEE*, pages 1–8. IEEE, 2015.
- [26] H. Dubbel, W. Beitz, and K.-H. Küttner. *DUBBEL: Taschenbuch für den Maschinenbau*. Springer-Verlag, 2013.
- [27] J. Dudding, P. Knell, R. Cornelius, B. Enzberg Mahlke, W. Fernengel, R. Grössinger, M. Küpferling, P. Lethuillier, G. Reyne, M. Taraba, et al. A pulsed field magnetometer for the quality control of permanent magnets. *Journal of magnetism and magnetic materials*, 242:1402–1404, 2002.
- [28] D. Eckert, R. Grössinger, M. Doerr, F. Fischer, A. Handstein, D. Hinz, H. Siegel, P. Verges, and K.-H. Müller. High precision pick-up coils for pulsed field magnetization measurements. *Physica B: Condensed Matter*, 294:705–708, 2001.
- [29] T. Elwert and D. Goldmann. Entwicklung eines hydrometallurgischen Recyclingverfahrens für NdFeB-Magnete. *Herstellung und Recycl. von Technol. H*, 133:81–96, 2013.
- [30] J. Espina Hernández, R. Grössinger, S. Kato, H. Hauser, and E. Estévez Rams. New sensors for measuring M and H in high magnetic fields. *Physica B: Condensed Matter*, 346:543–547, 2004.
- [31] J. Espina Hernández, R. Grössinger, R. Sato Turtelli, and J. Hallen. A new measuring system for determining the magnetic viscosity in permanent magnets. *Advanced Materials Research*, 68:12–20, 2009.
- [32] F. Fiorillo, C. Beatrice, O. Bottauscio, and E. Patroi. Measuring the hysteresis loop of permanent magnets with the pulsed field magnetometer. *Magnetics, IEEE Transactions on*, 43(7):3159–3164, 2007.
- [33] R. Funck. Composite materials in high efficient sleeve applications of electric machines. 2015. URL <http://www.circomp.de/de/downloads/CirComp-high-efficient-sleeve-applications.pdf>. viewed on 16th February 2016, 11:21.
- [34] J. Geraint. *The Computer-Aided Design and Analysis of Impulse Magnetizing Fixtures*. PhD thesis, University of Sheffield, 1992.
- [35] German Association of Steam Boiler, Pressure Vessel and Piping Manufacturers e.V. *AD 2000*. Beuth, 2011.
- [36] I. Gertsbakh. *Measurement theory for engineers*. Springer, 2003.
- [37] E. Gholz. Rare Earth Elements and National Security. *Council on Foreign*, 701, 2014.
- [38] D. Givord, A. Lienard, P. Tenaud, and T. Viadieu. Magnetic viscosity in Nd-Fe-B sintered magnets. *Journal of Magnetism and Magnetic Materials*, 67(3): L281 – L285, 1987. ISSN 0304-8853.

- [39] A. Gkountaras, C. Dinca, A. Giedymis, P. Birgel, U. Schaefer, and S. Dieckerhoff. Low cost integrated motor-controller drive for an electrical active suspension system. In *Power Electronics and Applications (EPE'14-ECCE Europe), 2014 16th European Conference on*, pages 1–10, Aug 2014. doi: 10.1109/EPE.2014.6910931.
- [40] C. Golovanov, G. Reyne, G. Meunier, R. Grossinger, and J. Dudding. Finite element modeling of permanent magnets under pulsed field. *Magnetics, IEEE Transactions on*, 36(4):1222–1225, Jul 2000. ISSN 0018-9464.
- [41] A. Graf. Halbleiter im 42V-Bordnetz. VDE, October 2001.
- [42] R. Grössinger. Characterisation of Hard Magnetic Materials. *Electrical Engineering*, 59(7):15–20, 2008.
- [43] R. Grössinger, J. Tellez Blanco, R. Sato Turtelli, R. Hauser, K. Reiterer, H. Sasik, and G. Chouteau. Determination of the magnetic viscosity in SmCo_{5-x}Cu_x alloys by pulsed-field method. *Physica B: Condensed Matter*, 294-295(0):194 – 198, 2001. ISSN 0921-4526. Proceedings of the Sixth International Symposium on Research in High Magnetic Fields.
- [44] R. Grössinger, M. Küpferling, P. Kasperkovitz, A. Wimmer, M. Taraba, W. Scholz, J. Dudding, P. Lethuillier, J. Toussaint, B. Enzberg Mahlke, et al. Eddy currents in pulsed field measurements. *Journal of magnetism and magnetic materials*, 242:911–914, 2002.
- [45] R. Grössinger, M. Taraba, A. Wimmer, J. Dudding, R. Cornelius, P. Knell, P. Bissel, B. Enzberg Mahlke, W. Fernengel, J. Toussaint, et al. Calibration of an industrial pulsed field magnetometer. *Magnetics, IEEE Transactions on*, 38(5):2982–2984, 2002.
- [46] R. Grössinger, R.-S. Turtelli, and C. Tellez Blanco. The influence of the magnetic viscosity on pulsed field measurements. *Journal of Optoelectronics and Advanced Materials*, 6:557–564, 2004.
- [47] M. Haavisto. *Studies on the Time-Dependent Demagnetization of Sintered NdFeB Permanent Magnets*. PhD thesis, Tampere University of Technology, 2013.
- [48] I. Hamdhan and B. Clarke. Determination of thermal conductivity of coarse and fine sand soils. In *Proceedings of World Geothermal Congress*, 2010.
- [49] G. Hanreich, M. Mündleina, H. Hauser, J. Nicolics, G. Stangl, R. Grössinger, and J. Espina-Hernandez. Ultra-thin pick-up coil for surface flux detection. *Sensors and Actuators A, Physical*, 91(1):57–60, 2001.
- [50] H. Harstick. *Einfluss des Schneidens auf die magnetischen Eigenschaften von Elektroblech*. Papierflieger-Verlag, 2014.
- [51] T. Heikkilä. Permanent magnet synchronous motor for industrial inverter applications-analysis and design. *Acta Universitatis Lappeenrantaensis*, 2002.

- [52] K.-H. Hellwege et al. Wärmeleitung in Polyamiden, Penton und Polyoxyäthylen im Temperaturbereich von -175 bis+ 140C. *Kolloid-Zeitschrift und Zeitschrift für Polymere*, 226(2):109–115, 1968.
- [53] J.-R. Hendershot and T.-J.-E. Miller. *Design of brushless permanent-magnet machines*. Motor Design Books, 2010.
- [54] H. Henke. *Elektromagnetische Felder: Theorie und Anwendung*. Springer-Verlag, 2011.
- [55] C. Horst, S. Tetsuya, and S. Leslie. *Handbook of Materials Measurement Methods*. Springer, Berlin, 2006.
- [56] M.-F. Hsieh, Y.-M. Lien, and D. G. Dorrell. Post-assembly magnetization of rare-earth fractional-slot surface permanent-magnet machines using a two-shot method. *Industry Applications, IEEE Transactions on*, 47(6):2478–2486, 2011.
- [57] M.-F. Hsieh, D. G. Dorrell, C.-K. Lin, P.-T. Chen, and P. Y. Wung. Modeling and effects of in situ magnetization of isotropic ferrite magnet motors. *Industry Applications, IEEE Transactions on*, 50(1):364–374, 2014.
- [58] S.-M. Hwang, J.-B. Eom, Y.-H. Jung, D.-W. Lee, and B.-S. Kang. Various design techniques to reduce cogging torque by controlling energy variation in permanent magnet motors. *IEEE transactions on magnetics*, 37(4):2806–2809, 2001.
- [59] H. Igarashi, D. Lederer, A. Kost, T. Honma, and T. Nakata. A numerical investigation of Preisach and Jiles models for magnetic hysteresis. *COMPEL-The international journal for computation and mathematics in electrical and electronic engineering*, 17(3):357–363, 1998.
- [60] F. Incropera and D. DeWitt. *Introduction to heat transfer*. 1985.
- [61] T. Ishigami, K. Yamazaki, K. Ohara, and T. Aoki. Manufacturing technology for continuous high-density coils for brushless motors. *Precision engineering*, 31(3):260–268, 2007.
- [62] T. Ishigami, M. Kitamura, and K. Sanada. Stator-core structure and winding technology for EPS motors. *Electrical Engineering in Japan*, 175(1):35–42, 2011.
- [63] T. Ishigami, Y. Tanaka, and H. Homma. Development of Motor Stator with Rectangular-Wire Lap Winding and an Automatic Process for Its Production. *Electrical Engineering in Japan*, 187(4):51–59, 2014.
- [64] W. Ismar Borges de Lima, editor. *Rare Earth Industry*. Elsevier, 2016.
- [65] L. Jahn, R. Schumann, and W. Rodewald. Magnetic viscosity of modified neodymium iron boron magnets with high coercivities. *Journal of magnetism and magnetic materials*, 153(3):302–310, 1996.

- [66] G. Jewell, D. Howe, C. Schotzko, and R. Grossinger. A method for assessing eddy current effects in pulsed magnetometry. *Magnetics, IEEE Transactions on*, 28(5):3114–3116, Sep 1992. ISSN 0018-9464.
- [67] G. Jewell, D. Howe, and C. Riley. The design of radial-field multipole impulse magnetizing fixtures for isotropic NdFeB magnets. *Magnetics, IEEE Transactions on*, 33(1):708–722, Jan 1997. ISSN 0018-9464.
- [68] M. Jones and D. Hull. Microscopy of failure mechanisms in filament-wound pipe. *Journal of Materials Science*, 14(1):165–174, 1979.
- [69] W. Jordan. *Technologie kleiner Elektromaschinen, Teil 1*. Technoexpoert Desden, 2 edition, 2013.
- [70] W. Jordan. *Technologie kleiner Elektromaschinen, Teil 2*. Technoexpoert Desden, 1 edition, 2013.
- [71] W. Jordan. *Technologie kleiner Elektromaschinen, Teil 3*. Technoexpoert Desden, 1 edition, 2015.
- [72] S. Junker. *Technologien und Systemlösungen für die flexibel automatisierte Bestückung permanent erregter Läufer mit oberflächenmontierten Dauermagneten*. Meisenbach, 2007.
- [73] A. Kampker. *Elektromobilproduktion*. Springer-Verlag, 2014.
- [74] O. Khan, C. Ragusa, F. Khan, and B. Montrucchio. A Mutual Demagnetizing Tensor for N-Body Magnetic Field Modeling. *Magnetics, IEEE Transactions on*, 49(7):3179–3182, July 2013. ISSN 0018-9464.
- [75] A. Kirste. *Magnetization measurements in ultrahigh magnetic fields*. PhD thesis, Humboldt-Universität zu Berlin, Mathematisch-Naturwissenschaftliche Fakultät I, 2004.
- [76] K. Kodama. Measurement of dynamic magnetization induced by a pulsed field: Proposal for a new rock magnetism method. *Frontiers in Earth Science*, 3(5), 2015. ISSN 2296-6463.
- [77] K. Koyama and T. Takeuchi. MITSUBISHI ELECTRIC. 2006.
- [78] R. Krishnan. *Permanent magnet synchronous and brushless DC motor drives*. CRC press, 2009.
- [79] D. Kujawski, F. Ellyin, and M. Culen. The Fatigue Behaviour of Filament-Wound Fiberglass/Epoxy Tubes under Cyclic Pressure. *Journal of Reinforced Plastics and Composites*, 17:268–280, 1998.
- [80] B. Lacovara. Considering Resin Transfer Molding. *Composites Fabrication Association S*, 199, 1995.
- [81] E. Lamprecht, J. Franke, M. Merklein, and M. Schmidt. *Der Einfluss der Fertigungsverfahren auf die Wirbelstromverluste von Stator-Einzelzahnblechpaketen für den Einsatz in Hybrid-und Elektrofahrzeugen*. Meisenbach, 2014.

- [82] K. Lee, J. Hong, S. Lee, and S. Lee. Quality assurance testing for magnetization quality assessment of BLDC motors used in compressors. *Industry Applications, IEEE Transactions on*, 46(6):2452–2458, 2010.
- [83] M.-Y. Lee and D.-Y. Lee. Review on Conventional Air Conditioning, Alternative Refrigerants, and CO2 Heat Pumps for Vehicles. *Advances in Mechanical Engineering*, 5:713924, 2013.
- [84] D. Lin, P. Zhou, and A. Bergqvist. Improved Vector Play Model and Parameter Identification for Magnetic Hysteresis Materials. *Magnetics, IEEE Transactions on*, 50(2):357–360, 2014.
- [85] D. Lin, P. Zhou, C. Lu, N. Chen, and M. Rosu. Construction of magnetic hysteresis loops and its applications in parameter identification for hysteresis models. In *Electrical Machines (ICEM), 2014 International Conference on*, pages 1050–1055. IEEE, 2014.
- [86] A. Lyberatos. Magnetic viscosity and the field rate dependence of the magnetization. *Journal of magnetism and magnetic materials*, 202(1):239–250, 1999.
- [87] A. Meyer, A. Heyder, M. Brela, N. Urban, J. Sparrer, and J. Franke. Fully automated rotor inspection apparatus with high flexibility for permanent magnet synchronous motors using an improved hall sensor line array. In *Electric Drives Production Conference (EDPC), 2015 5th International*, pages 1–5. IEEE, 2015.
- [88] G. Müller, K. Vogt, and B. Ponick. *Berechnung elektrischer Maschinen*. Number Bd. 2 in Berechnung elektrischer Maschinen. Wiley-VCH, 2008. ISBN 9783527405251.
- [89] V. Müller Benedict. Grundkurs Statistik in den Sozialwissenschaften: eine leicht verständliche, anwendungsorientierte Einführung in das sozialwissenschaftlich notwendige statistische Wissen. 4., überarbeitete Auflage. *Auflage. Wiesbaden*, 2007.
- [90] Z. G. Nagy. *Modeling and analysis of the magnetization, torque and dynamics of untethered soft-magnetic microrobots*. PhD thesis, Diss., Eidgenössische Technische Hochschule ETH Zürich, Nr. 19529, 2011, 2011.
- [91] M. Naidu, T. Nehl, S. Gopalakrishnan, and L. Wurth. A semi-integrated sensorless PM brushless drive for a 42 V automotive HVAC compressor. In *Industry Applications Conference, 2003. 38th IAS Annual Meeting. Conference Record of the*, volume 3, pages 1435–1442 vol.3, Oct 2003. doi: 10.1109/IAS.2003.1257746.
- [92] T. Oikawa, T. Tajima, K. Masumoto, H. Akita, H. Kawaguchi, and H. Kometani. Development of high efficiency brushless DC motor with new manufacturing method of stator for compressors. 2002.
- [93] S. Pan. *Rare Earth Permanent-Magnet Alloys High Temperature Phase Transformation*. Springer, 2013.

- [94] J.-S. Park, J.-H. Choi, B.-G. Gu, and I.-S. Jung. BLDC drive control of electric water pump for automotive application. In *Vehicle Power and Propulsion Conference (VPPC), 2010 IEEE*, pages 1–5, Sept 2010.
- [95] K. Potter. *Resin transfer moulding*. Springer Science & Business Media, 2012.
- [96] F. Rothwarf, S. Simizu, M. Huang, and R. Schaefer. Pulsed field magnetometer for nondestructive monitoring of encapsulated magnetic materials. *Journal of applied physics*, 73(10):5614–5616, 1993.
- [97] J. Rousseau, D. Perreux, and N. Verdier. The influence of winding patterns on the damage behaviour of filament-wound pipes. *Composites Science and Technology*, 59(9):1439–1449, 1999.
- [98] B. Rowden, F. Barlow, J. Balda, A. Elshabini, G. Garcia, R. Leidhold, C. De Angelo, G. Bossio, and D. Forchetti. Integrated motors and controllers for 42 V automotive auxiliary motor applications. In *Power Electronics in Transportation, 2004*, pages 97–102, Oct 2004. doi: 10.1109/PET.2004.1393807.
- [99] T. L. Saaty. Decision making with the analytic hierarchy process. *International journal of services sciences*, 1(1):83–98, 2008.
- [100] P. Salminen et al. Fractional slot permanent magnet synchronous motors for low speed applications. *Acta Universitatis Lappeenrantaensis*, 2004.
- [101] W. Schatt, K.-P. Wieters, and B. Kieback. *Pulvermetallurgie*. Springer, 2007.
- [102] H. Schilp, P. Schlag, and M. Kohnhauser. Optimized handling of permanent magnets within the mass production of electric traction drives. In *Electric Drives Production Conference (EDPC), 2013 3rd International*, pages 1–6, Oct 2013. doi: 10.1109/EDPC.2013.6689728.
- [103] K. Seiichi and K. Giyuu. Pulsed field magnetometer for low-temperature study of high-performance permanent magnets. *Magnetics, IEEE Transactions on*, 36(5):3634–3636, 2000.
- [104] C. Sinohui. A Comparison of Methods of Attaching Thermocouples to Printed Circuit Boards for Thermal Profiling. In *Nepcon West*, pages 866–875. CAHNERS EXPOSITION GROUP, 1999.
- [105] L. Song, Z. Li, J. Gao, Q. Zeng, and F. Wang. 3D thermal analysis of water cooling induction motor used for HEV. In *Electrical Machines and Systems, 2008. ICEMS 2008. International Conference on*, pages 534–537. IEEE, 2008.
- [106] M.-S. Song, Y.-b. Kim, C.-S. Kim, and T.-K. Kim. Measurement accuracy of a pulsed field magnetometer designed for rare earth based permanent magnets. *Magnetics, IEEE Transactions on*, 36(5):3637–3639, Sep 2000. ISSN 0018-9464.
- [107] D. Staton, A. Boglietti, and A. Cavagnino. Solving the more difficult aspects of electric motor thermal analysis in small and medium size industrial induction motors. *Energy conversion, iee transactions on*, 20(3):620–628, 2005.

- [108] W. Stautner, S. Mine, K. Sivasubramaniam, J. Rochford, E. Budesheim, and K. Amm. A Cryo-Free 10 T High-Field Magnet System for a Novel Superconducting Application-Experimental Results. *Applied Superconductivity, IEEE Transactions on*, (3):9500905–9500905, June 2012. ISSN 1051-8223.
- [109] G. Stone, E. Boulter, I. Culbert, and H. Dhirani. Electrical insulation for rotating machines-design, evaluation, aging, testing, and repair-Book. *IEEE Electrical Insulation Magazine*, 3(20):65, 2004.
- [110] R. Streiter. Active preview suspension system - ABC Prescan in the F700. *ATZ worldwide eMagazines*, 110, 2008.
- [111] H. Takayanagi, M. Xia, and K. Kemmochi. Stiffness and strength of filament-wound fiber-reinforced composite pipes under internal pressure. *Advanced Composite Materials*, 11(2):137–149, 2002.
- [112] J. Téllez Blanco, R. Sato Turtelli, R. Grössinger, E. Estévez Rams, and J. Fidler. Giant magnetic viscosity in SmCo₅x Cux alloys. *Journal of applied physics*, 86(9), 1999.
- [113] H. Ting and J. Seaman. Rare Earths: Future Elements of Conflict in Asia? *Asian Studies Review*, 37(2):234–252, 2013.
- [114] W. Tong. *Mechanical design of electric motors*. CRC Press, 2014.
- [115] J. Tremel and J. Franke. Hall sensor line array for magnetic field inline measurements of PM-excited rotors. In *Electric Drives Production Conference (EDPC), 2012 2nd International*, pages 1–4. IEEE, 2012.
- [116] S. Trojanowski and M. Ciszek. Sensitivity of the integrating pulse magnetometer with a first-order gradiometer. *Review of Scientific Instruments*, 79(10):104702, 2008.
- [117] S. Tumanski. *Handbook of magnetic measurements*. CRC Press, 2011.
- [118] R. Tzscheutschler, H. Olbrich, and W. Jordan. *Technologie des Elektromaschinenbaus*. Verlag Technik, 1990.
- [119] VDI Richtlinie. 2225: Technisch-wirtschaftliches Konstruieren. *Düsseldorf: VDI*, 1964.
- [120] K. Vervaeke. 6D magnetic field distribution measurements of permanent magnets with magnetic field camera scanner. In *Electric Drives Production Conference (EDPC), 2015 5th International*, pages 1–4. IEEE, 2015.
- [121] A. Wygralak. National Geochemical Survey of Australia: interpretation of selected Northern Territory data. *National Geochemical Survey Record 2012-005*, 2012.
- [122] M. Xia, K. Kemmochi, and H. Takayanagi. Analysis of filament-wound fiber-reinforced sandwich pipe under combined internal pressure and thermomechanical loading. *Composite structures*, 51(3):273–283, 2001.

- [123] L. Yao. *Magnetic field modelling of machine and multiple machine systems using dynamic reluctance mesh modelling*. PhD thesis, University of Nottingham, 2006.
- [124] D. Zarko, D. Ban, T. Lipo, et al. Analytical solution for cogging torque in surface permanent-magnet motors using conformal mapping. *Magnetics, IEEE Transactions on*, 44(1):52–65, 2008.
- [125] J. Zerbe, C. Dinca, and U. Schafer. Hardware guide winding and hot wire winding. In *Electric Drives Production Conference (EDPC), 2015 5th International*, pages 1–6. IEEE, 2015.
- [126] L. Zhu, S. Jiang, L. Zhu, and C. Chan. Comparison of alternate analytical models for predicting cogging torque in surface-mounted permanent magnet machines. In *Vehicle Power and Propulsion Conference, 2008. VPPC'08. IEEE*, pages 1–6. IEEE, 2008.
- [127] Z. Zhu and D. Howe. Influence of design parameters on cogging torque in permanent magnet machines. *Energy Conversion, IEEE Transactions on*, 15(4):407–412, 2000.
- [128] H. Zijlstra. *Experimental methods in Magnetism*. North-Holland, 1967.

Patent References

- [129] J. Baumeister. Permanentmagnet-Rotor für einen Elektromotor, April 2012.
- [130] F. J. Biais and K. M. Rahman. Auxiliary magnetizing winding for interior permanent magnet rotor magnetization, Jan. 6 2004. US Patent 6,674,205.
- [131] W. König. Verfahren und Vorrichtung zur überwachung eines Magnetisierungsprozesses von Magnetpolen, Nov. 6 2014. DE Patent App.
- [132] W. Luetge. WINDING METHOD, IN PARTICULAR FOR PRODUCING ELECTRIC COILS, 2011.
- [133] B. Van and J. Deschagt. Discriminating magnetic material properties. Patent, November 2008. WO Patent App. PCT/EP2008/056,316.

Student Theses

- [134] C. Berkman. Integration Technologies for Motor and Power Electronics. Master Thesis, 13th September 2014.
- [135] M. Bushe. Mechanische Auslegung eines hochdynamischen Elektromotors für eine adaptive Wankstabilisierung. Bachelor Thesis, 9th January 2012.
- [136] Y. Cat. Entwurf eines Magnetisierprüfstands für eingebettete NdFeB-Magnete in einem BLDC-Rotor. Bachelor Thesis, 27th of June 2014.

- [137] M. Franke. Implementierung eines MTPA/MTPW Regelalgorithmuses für den E-Suspension Antrieb, 4th September 2014.
- [138] A. Giedymin. Entwurf und Implementierung einer Regelung eines hochdynamischen Elektroantriebs für eine adaptive Wankstabilisierung nach ISO 26262. Bachelor Thesis, 26th Oktober 2012.
- [139] P. Korneluk. Auslegung eines Freilaufkreises zur Erzeugung einer negativen Hochstromhalbwellen für eine Magnetisierungsanordnung. Bachelor Thesis, 25th July 2014.
- [140] R. Rissmann. Magnetfeldmessung und Qualitätskontrolle eines BLDC Rotors mit vergrabenen Magneten während eines Magnetisierungsvorganges. Bachelor Thesis, 23rd of June 2014.
- [141] D. Schwarzer. Vergleich zweier Magnetisierungsanordnungen zur Verbesserung der Magnetausnutzung eines BLDC-Rotors mit vergrabenen Magneten. Bachelor Thesis, 16th October 2013.
- [142] D. Schwarzer. Design and Test of a Foldable Motor Integrated Low Voltage Inverter for Automotive Applications. Master Thesis, 8th October 2015.

Scripts

- [143] U. Schäfer. Elektrische Antriebe 2. viewed on 1st December 2015; 17:35, Winter Semester 2015/16.

Data Sheets

- [144] ABB. 5SDD 38H5000. Data Sheet, August 2011. URL http://5scomponents.thomasnet.com/asset/5SDD_38H5000_5SYA1177-00Sept_07-1-.pdf. viewed on 24th November 2015, 19:45.
- [145] Arcelor Mittal. Enhanced fully processed electrical steels for automotive traction applications. Presentations, July 2008. URL http://www.abmbrasil.com.br/cim/download/20080702_sigrid.pdf. viewed on 19th October 2015, 14:06.
- [146] Argus Media Limited. Metal-Pages. URL <http://www.metal-pages.com/>. viewed on 28th February 2015, 18:07.
- [147] K. Bennion. Electric Motor Thermal Management. Presentation, May 2012. URL http://energy.gov/sites/prod/files/2014/03/f10/ape030_bennion_2012_o.pdf. viewed on 19th October 2015.
- [148] Bomatec. Werkstoffdaten / Material data sheet BMN-35H. Data Sheet. URL <http://www.bomatec.ch/files/downloads/datenblaetter/ndfeb/BMN-35H.pdf>. viewed on 17th November 2015, 11:42.

- [149] K. Bourzac. The Rare-Earth Crisis. Internet, April 2011. URL <http://www.technologyreview.com/featuredstory/423730/the-rare-earth-crisis/>. Viewed on 30th of September 2015, 09:57.
- [150] K. Bradsher. Earth-Friendly Elements, Mined Destructively, December 2009. URL <http://www.nytimes.com/2009/12/26/business/global/26rare.html>. viewed on 30th September 2015, 09:58.
- [151] Daimler AG and Porsche AG and VW AG and BMW Group. Elektrische und elektronische Komponenten im Kraftfahrzeug 48V-Bordnetz, August 2011.
- [152] DELO. DELO-MONOPOX AD066. Data Sheet. URL http://www.syneo.net/pdf/Colle/%23MP/resine-epoxy-mono-composant_DELO-MONOPOX_AD066_8TIDB-GB29.pdf. viewed on 12th of October 2015.
- [153] Deutsche Edelstahlwerke. Werkstoffdatenblatt 1.4571. Data Sheet, December 2015. URL http://www.dew-stahl.com/fileadmin/files/dew-stahl.com/documents/Publikationen/Werkstoffdatenblaetter/RSH/1.4571_de.pdf. viewed on 13th February 2016, 14:45.
- [154] DIN. Magnetische Werkstoffe - Teil 8-1: Anforderungen an einzelne Werkstoffe - Hartmagnetische Werkstoffe, August 2005.
- [155] DIN. Prüfverfahren zur Bestimmung des Temperaturindex von Lackdrähten. DIN EN 60172:2014, 2010-11.
- [156] DIN. Technische Lieferbedingungen für bestimmte Typen von Wickeldrähten. DIN EN 60317-51, 2013.
- [157] Dupont. Mylar A polyester film physical-thermal properties. Data Sheet, June 2003. URL http://usa.dupontteijinfilms.com/informationcenter/downloads/Physical_And_Thermal_Properties.pdf. viewed on 30th of September 2015, 17:50.
- [158] Dupont. Dupont nomex paper type 410. Data Sheet, August 2013. URL http://www.dupont.com/content/dam/assets/products-and-services/electronic-electrical-materials/assets/DPP_Nomex410_K20612-1.pdf. viewed on 30th of September 2015, 17:52.
- [159] Elantas. Elan-tron MC 5470 FR /W 5710. Data Sheet, October 2009. URL http://scheiing.de/wcms/ftp//s/scheiing.de/uploads/elan-tron_mc_5470_fr.pdf. viewed on 22th October 2015, 15:10.
- [160] Electronicon. E59.A18-694010. Data Sheet, 2007. URL http://www.electronicon.com/fileadmin/inhalte/pdfs/downloadbereich/Katalog/neue_Kataloge_2011/200.003-020070.pdf. viewed on 24th November 2015, 19:17.
- [161] Fenner Drives. Product Catalogue Fenner Drives, Trantorque Mini. Catalogue, 2015. URL <http://www.fennerdrives.com/FetchFile.ashx?id=cc515d1e-c9ef-49d9-acd3-3272eb879463>. viewed on 15th October 2015, 12:45.

- [162] Fluke. Fluke Digital Multimeter. Data Sheet, December 1991. URL http://assets.fluke.com/manuals/8840A___imeng0300.pdf. viewed on 29th January 2016, 14:10.
- [163] Forum ElektroMobilität e.V. E-Mail Das Magazin für die Mobilität von Morgen, January 2015. URL http://www.forum-elektromobilitaet.de/assets/mime/567b67c1afec32018d98d7070c6e6e3f/Newsmagazin_Forum_ElektroMobilitaet.pdf. viewed on 18th February 2016, 17:46.
- [164] R. Grössinger. Hirst Pulsed Field Magnetometer.
- [165] HAYMES International. HASTELLOY C-22 alloy. Data Sheet. URL http://www.haynes.ch/doc/haynes/c22_h2019.pdf. Viewed on 4th of December 2015.
- [166] Heermann. Heersolit Backlackdrähte, April 1999. URL http://www.ruggaber.de/kupfer/dblheermann/uebersback_heerm.pdf. viewed on 30th of September 2015, 10:06.
- [167] Infineon. TLE 500X Application Note GMR Accuracy Extension. Data Sheet, August 2011. URL http://www.infineon.com/dgdl/Angle_Error_Extension_GMR_AN_Rev+1+2.pdf?fileId=db3a304332fc1ee7013311373b643bd6. viewed on 30th September 2015, 10:09.
- [168] Infineon. TLE 5012B Data Sheet. Data Sheet, February 2014. URL http://www.infineon.com/dgdl/Infineon-TLE5012B_Exxxx-DS-v02_00-en.pdf?fileId=db3a304334fac4c601350f31c43c433f. viewed on 30th of September 2015, 10:08.
- [169] INFO-RE Information on Rare Earth. The leading Rare Earth Information Provider in the World. Internet. URL <http://www.info-re.com/#&panel1-1>. viewed on 28th February 2015, 18:06.
- [170] Isodraht. Isoflex (IF). Data Sheet. URL <http://www.ruggaber.de/kupfer/dblisodraht/IsodrahtIsoflexIF.pdf>. viewed on 30th September 2015, 10:18.
- [171] Keller. Digital Manometer LEO 1. Data Sheet, July 2007. URL <http://www.keller-druck.com/picts/pdf/engl/leo1e.pdf>. viewed on 15th October 2015.
- [172] Kerafol. Keratherm 86/37. Data Sheet, June 2014. URL http://www.kerafol.com/fileadmin/user_upload/Thermalmanagement/produkte/86_37/Datenblatt_86_37_EN.pdf. viewed on 30th of September 2015, 17:11.
- [173] LEM. Current Transducer LT 100-S/SP30. Data Sheet. URL <http://www.europowercomponents.com/media/uploads/LT100-S-SP30.pdf>. viewed on 29th January 2016, 14:10.

- [174] Loctite. Loctite 5091. Data Sheet, June 2015. URL <https://tds.us.henkel.com/NA/UT/HNAUTDS.nsf/web/0313048B00138147882571870000D7C9/File/SI%205091-EN.pdf>. viewed on 01 November 2015, 17:41.
- [175] LORENZ MESSTECHNIK GmbH. DR-2212, DR-2212-R Torque Sensor. Data Sheet, . URL http://www.physicomcorp.com/doc_series/DR2212_Ser_Ovr.pdf. viewed on 27th October 2015.
- [176] LORENZ MESSTECHNIK GmbH. DR-2643, DR-2643-P. Data Sheet, . URL http://www.lorenz-messtechnik.de/pdfdatbl/m/080720g_dr-2643.pdf. viewed on 1st February 2016.
- [177] M-pulse GmbH. Magnetizing coils for Rotors. Website. URL http://www.m-pulse.eu/english/products/motor_coils.html. viewed on 25th November 2015, 18:42.
- [178] Magnet-Physik. PERMAGRAPH C. Data Sheet, 2008. URL http://www.magnet-physik.de/fileadmin/Mediendatenbank/1_Produkte/2_Messtechnik/Datenbl%C3%A4tter/Permagraph_C_e_2092.pdf. viewed on 11th of November 2015. 18:37.
- [179] MAGSYS magnet systeme GmbH. Magnetisiervorrichtungen. Website. URL <http://www.magsys.de/index.php/de/produkte-dienstleistungen/magnetisiervorrichtungen>. viewed on 25th November 2015, 18:44.
- [180] National Instruments. NI sbRIO-961x /963 x /964 x. Data Sheet, June 2010. URL www.ni.com/pdf/manuals/375052c.pdf. viewed on 27th October 2015, 17:47.
- [181] Omega Engineering. Revised Thermocouple Reference Tables. Data Sheet. URL <http://www.omega.com/temperature/Z/pdf/z207.pdf>. viewed on 29th January 2016, 14:13.
- [182] Omega Engineering. Omega HH147U. Data Sheet, January 2011. URL <http://www.omega.de/temperature/pdf/HH147U.pdf>. viewed on 29th January 2016, 14:16.
- [183] Power Electronic Measurements Ltd. Rogowski Coil LFR Specification. Data Sheet, November 2010. URL http://www.pemuk.com/Userfiles/LFR/LFR_1110.pdf. viewed on 25th January 2016, 15:33.
- [184] Quadrant Engineering Plastics. Techtron HPV PPS. Data Sheet, March 2011. URL http://media.quadrantplastics.com/fileadmin/quadrant/documents/QEPP/EU/Product_Data_Sheets_PDF/AEP/Techtron_1000_PPS_PDS_D_27042011.pdf. viewed on 30th of September 2015, 17:13.
- [185] Quadrant Engineering Plastics. Duratron T4203. Data Sheet, April 2011. URL http://www.quadrantplastics.com/fileadmin/quadrant/documents/QEPP/EU/Product_Data_Sheets_PDF/AEP/Duratron_T4203___T4503_PAIPDS_E_28042011.pdf. viewed on 30th of September 2015, 17:11.

- [186] Refu Elektronik. Data Sheet RPCS 630. Data Sheet. URL http://www.refu-drive.de/fileadmin/user_upload_drive/Download/1504_refudrive_630_datenblatt_RZ_de_SCREEN-Einzelseiten.pdf. viewed on 26th January 2016, 10:55.
- [187] Ruggaber. Durogan (DH). Data Sheet, . URL <http://www.ruggaber.de/kupfer/dblisodraht/IsodrahtDuroganDH.pdf>. viewed on 30th September 2015, 17:16.
- [188] Ruggaber. Multogan 2000 (MH). Data Sheet, . URL <http://www.ruggaber.de/kupfer/dblisodraht/IsodrahtMultoganMH.pdf>. viewed on 30th of September 2015, 17:17.
- [189] Schramberg. Strontium Ferrite HF 26/24. Data Sheet, . URL http://www.magnete.de/uploads/tx_fbmagneticfieldcalc/HF_26_24_D.pdf. viewed on 11th of November 2015, 18:23.
- [190] Schramberg. Strontium Ferrite HF 28/26. Data Sheet, . URL http://www.magnete.de/uploads/tx_fbmagneticfieldcalc/HF_28_26_D.pdf. viewed on 17th November 2015, 12:13.
- [191] Schramberg. Strontium Ferrite HF 30/26. Data Sheet, . URL http://www.magnete.de/uploads/tx_fbmagneticfieldcalc/HF_30_26_E.pdf. viewed on 30th of September 2015, 17:19.
- [192] Schramberg. Barium Ferrite HF 8/22. Data Sheet, . URL http://www.magnete.de/uploads/tx_fbmagneticfieldcalc/HF_8_22_E.pdf. viewed on 30th of September 2015, 17:19.
- [193] Schunk Carbon Technology. Fiber Reinforced Armor Sleeves for Permanent Magnet Motors. Catalogue, 2015. URL http://www.schunk-group.com/uploads/tx_rmsschunkttest/20.36e_Armor-Sleeves_2015_06.pdf. viewed on 30th of September 2015, 17:20.
- [194] Siemens AG. SINAMICS S120 Synchronmotoren 1FT7. Data Sheet, July 2011. URL https://cache.industry.siemens.com/dl/files/223/52334223/att_108933/v1/1FT7_de-DE.pdf. viewed on 27th October 2015,17:30.
- [195] Testec Elektronik GmbH. Active Differential Probes TT-SI 9101. Data Sheet, August 2006. URL http://www.distrelec.de/Web/Downloads/1_/ds/ttsi9101_mul_ds.pdf?mime=application%2Fpdf. viewed on 25 January 2016, 15:37.
- [196] Thyssen Krupp Steel. Power Core M330-35A. Data Sheet, May 2013. URL <https://www.thyssenkrupp-steel-europe.com>. viewed on 30th of September 2015, 17:22.
- [197] Thyssen Krupp Steel. Produktkatalog Nicht kornorientiertes elektroband Power Core. Catalogue, May 2013. URL <https://www.thyssenkrupp-steel-europe.com>. viewed on 30th of September 2015, 17:31.

- [198] Ticoma Engineering Polymers. Fortron 1140L4 PPS Glass Reinforced. Data Sheet, January 2007. URL <http://www.hipolymers.com.ar/pdfs/fortron/datos/fortron%201140L4.pdf>. viewed on 7th of October 2015.
- [199] Toho Tenax. HTS40F13. Data Sheet, April 2012. URL <http://www.tohotenaxamerica.com/products/pls020.pdf>. viewed on 30th of September 2015, 17:32.
- [200] Toshiba. Rare-Earth Cobalt Magnets TOSREX. Data Sheet. URL http://www.toshiba-tmat.co.jp/eng/product/pdf/e_cmp_10.pdf. viewed on 1st of December 2015, 17:49.
- [201] Umicore. BrazeTec Silfos 15. Data Sheets, May 2011. URL http://technicalmaterials.unicore.com/Brazetec/de/datenblaetter/show_BT_Silfos_15.pdf. viewed on 14th October 2015; 11:02.
- [202] Vacuumschmelze. Selten-Erd-Dauermagnete Vacodym- Vacomax. Data Sheet, 2014. URL http://www.vacuumschmelze.de/fileadmin/Medienbibliothek_2010/Downloads/DM/VACODYM-VACOMAX-dt_12112014.pdf. viewed on 30th of September 2015, 17:53.
- [203] Vetrotex. E,R and D glass properties. Data Sheet, March 2002. URL http://glassproperties.com/glasses/E_R_and_D_glass_properties.pdf. viewed on 30th September 2015; 17:33.
- [204] Victrex. VICTREX PEEK 450G120. Data Sheet, July 2014. URL http://www.victrex.com/~media/datasheets/victrex_tds_450g120.ashx. viewed on 30th September 2015; 17:36.
- [205] K. Wiens. A Visit to the Only American Mine for Rare Earth Metals, February 2012. URL <http://www.theatlantic.com/technology/archive/2012/02/a-visit-to-the-only-american-mine-for-rare-earth-metals/253372/>. viewed on 30th September 2015, 09:59.
- [206] C.-W. Yap. China Ends Rare-Earth Minerals Export Quotas, January 2015. URL <http://www.wsj.com/articles/china-ends-rare-earth-minerals-export-quotas-1420441285>. Viewed on 30th September 2015, 09:59.
- [207] Yokogawa Meters & Instruments Corporation. DL850E/DL850EV ScoperCorder User's Manual. Data Sheet, October 2015. URL <https://www.yokogawa.com/pdf/provide/E/GW/IM/0000028031/0/IMDL850E-02EN.pdf>. viewed on 25th January 2016, 15:28.
- [208] ZES ZIMMER. LMG 670 Precision Power Analyzer. Data Sheet, October 2014. URL <http://www.zes.com/de/content/download/487/4829/file/LMG670-4Seiter-DE-Web.pdf>. viewed on 27th October 2015, 17:43.
- [209] ZES ZIMMER. ZES Sensors and Accessories. Data Sheet, May 2014. URL www.zes.com/en/content/download/493/4885/file/ZES_SENSORS.pdf. viewed on 27th October 2015, 17:40.

A Appendix

A.1 Motor type Choice Decision Matrix

In this section the motor type decision matrices introduced in section 2.3 are shown. The following enumeration also lists the subcategories:

- Designated space
 - diameter
 - length
 - round configuration
 - rectangular configuration
 - separation of the components
- Weight
 - power electronics
 - motor
 - housing
- Efficiency
 - below 48V DC
 - above 48V DC
- Ability to modularize
 - modularized power increase
 - modularized speed increase
 - modularized voltage increase
 - modularized control algorithm

- Research intensity
 - development of new control algorithm
 - development of new stator geometry
 - development of new rotor geometry
 - development of new power electronics
 - development of new sensors
- Manufacturability
 - available manufacturability
 - external manufacturability
 - investment cost in manufacturing
 - ability for mass production
- Material cost above 48V DC and below 48V
 - magnet costs
 - copper costs
 - stator lamination costs
 - rotor lamination costs
 - semiconductor costs
 - capacitor costs
 - semiconductor driver costs
 - sensor costs
 - processor costs
 - joining technique costs
 - housing costs
 - extra costs, i.e. commutator
- Manufacturing costs
 - manufacturing magnet
 - manufacturing winding
 - manufacturing stator laminations
 - manufacturing rotor laminations
 - manufacturing power electronics
 - manufacturing processor PCB

manufacturing sensors

manufacturing joining technique

manufacturing housing

assembly

- Consequences material price development

affected by copper price increase

affected by lamination price increase

affected by isolation price increase

affected by magnet price increase

affected by shaft steel price increase

affected by sensor price increase

affected by semiconductor price increase

affected by processor price increase

affected by joining technique price increase

affected by capacitor price increase

- Material delivery reliability

affected by copper

affected by magnets

- Acoustics

disturbing noise

- Sensors

interpretation of sensor signals

excitation of sensors

reliability of sensor

- Robustness

robustness

maintainability

life expectancy

- Modular manufacturability
 - length variability at fixed diameter of stator
 - length variability at fixed diameter of rotor
 - fixation inside the assembly line
 - housing standardization
- Dynamics
 - dynamics
 - torque control
 - overload capabilities
 - characteristic curve

A.2 Inner vs. Outer Choice Decision Matrix

In this section the inner and outer motor matrices introduced in section 2.3.1 are shown. Here several subcategories are also investigated:

- Power, Torque
 - S1 torque density
 - S1 power density
 - S3 torque density
 - S3 power density
 - torque out of flux
 - torque out of current
 - efficiency
- Manufacturability of rotor
 - bandage
 - shaft
 - magnets
- Manufacturability of stator
 - flyer winding
 - needle winding
 - linear winding

- Cooling
 - rotor heat removal
 - stator heat removal
 - cooling effectiveness
 - rotor temperature
 - stator temperature
- Costs
 - magnets
 - copper
 - bearing
 - stator laminations
 - rotor laminations
 - wedges
 - inverter for S1
 - inverter for S3
- Mechanical
 - radial force absorption
 - vibration absorption
 - robustness

A.3 Winding Technology Decision Matrix

In this section, the winding technology decision matrix is presented. The winding procedures are:

- Needle winding of pole chain
- Needle winding of inside slotted stator
- Needle winding of outside slotted stator
- Flyer winding of single tooth
- Flyer winding of outside slotted stator
- Flyer winding of pole chain
- Linear winding of outside slotted stator

- Linear winding of single pole
- Linear winding of pole chain
- Hook or guide winding

The parameters are:

- Quality of the wire after winding
- Electric copper fill factor
- Heat removal of the winding
- Automation
- Stator pre- and post-processing
- Phase insulation
- Electric symmetry of the phases/windings
- Mechanical symmetry of the stator
- Turnout of the winding machine
- Investment for stator production
- Number of contacts
- Electric circuitry of the poles
- Flexibility of the circuitry
- Vibration stability
- Usability for diversity of types and set-up costs
- Number of stator parts
- Ability to wind thick copper wire
- Good wire return with orthocyclic winding

Motor Design for maximum Material Exploitation and Magnetization Procedure with in-line Quality Check for Mass Production

To reduce the amount of Rare-earth Elements in high efficient permanent magnet electric motors, the magnetic stray flux has to be reduced. Additionally, a temperature reduction inside the motor reduces the necessary amount of the so called Heavy Rare-earth Elements, which account for the bulk part of the magnet material costs. In this thesis a permanent magnet motor in wet rotor configuration for an automotive application is designed. It was shown that by simple thermal improvements of the electric insulation system the maximum temperature of the stator can be reduced. Extensive measurements on different combinations of insulation material of the stator and the development of a new thermal model for orthocyclic wound stators were performed. Due to the use of fiber cans eddy current losses could be eliminated and the stray flux minimized. In a second stage a magnetizing fixture was build up, which is able to magnetize the buried magnets inside the rotor. The rotor and the magnetizing fixture was developed, so that the magnets can be optimal magnetized.

ISBN 978-3-7983-2883-9 (print)

ISBN 978-3-7983-2884-6 (online)



ISBN 978-3-7983-2883-9



<http://verlag.tu-berlin.de>